공학박사학위논문

# Enhancement of Initial Coulombic Efficiency of Molybdenum Oxide Electrodes for Lithium-ion Batteries

## 리튬 이온 전지용 몰리브데넘 산화물 전극의 초기 쿨롱 효율 향상

2015년 8월


서울대학교 대학원

화학생물공학부

장 지 현

# ABSTRACT

## Enhancement of Initial Coulombic Efficiency of Molybdenum Oxide Electrodes for Lithium-ion Batteries

**Jihyun Jang**

Department of Chemical and Biological Engineering
The Graduated School
Seoul National University

Although graphite, the negative electrode for commercialized lithium-ion batteries, has lots of advantages, it shows limited specific capacity to apply it to the high-capacity lithium-ion batteries such as electric vehicles and energy storage systems. Among alternative materials to overcome such drawback, transition metal oxides which react with lithium through a conversion reaction having high specific capacity have been exploited. During the lithiation, as metal – oxygen bond in metal oxide is broken, metal

ion is reduced elemental state by taking electrons and oxygen ion forms chemical bonds with lithium ion to be generated $Li_2O$. In de-lithiation process, the reverse reaction occurs by the oxidation of metal component and formation of metal – oxygen bond again.

Molybdenum oxides react with lithium by an insertion or conversion reaction according to Mo valence, or bond strength between Mo and O. In the lithiation by conversion reaction, it delivers high specific capacity, especially very high in $MoO_3$, 6 $Li^+$/electrons per formula unit giving corresponding theoretical specific capacity of 1117 mAh $g^{-1}$. However, due to the constantly cleavage and formation of metal – oxygen bond and severe electrolyte decompositions at the surface of newly formed nano-sized metal, they show poor electrochemical performance including low initial Coulombic efficiency. Since the lithium sources in full-cell are limited, low ICE causes the decrease in cell capacity dramatically in the subsequent cycles. Thus, such drawback should be overcome for the use in practical LIBs.

In this study, to enhance the electrochemical performance, especially the initial Coulombic efficiency, of molybdenum oxides, three strategies are performed. Firstly, by the change of pH in the preparation of amorphous molybdenum oxides, the Mo valence of them are changed, which results in the improvement of electrochemical performance. In the second strategy, the reaction mechanism of $MoO_3$ electrode is examined, and its initial Coulombic efficiency and electrochemical performance is improved by just short-time ball-milling. The reason is likely due to the effect from the

grinded surface of particles and tens of nanometric particles generated by ball-milling. Lastly, a new type of negative electrode, $Li_2MoO_3$, is introduced, which is designed to release larger amount of lithium ions and electrons in de-lithiation than amount of them taken in lithiation. Through such reaction, $Li_2MoO_3$ electrode shows the initial Coulombic efficiency higher than 100 % and good cycle performance as well. In addition, for in-depth analysis about what happens in these electrodes proposed in three strategies, several kinds of electrochemical and spectroscopic methods are used. By using these solutions, it is expected that the improvement of electrochemical performance can be achieved not only in molybdenum oxides but also other conversion reaction-type metal oxides. Furthermore, this work can help the use of conversion reaction-type transition metal oxides into the negative electrode for practical LIBs in the near future.

---

**Keywords:** Lithium-ion batteries, Negative electrode, Molybdenum oxide, Amorphous oxide, Conversion reaction, Initial Coulombic efficiency

**Student Number:** 2010 – 21012

# CONTENTS

# LIST OF FIGURES

Mo valence.

**Figure 9.** The first- and second-cycle voltage – capacity profiles of (a) aM2-0.8, (b) aM2-4, and (c) cM3 electrodes over the voltage range of 0.01 ~ 3.0 V (*vs.* $Li/Li^+$).

**Figure 10.** The first- and second-cycle differential capacity (dQ/dV) plots of (a) aM2-0.8, (b) aM2-4, and (c) cM3 electrodes for lithiation, and (d) aM2-0.8, (e) aM2-4, and (f) cM3 electrodes for de-lithiation, respectively.

**Figure 11.** The second- and third-cycle differential capacity (dQ/dV) plots for cut-off controlled (a) aM2-0.8, (b) aM2-4, and (c) cM3 electrodes. The cut-off voltages are as follows: 0.01 V (*vs.* $Li/Li^+$) for the first-, second-, and third-cycle lithiation, and 3 V (*vs.* $Li/Li^+$) for the first-cycle de-lithiation, 0.8 V (*vs.* $Li/Li^+$) for the second- and third-cycle de-lithiation.

**Figure 12.** Cycle performance of aM2-0.8, aM2-4 and cM3 electrodes with current density of 100 mA $g^{-1}$ over voltage range of 0.01 ~ 3.0 V (*vs.* $Li/Li^+$). Only the de-lithiation capacity is shown.

**Figure 13.** (a) The first-cycle voltage – capacity profile and (b) dQ/dV plot of $MoO_3$ (99.5 +%; Sigma-Aldrich) electrode. Black spots and white squares are the points for *ex-situ* XRD, and *ex-situ* XANES, respectively.

**Figure 14.** *Ex-situ* XRD patterns of $MoO_3$ (Sigma-Aldrich) electrode before cycling (OCV), after lithiation until 2.5 V, 2 V, 400 mAh $g^{-1}$, and 0 V (*vs.* $Li/Li^+$). White square is peak from Cu current collector. Reference $MoO_3$ (JCPDS # 05-0508) is indicated as the gray drop line.

**Figure 15.** *Ex-situ* XANES of $MoO_3$ (Sigma-Aldrich) electrodes (a) before cycling (OCV), after lithiation until 1.5 V, 0 V (*vs.* $Li/Li^+$), and (b) before cycling (OCV), after de-lithiation up to 0.8 V, 3 V (*vs.* $Li/Li^+$). XANES spectrum for Mo metal is also indicated as the reference (gray line).

**Figure 35.** *Ex-situ* XANES spectra for 30 min ball-milled $MoO_3$ electrode after de-lithiation until 2.2 V and 3 V (*vs.* $Li/Li^+$). Spectra for bare electrode before cycling is also depicted as gray dash line (indicated as OCV).

**Figure 36.** Cycle performance of bare and ball-milled $MoO_3$ electrodes at the current density of (a) 100 mA $g^{-1}$ and (b) 500 mA $g^{-1}$.

**Figure 37.** The first- and second-cycle voltage – capacity profiles of 30 min ball-milled (a) $MoO_2$ (99 %; Sigma-Aldrich) and (b) $MoO_3$ (99.5 +%; Sigma-Aldrich) electrodes.

**Figure 38.** (a) The first- and second- cycle voltage – capacity profiles and (b) the current behavior of $Li_2MoO_3$ electrode in the first-cycle lithiation. Dotted line in (b) indicates the expected current profile for Cottrell behavior.

**Figure 39.** *Ex-situ* XRD patterns of $Li_2MoO_3$ electrode before cycling (pristine), after lithiation until 0 V (*vs.* $Li/Li^+$), and de-lithiation up to 3 V (*vs.* $Li/Li^+$). White square and triangles are peaks from copper current collector and beryllium window, respectively.

**Figure 40.** The first-cycle de-lithiation dQ/dV plots of $MoO_2$, $MoO_3$ and $Li_2MoO_3$ electrodes. Arrows are indicated the peak at around 2.5 V (*vs.* $Li/Li^+$).

**Figure 41.** *Ex-situ* (a) XANES and (b) EXAFS spectra of $MoO_2$, $MoO_3$, and $Li_2MoO_3$ electrodes before cycling.

**Figure 42.** *Ex-situ* (a) XANES and (b) EXAFS spectra of $MoO_2$, $MoO_3$, and $Li_2MoO_3$ electrodes after the first-cycle lithiation. Reference Mo metal is also indicated and peak intensity of it in (b) decreases by half.

**Figure 43.** *Ex-situ* (a) XANES and (b) EXAFS spectra of $MoO_2$, $MoO_3$, and $Li_2MoO_3$ electrodes after the first-cycle de-lithiation. EXAFS spectra of $MoO_3$ before

cycling is also depicted in (b) for the comparison.

**Figure 44.** (a) *Ex-situ* XANES spectra of $MoO_2$, $MoO_3$ and $Li_2MoO_3$ electrode after the first cycle. Spectra of Mo metal and $MoO_2$, $MoO_3$ electrodes before cycling are also depicted for the reference. (b) The relationship between Mo K-edge shift energy derived from (a) and Mo valence.

**Figure 45.** *Ex-situ* (a) XANES and (b) EXAFS spectra of the de-lithiated $Li_2MoO_3$ electrode until 2.2 V and 3 V (*vs.* $Li/Li^+$). For the comparison, spectra are also represented: $MoO_2$ and $MoO_3$ electrodes before cycling in (a), and after the first cycle in (b).

**Figure 46.** Schematic illustration of reaction mechanism of $MoO_2$, $MoO_3$ and $Li_2MoO_3$ electrodes during the first-cycle lithiation and de-lithiation processes.

**Figure 47.** (a) The first- and second-cycle voltage – capacity profiles and (b) the first-cycle de-lithiation dQ/dV plots of a composite electrode consisting a physical mixture of $MoO_2$ and $Li_2O$ electrode. The first-cycle de-lithiation dQ/dV plots of $MoO_2$ and $Li_2MoO_3$ electrodes are also indicated in (b) for the comparison.

**Figure 48.** The first- and second- voltage – capacity profiles of (a) $RuO_2$ (99.9 %; Sigma-Aldrich) and (b) $Li_2RuO_3$ electrodes.

**Figure 49.** (a) Cycle performance with current density of 100 mA $g^{-1}$ and (b) rate performance of $Li_2MoO_3$ electrodes over voltage range of 0 ~ 3 V (*vs.* $Li/Li^+$). Only the de-lithiation capacity is shown, and current density (in mA $g^{-1}$) is indicated below the data points in (b).

**Figure 50.** The first- and second- voltage – capacity profiles of (a) SiO (Sigma-Aldrich) and (b) a composite electrodes consisting of hand-mixed SiO and $Li_2MoO_3$.

**Figure 51.** The first-cycle de-lithiation dQ/dV plots of SiO, $Li_2MoO_3$, and a composite

# LIST OF TABLES

# 1. INTRODUCTION

Energy is one of the most important issue in human life, because it is useful. It is found in a numerous different forms including thermal energy as heat, chemical energy in fuel, the kinetic energy in moving water and wind, and magnetic and electrical energy. Usually, we want to use one form in another form, and this requires energy conversion and transducer devices. In addition, energy may be presented in different with those when and where we want to use it. Therefore, energy storage device which can store and transport from place to place has been important. Such conversion device is also called *batteries*, and energy stored in batteries are often called *the electrochemical energy*, which means to convert between two different types of energy: electrical and chemical energy.

Electrical energy also can be stored in electric or magnetic field, by mechanical energy as flywheels, and thermal energy in form of heat. However, the amount of energy stored in these form is relatively small and the methods for the conversion into other form are difficult. On the other hands, by using batteries, much large amount of

energy can be stored as the chemical species. It is efficient in terms of energy stored per unit weight or volume, and relatively inexpensive than other storage methods. Thus, storage as the chemical energy is a useful, keeping energy for later use to other forms such as electric, heat, light, or mechanical energy.

Recently, the development of better batteries is a great deal of interest. Behind of such concerns, there are several important issues related to the environment in which we live. It has been revealed that the emission of greenhouse gases generated by combustion of fossil fuel is main cause of global warming. In addition, various side products generated during combustion leads to environmental pollution and smog in the urban cities. Such problems are getting worse due to dramatically increased vehicles which are using a combustion engine. Therefore, the demand of other power generator such as batteries rather than engine in vehicle has been growing. To use batteries as main energy sources in electric vehicles, huge amount of energy must be available to store and release. Therefore, many researches have been conducted to enlarge energy of batteries. Specific energy (Wh $kg^{-1}$) or volumetric energy (Wh $L^{-1}$) of battery is determined by the cell voltage and specific capacity (mAh $g^{-1}$) or volumetric capacity (mAh $L^{-1}$), respectively.[1] Among various kinds of batteries, lithium-ion batteries (LIBs) have been spotlighted because it can store and convert the much higher energy than other kinds of batteries by enlarged specific capacity and high reaction voltage with high stability.

LIB consists of four main component: negative electrode, positive electrode, electrolyte, and separator. In practical LIBs, graphite and lithium cobalt (III) oxide ($LiCoO_2$) are used as negative and positive electrode, respectively. Although it shows good performance in small electronic devices such as mobile phone and notebook PC, there are limitation in the usage of high-capacity system such as electric vehicles (EVs) mentioned above, and energy storage system (ESS).[2-3] In particular, since graphite negative electrode shows limited capacity per unit weight and volume, many alternatives which show enlarged capacity have been considered, for examples alloying materials and transition metal oxides.[4-8] When the latter reacts with lithium through a conversion reaction, it can exhibit about 3 ~ 4 times higher capacity than carbonaceous materials. Molybdenum oxides also are known to show high specific capacity when lithiated by a conversion reaction. However, due to the large hysteresis and poor Coulombic efficiency, it has been struggling for practical use. Among shortcomings of conversion reaction-type transition metal oxides, low initial Coulombic efficiency (ICE) is the most critical because it affects directly into the capacity of full-cell in the subsequent cycles.

In this work, the electrochemical performance of molybdenum oxide negative electrode can be enhanced by three strategies. First one is the control of synthetic parameters of amorphous molybdenum oxide. Amorphous molybdenum oxides are known to be a good negative electrode materials showing high specific capacity with good cycle performance when it reacts by an insertion reaction rather than conversion

reaction.[9] Along this line, Mo valence of amorphous molybdenum oxide (δ in $MoO_{2+\delta}$) can be altered by the control of pH during the solution-based preparation. In addition, a small variation of Mo valence can determine the reaction mechanism, insertion or conversion reaction, and eventually the electrochemical performance. By preparation in low pH (pH=0.8), Mo valence in amorphous molybdenum oxide deceases up to +4, and therefore, it can react with lithium through the insertion reaction, which results in enhanced electrochemical performance than that reacted by the conversion reaction.

Second study is about enhancement of ICE and other performance of molybdenum trioxide ($MoO_3$) by just short-time ball-milling. Although $MoO_3$ electrode exhibit high specific capacity by conversion reaction ($MoO_3 + 6Li^+ + 6e^- \rightarrow Mo^0 + 3Li_2O$, theoretical specific capacity: 1117 mAh $g^{-1}$), it also shows extremely poor Coulombic efficiency in the first cycle due to difficulty of oxidation of molybdenum up to +6 in de-lithiation. By just short-time ball-milling, ICE of $MoO_3$ electrode is much enhanced by the formation of the grinded surfaces and tens of nanometric particles. The effects of them are demonstrated by electrochemical and spectroscopic methods. Since they cannot be prepared by solid-state synthesis even in low heating temperature, weak ball-milling can be one of the simple solutions to improve the performance of conversion reaction-type metal oxides.

The last one is the development of a new negative electrode material for LIBs which shows ICE higher than 100 % by introducing a molecular mixture of $Li_2O$ and molybdenum dioxide ($MoO_2$), in other words, $Li_2MoO_3$. In this electrode, $Li_2O$

component is idling during lithiation, and participate in bond forming reaction (de-conversion reaction) during de-lithiation, which results in higher capacity in de-lithiation than that in lithiation. Such behavior exhibiting unusually high ICE is demonstrated by electrochemical, and especially spectroscopic method by using XAS (X-ray absorption spectroscopy) to trace the change of Mo valence according to cycling. Since it shows good cycle performance with high capacity (900 mAh $g^{-1}$ at $50^{th}$ cycle), $Li_2MoO_3$ electrode can be good candidate of negative electrode for LIBs. In addition, owing to ICE higher than 100 %, it can be also useful when mixed with other negative electrode material whose showing enormous specific capacity but poor ICE such as Si, SiO.

# 2. BACKGROUND

## 2.1. Chemistry and electrochemistry for lithium-ion batteries

The "Battery" is a device that can store the electric energy as the chemical energy during charge, and convert the chemical energy into the electric energy during discharge. The amount of energy stored and released is related with the energy level difference between two electrode materials. Generally, the energy possessed in the material can be represented by the *chemical potential* ($\mu_i^\alpha$), for species *i* in phase α:

$$\mu_i^\alpha = (\frac{\partial G}{\partial n_i})_{T,P,n_j}$$

where $n_i$ is the number of moles of *i* in phase α. That is, the chemical potential means the change of molar Gibbs free energy for the addition of species *i* into phase α when a temperature and pressure are fixed (Fig. 1a). The reaction proceeds in the direction the chemical potential is reduced, and thus, we also called it as the escaping tendency. In addition, when the charged species *i* is inserted into phase α which has the potential ($\phi^\alpha$), there is the change of the electric work (or energy, $z_i F\phi^\alpha$) as well as the change of the chemical potential ($\mu_i^\alpha$) (Fig. 1b). The *electrochemical potential* ($\overline{\mu_i^\alpha}$) is introduced for species $\underline{i}$ with charge $z_i$ in phase α.

$$\bar{\mu}_i^{\alpha} = \mu_i^{\alpha} + z_i F \phi^{\alpha}$$

Therefore, the electrochemical potential rather than chemical potential could be used to represent energy level in electrode materials. During the discharging process of battery, the electrochemical energy difference between two electrode materials is released as the electric energy, and this energy difference is filled again during charging process.

The energy conversion process between the electric and chemical energy can be realized by the electrochemical reaction involving electrons: *redox (oxidation and reduction) reaction*. Oxidation and reduction reaction generally accompany the loss and the gain of electrons, respectively.

$$\nu_A A \rightarrow \nu_C C + ne^- \text{ (oxidation)} \quad (1a)$$

$$\nu_B B + ne^- \rightarrow \nu_D D \text{ (reduction)} \quad (1b)$$

Most of cells consist of two electrodes (anode and cathode), and electrolyte. The oxidation and reduction reaction take place at the anode and cathode, respectively. In the rechargeable batteries, however, oxidation and reduction reaction occur on the one electrode during charge and discharge. Therefore, negative and positive electrodes rather than anode and cathode are less confused for the realistic situation at the electrode in the electrochemical cell. By using these two electrodes and two redox reactions (1a and 1b), called *half-cells*, the electrochemical cell can be made with following the overall reaction:

$$\nu_A A + \nu_B B \rightarrow \nu_C C + \nu_D D \quad (2)$$

In this electrochemical cell, oxidation and reduction reaction take place simultaneously at two electrodes, within electrolyte as ion transfer medium. The difference in redox tendency between A and B molecules at two electrodes, that is the energy to store and release, is represented by the *standard Gibbs free energy change of reaction* ($\Delta G_{rxn}^0$):

$$\Delta G^0_{rxn} = -nFE^0 \quad (3)$$

where F is Faraday constant ($9.6485 \times 10^4\ equiv^{-1}$), and $E^0$ is a *standard*

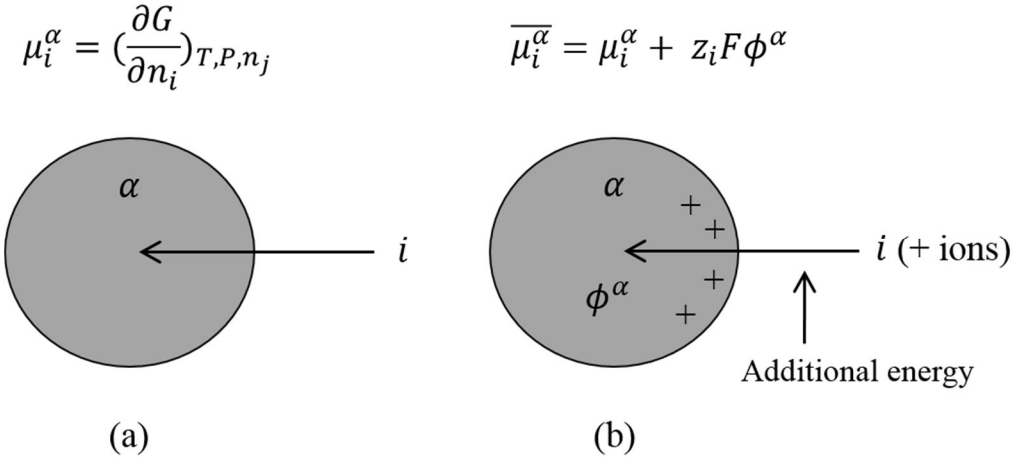


[10]



**Figure 1.** The definition for chemical potential and electrochemical potential.

*electromotive force* (EMF, V) for the electrochemical cell. The symbol $^0$ indicates that this system is the standard state ($10^5$ Pa, 298.15 K). If A molecule has larger oxidation tendency than B molecule (or large reduction tendency of B molecule than A molecule), reaction (2), or reaction (1a) and (1b) can take place spontaneously, and therefore this electrochemical cell can release the electric energy corresponding to the difference in redox tendency between A and B molecules, that is $\left|\Delta G_{rxn}^0\right|$. As in this case, when the reaction take place spontaneously, the standard Gibbs free energy of reaction is negative ($\Delta G_{rxn}^0 < 0$), and this cell is called as galvanic cell. On the other hands, if the standard Gibbs free energy of reaction is positive ($\Delta G_{rxn}^0 > 0$, reverse of reaction (2) in this case), this reaction cannot happen spontaneously and external energy should be supplied into the cell, called electrolytic cell.

The standard EMF ($E^0$) in the electrochemical cell also indicates the difference in the degree of redox tendency between two half-cells as in:

$$E^0 = E_{RHS}^0 - E_{LHS}^0$$

where $E_{RHS}^0$ is the standard reduction potential in the right-hand side (RHS) half-cell, and $E_{LHS}^0$ is the standard reduction potential in the left-hand side (LHS) half-cell. Note that the RHS and LHS choose as $E_{RHS}^0 > E_{LHS}^0$, and thus $E^0 > 0$ ($\Delta G_{rxn}^0 < 0$) for spontaneous reaction. If $E^0 < 0$, this cell does not work spontaneously, it should be supplied energy from external circuit. In reaction (2), RHS reaction is $\nu_B B + ne^- \rightarrow \nu_D D$, and LHS reaction is $\nu_C C + ne^- \rightarrow \nu_A A$. In non-standard condition, however, the equilibrium cell potential ($E_{eq}$) of reaction (2) should be modified by the *Nernst equation*:

$$E_{eq} = E^0 + \frac{RT}{nF} ln \frac{a_A^{\nu_A} a_B^{\nu_B}}{a_C^{\nu_C} a_D^{\nu_D}}$$

where $a_i$ is an activity of species i, R is a gas constant (8.314 $JK^{-1}mol^{-1}$), and T is an absolute temperature (K).

Energy is the product of cell voltage and capacity. Thus, in order to increase the energy in the battery, high cell voltage (large potential difference between positive and negative electrode) and high capacity are needed. Metallic lithium had been considered as a negative electrode material since its standard reduction potential is the lowest among all elements, -3.045 V (*vs.* NHE). In addition, it is the lightest elements except proton and helium, which results in the highest capacity (theoretical specific capacity: 3862 mAh $g^{-1}$). In the 1972, the rechargeable lithium batteries were firstly proposed by M. S. Whittingham:[11-12] the concept of electrochemical lithium ion intercalation was defined, titanium sulfide ($TiS_2$) as positive electrode and metallic lithium as negative electrode in a liquid organic electrolyte. In the 1980s, commercialization of this kind of rechargeable lithium batteries, such as the Li/$MoS_2$, failed because of the several drawbacks of lithium metal: explosion risk and poor cycle performance due to the dendritic growth and/or dead lithium.[13]

Because of these problems, less-dangerous rechargeable lithium batteries with no metallic lithium have been considered. Many researchers including Armand revealed that alkali ion can intercalate between the layers of graphite.[14] Graphite shows reversible lithium ion intercalation and de-intercalation behavior at a low voltage, around 0.2 V (*vs.* $Li/Li^+$) which value is similar with metallic lithium. However, since there is no lithium sources in the graphite, positive electrode should possess lithium sources. Meanwhile, in 1979, J. B. Goodenough and coworkers developed the lithium cobalt oxide, $Li_xCoO_2$.[15-16] Metal oxide family including lithium ion, $Li_xMO_2$ (M = Co, Ni, Mn), could be used as a positive electrode materials for lithium-ion batteries. By using these materials with proper electrolyte, Sony in Japan had commercialized the *lithium-ion batteries (LIBs)* (3.6 V, 120 – 150 Wh $kg^{-1}$) in 1991.[13] After the 1990s, the LIBs have been researched and improved considerably, but still, there are some shortcomings to be solved (Table 1).

**Table 1.** Specific characteristics of lithium-ion batteries.

| ***Advantages*** | ***Shortcomings*** (Ref.[13]) |
|---|---|
| *Performance data* | |
| · High cell voltage (3.0 – 4.2 V), specific energy (90 – 240 Wh $kg^{-1}$, 200 – 500Wh $L^{-1}$ at cell level), and specific power (up to 500 W $kg^{-1}$) | · Chemical reactivity; stability of the chemicals |
| · High discharge rate (40 *C*); fast charge (< 3h); useful power > 80 % DoD | · Higher internal impedance than nickel-cadmium |
| · More than 1000 cycles; deep cycling possible; Coulombic efficiency almost 100 % | · Degradation at high temperatures and at discharge < 2 V; capacity loss or thermal runaway when overcharged |
| · Low self-discharge rate (5-10 % per month, 20 $^{o}$C ) | · Temperature range : -20 $^{o}$C to +60 $^{o}$C |
| · No memory effect; no reconditioning needed; tolerates microcycles | · Venting and thermal runaway when crushed |
| *Cell design* | |
| · Low weight; very small batteries and high capacity available | · Safety precaution and protective circuitry |
| · Can be optimized for capacity or rate | · Stricter regulation on shipping |
| · No free liquid electrolyte; gelled electrolyte and solid-state chemistry available | · Preferred charge method; constant voltage, constant current |
| *Application and cost* | |
| · From consumer electronics to electric vehicles | · More expensive than lead-acid |

## 2.2. Components in lithium-ion batteries

As shown in Fig. 2, the lithium-ion batteries consist of four main components: *negative electrode, positive electrode, electrolyte* and *separator* (not shown in Fig. 2). Electrode materials in the commercialized and widely used lithium-ion batteries are layered materials: graphite as negative electrode material and layered lithium metal oxide as positive electrode material. After fabrication, the state of battery is discharged state (cell voltage ~ 0 V), so that it should be charged first. In the charging process, the voltage of positive electrode increases up to ~ 4.3 V (*vs.* $Li/Li^+$) by oxidizing transition metal ions in the oxide with the extraction of lithium ions. These lithium ions move into the negative electrode side through the electrolyte medium, and insert into the graphite layer while the voltage of negative electrode decrease around ~ 0.2 V (*vs.* $Li/Li^+$). In subsequent discharging, the reverse reaction proceeds and the state of battery returns its initial state. Generally, electrodes in LIB are porous composite, consisting of an active material, a conductive material (carbon black), and a polymer binder with various ratio according to an active materials and/or the purpose of cells.

### 2.2.1. Positive electrode materials

For rechargeable lithium batteries with a metallic lithium as the negative electrode, the positive electrode does not have lithium sources. In contrast, for the lithium-ion batteries, due to the ‘empty’ carbon negative electrode, the air-stable lithium-based intercalation materials must act as a sources of lithium ions during the first charging process. Most of positive electrode materials have tunnel structure to be stored and/or diffused lithium ions: olivine (1D channel), layered (2D channel), and spinel (3D channel) structures.

[17]

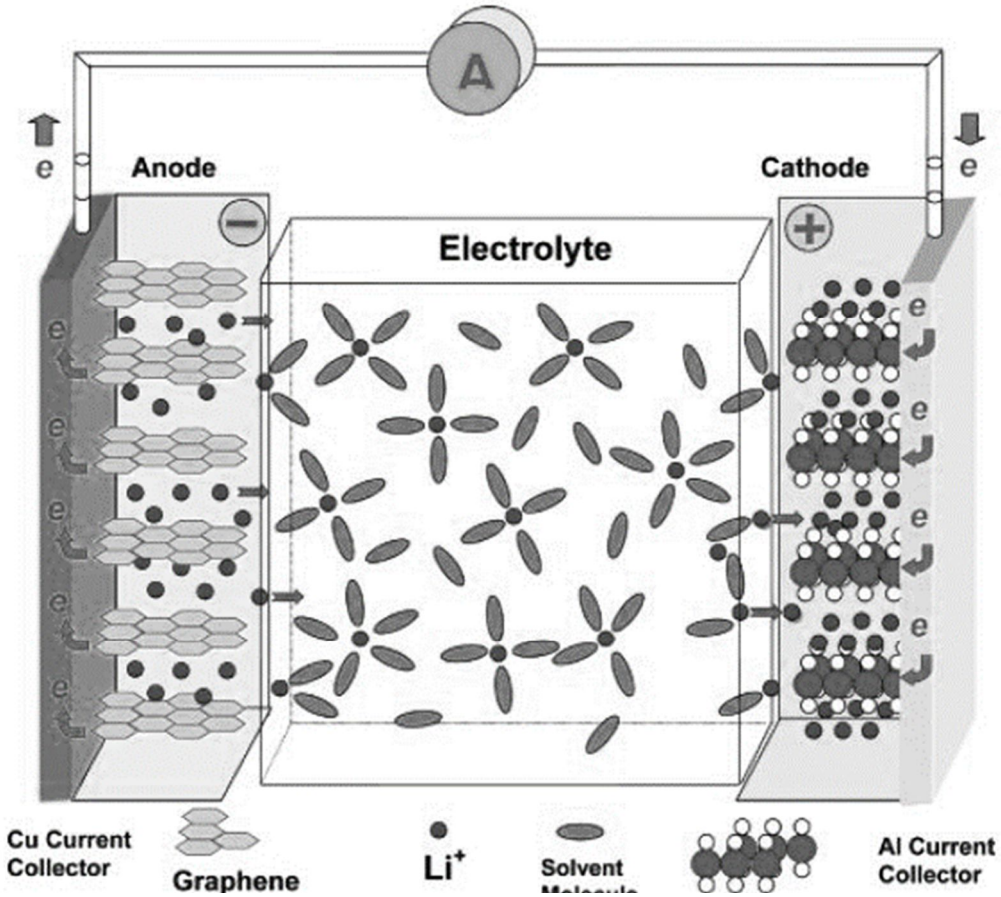


**Figure 2.** A schematic structure of the rechargeable lithium-ion batteries**.**

structure

#### 2.2.1.1. Layered structure oxides

The composition of lithium transition metal oxides which have *layered structure* are generally $Li_xMO_2$ (M = Co, Mn, Ni, etc.) with α-$NaFeO_2$ structure. Since lithium ions are located between $MO_2$ slabs, they can easily inserted into or removed from host structure. According to transition metal ions in slab, the properties of positive electrode material are changed.

As mentioned earlier, the positive electrode material in the first commercialized cells in SONY was *$LiCoO_2$ (LCO)*, whose properties were first investigated by J. B. Goodenough.[15] Its crystal structure can be described in terms of a close-packed face-centered cubic arrangement of oxygen ions, with the $Li^+$ and $Co^{3+}$ cations occupying octahedral coordinate positions in between layers of oxygen ions with alternate way. As a result, these materials are described as having layered, rather than simple cubic, structures.[18] It typically works at 3.5 – 4.3 V (*vs.* $Li/Li^+$), and provides a moderate specific capacity, 140 mAh $g^{-1}$ (when about 0.5 $Li^+$ per formula unit are used), with long cycle life, > 500 cycles with 80 – 90 % capacity retention. This material undergoes several phase changes during charge and discharge. If charging over 4.3 V (*vs.* $Li/Li^+$), it undergo severe structural destruction as well as the evolution of oxygen gas, which cause in capacity loss and safety issue in subsequent cycle.[19-21] Therefore, limited capacity ($Li_xCoO_2$, $1 > x > 0.5$) in < 4.3 V (*vs.* $Li/Li^+$) range should be used.

Because of higher cost and somewhat poisonous of LCO, it would be prefer to use *$LiNiO_2$ (LNO)*. LNO displays a ~ 0.25 V more negative reaction voltage and up to 30 % higher theoretical specific capacity than LCO.[22-23] However, it is difficult to synthesize the right stoichiometry due to the tendency for nickel ions to reside on the lithium ion layers (cation mixing), which results in a loss of capacity. In addition, LNO readily loses oxygen at high voltage, destroying its layered structure, and tending to lead to safety issues because of an exothermic reaction with the organic electrolyte. There have been numerous researches for the modification by the substitution of other

cations, such as $Co^{3+}$, $Mg^{2+}$, $Al^{3+}$ or $Ti^{4+}$ ions.[24] Especially, $LiNi_{1-x-y}Co_xAl_yO_2$ *(NCA)* with typical values of x = 0.15 and y = 0.05 is stable enough for commercial application.[25]

A number of other layered structure materials have also been investigated. Some of them contain two or more transition metal cations at fixed ratios, including Ni, Mn, Co, and Al. One of these is $LiNi_{1/3}Co_{1/3}Mn_{1/3}O_2$ *(NCM)*.[26-27] In this material, the nickel, cobalt, and manganese are divalent, trivalent, and tetravalent (discharged state), respectively. Thus, the major electrochemically active species is nickel, with the cobalt playing an active role only at high voltage. Owing to the stable binding of manganese and oxygen, the whole structure is stable, even when charged up to a higher voltage of 4.4 V (*vs.* $Li/Li^+$).

#### 2.2.1.2. Spinel structure materials

The spinel class of materials, with the nominal formula $AB_2O_4$, also has a close-packed face-centered cubic arrangement of oxygen ions. A wide range of materials with different A and B ions can have this structure, and some of them are quite interesting for use in the LIBs, for example, $LiMn_2O_4$ *(LMO)*. This material provide a voltage of around 4.0 V (*vs.* $Li/Li^+$), a specific capacity of about 140 mAh $g^{-1}$. The energy density is 10 % less than LCO, but it has somewhat better kinetics and does not evolve oxygen. LMO, first investigated by Thackeray *et al.*, has the inherent advantages of low cost, good kinetics due to the 3D diffusion channel for lithium ion, and being nonpoisonous.[28-29] However, the cell with manganese spinel positive electrodes suffers from poor cycling and storage stability at elevated temperatures owing to structural change (Jahn-Teller distortion) and the dissolution of $Mn^{2+}$ by HF attack in the electrolyte causing poisoning of the negative electrode.[30-31] To solve these problems, doping with elements having low valence such as lithium ($Li_{1+x}Mn_2O_4$), magnesium, zinc improves the cycling behavior of the spinel structure by suppressing the Jahn-

Teller distortion effect and increasing Mn valence.[32-33] In addition, the coating with $Al_2O_3$, $AlPO_4$ also acts as the positive effect on the cycle performance by the protection from HF attack and hence reduction of the dissolution of $Mn^{2+}$.[34-35]

*$LiNi_{0.5}Mn_{1.5}O_4$ (LNMO)* is also considered as a new candidate for the positive electrode, especially 5V-class electrode, in the LIBs. It also has spinel structure with delivering 120 mA h $g^{-1}$, in which the Mn valence remains 4+ and Ni ions are active with two-electron redox reaction ($Ni^{2+ / 4+}$). It shows high reaction voltage, but still remain problems related with the electrolyte whose electrochemical stability is limited up to 4 V (*vs.* $Li/Li^+$).[36-37]

#### 2.2.1.2. Olivine structure materials

The olivine structure materials are another material to be concerned with the positive electrode for LIBs. It has a hexagonal stacking of oxygen ions, described as $M_2XO_4$, in which M ions are in half of the available sites of the close-packed hexagonal oxygen array showing 1D channel for M ions. The more highly charged X ions occupy one-eighth of the tetrahedral sites. The most interesting material in olivine structures is *$LiFePO_4$ (LFP)*, firstly developed by Padhi *et al.*, that has the obvious advantage of safe and inexpensive.[38] It delivers 3.3 – 3.6 V (*vs.* $Li/Li^+$) and more than 90 % of its theoretical specific capacity of 165 mA h $g^{-1}$. In fact, $Fe^{2+ / 3+}$ redox reaction occur at around 3.2 V (*vs.* $Li/Li^+$), the induced effect of strong P – O covalent bonding in phosphate ion increases the reaction voltage up to 3.4 V (*vs.* $Li/Li^+$).[39-40] In addition, these materials do not tend to lose oxygen and react with the organic solvent electrolyte nearly so much as in the layered structure materials, and therefore, they are evidently much safer at elevated temperature. As a result, they are being considered for large-scale application, such as in vehicles or load leveling.

Due to the low electrical conductivity of LFP (< $10^{-9}$ S $cm^{-1}$), nano-size particles

and intimate contact with conductive carbon, must be used to avoid inactive areas in the bulk electrode and to reduce the distance for lithium ion transport in the solid.[41-42] A different approach is the material doping with highly charged (super-valent) metal ions, such as niobium, that could replace some of the lithium ions, increasing the n-type electronic conductivity.[43]

**Table 2.** Overview of rechargeable lithium-ion battery positive electrode materials.

| (Ref.[13]) | | $LiCoO_2$ | $LiNiO_2$ | $LiMn_2O_4$ | $LiFePO_4$ |
|---|---|---|---|---|---|
| Voltage (*vs.* $Li/Li^+$) | V | ~ 4.0 | ~ 3.8 | ~ 4.0 | ~ 3.5 |
| Cycle life | | > 1000 | Limited | Limited | > 1000 |
| Theoretical specific capacity | Ah $kg^{-1}$ | 137 | 192 | 148 | 170 |
| Theoretical capacity density | Ah $L^{-1}$ | 706 | 919 | 634 | - |
| Specific energy | Wh $kg^{-1}$ | 90 – 140 | - | 160 | - |
| Energy density | Wh $L^{-1}$ | 220 – 350 | - | 270 | - |
| Specific power | W $kg^{-1}$ | 760 | - | 1800 | - |

### 2.2.2. Negative electrode materials

In the early works on the rechargeable lithium batteries, the metallic lithium was used as the negative electrode. Although it shows the highest specific capacity and lowest reaction voltage, it has significant problems such as poor cycling and safety issues. The battery makers, therefore, currently have used a "host material" which has no metallic lithium and ability to be inserted and extracted lithium ion at a low voltage (near the reaction voltage of metallic lithium): carbonaceous materials, alloy materials, and transition metal-based inorganic compounds.

#### 2.2.2.1. Metallic lithium

It is obvious that *metallic lithium* has the lowest voltage, -3.045 V (*vs.* NHE), as well as the highest specific capacity, 3862 mA h $g^{-1}$, among any possible lithium reservoir materials in an electrochemical cell. There are many problems with the use of metallic lithium, however. (i) Deposition at unwanted locations: In the absence of a significant nucleation barrier, deposition will tend to occur anywhere including current collector and other parts of an electrochemical cell that are at the same electrical potential as the negative electrode. (ii) Shape change: The location of the electrodeposit is not the same as that where the discharge (dissolution) process took place, which results in a problem of current distribution and hydrodynamics. (iii) Dendritic growth: It is related to the inherent instability of a flat interface during electrodeposition, even in the case of a chemically clean surface. It also differs current distribution and cause short-circuit, dead-lithium and therefore thermal runaway. (iv) Low Coulombic efficiency and poor cycle performance due to newly formed the surface of metallic lithium in every cycle. Due to these drawbacks of metallic lithium, many substitutes have been researched to replace metallic lithium in negative electrode.[44-47]

In these days, however, to enlarge energy of the cell, metallic lithium is

considered again as a negative electrode in new battery systems such as *lithium – sulfur* and *lithium – air batteries* with new techniques including the additives, protective layer, solid electrolyte, and so on.[48-52]

#### 2.2.2.2. Carbonaceous materials

*Carbonaceous materials* are currently used as the negative electrode material in the very common small LIBs because of better dimensional stability, higher specific charges for lithium intercalation, and more negative redox voltage, around 0.2 V (*vs.* $Li/Li^+$) than most alternative materials. A wide range of structures and properties is possible to use, depending on how the carbon is produced. It is often divided into two categories: graphitic carbons and non-graphitic carbons.

The *graphitic carbon*, or *graphite*, consists of parallel sheets containing interconnected hexagon of carbon, called graphene layers or sheets. They are stacked with alternative layer, ABABA stacking. Graphite is amphoteric, which means either cations or anions can be inserted into it between the graphene layers. The insertion of alkali metal ions into graphite was first demonstrated in 1926, and chemical synthesis of lithium ion inserted graphite was demonstrated in 1955.[53] Insertion of alkali metal ion, especially lithium ion, occurs with staging phenomena which is a nonrandom filling of positions between the layers of the host crystal structure.[54] In the LIBs, during charge, lithium ions are inserted into graphite up to a theoretical composition of $LiC_6$ having a capacity of 372 mAh $g^{-1}$., following the reaction.

$$xLi^+ + xe^- + C_n \leftrightarrow Li_xC_n$$

Graphite generally has two planes: basal plane (perpendicular to c-axis) and edge plane (parallel to c-axis). The edge plane is the active plane for lithium ion insertion and the electrolyte decomposition, whereas inactive at the basal plane.

The *non-graphitic carbons* show a sloping voltage – capacity profile, with no evidence of staging. They are often divided into two types: designated as soft, or graphitizing, carbon and hard carbon.[55] *Soft carbons* are generally produced by the pyrolysis of liquid materials such as petroleum pitch, which is the residue from the distillation of petroleum fraction. The carbon atoms in their structure are initially arranged in small graphene-type groups, but there is a significant amount of imperfection, as well as randomness in the way that the layers are vertically stacked upon each other. It can be graphitized by a calcination in about 2500 $^{o}$C. On the other hands, *hard carbons* cannot be graphitized up to 2800 $^{o}$C due to a high degree of disorder. They are typically produced by the pyrolysis of solid materials, such as chars or glassy carbon, initially having a significant amount of initial cross-linking, as well as nanoporosity. The electrochemical behavior of these carbon materials is quite different with the graphite. There is a wide range of possible sites in which the lithium ion can reside, with different local structure, and energies.[56-57] The result in the voltage varies gradually, rather than showing the steps characteristics. It also can be seen that there are some capacity loss that is trapped in the structure and/or reacted with the functional group on the surface of carbons on the first cycle.

#### 2.2.2.3. Lithium alloys

The replacement of metallic lithium by *lithium alloys* has been investigated since Dey demonstrated the feasibility of electrochemical formation of lithium alloys in liquid organic electrolyte in 1971.[58] The reaction proceeds reversibly according to this equation.

$$xLi^{+} + xe^{-} + M \leftrightarrow Li_{x}M$$

There are many metal compounds that can alloy with lithium, for example, Al, Si, Sn, Pb, In, Bi, Sb, Ag, and some alloys.[59] In particularly, *Sn-based* and *Si-based alloy*

*compounds* have been considerably researched due to its higher specific capacity (994 mAh $g^{-1}$ for $Li_{22}Sn_5$, 3579 mAh $g^{-1}$ for $Li_{15}Si_4$ at room temperature and 4200 mAh $g^{-1}$ for $Li_{22}Si_5$ at high temperature[60]) than graphite (372 mAh $g^{-1}$ for $LiC_6$).

However, in a composite $(Li^+M^-)_xM^0$, since the $M^-$ are considerably larger than neutral $M^0$ atoms and the volume of $Li^+$ also cannot be ignored, the electrochemical cycling of lithium-alloy electrode is inevitably associated with large volume changes (100 ~ 300 %).[1] In addition, lithium alloys have highly ionic character, which results in that they are fairly brittle. Thus, these changes lead rapidly to deterioration of the electrode including cracks and eventually pulverization, resulting a low initial Coulombic efficiency and poor cycle life to only a few cycles. Significant researches have been conducted to alleviated or suppress the volume change during charge and discharge: (i) Size reduction of the matrix metals with nanostructured alloys, [61-63] and allowing more porous or breathing room by using nanostructures such as thin film and nanowires,[64-65] (ii) A composite of active / inactive metals or intermetallic alloys,[66-68] (iii) Using the high-end binder and/or electrolyte additives.[69-72] In 1997, Fuji introduced a new lithium-ion technology (STALION) using an amorphous tin composite oxide (ATCO) negative electrode, which reacts reversibly with lithium at about 0.5 V (*vs.* $Li/Li^+$) and has twice the capacity of graphite (> 600 Ah $kg^{-1}$, > 2200 Ah $L^{-1}$).[13]

#### 2.2.2.4. Transition metal-based oxides

The spinel *lithium titanate ($Li_4Ti_5O_{12}$, LTO)* has been focused because of its safe, low reaction voltage, around 1.5 V (*vs.* $Li/Li^+$) and also fast kinetics. The formula can be written as $Li[Li_{1/3}Ti_{5/3}]O_4$ indicating that Li ions locate both tetrahedral (occupy the 8a sites) and octahedral (occupy the 16d sites) oxygen coordination.[73-74] It is a typical *insertion* or *addition-type material* and can be accommodated 3 mole of lithium per formula unit of LTO during lithiation via intercalation giving a theoretical specific

capacity of 175 mAh $g^{-1}$. Interestingly, it shows very little change in the cubic lattice parameters during cycling (zero-strain material), and also lithium ion diffusion coefficient is fairly high, thus can show fast kinetic performance at high current *C*-rates (15-30 *C*).[8, 75] However, the electronic conductivity is smaller by two orders of magnitude than lithium ion conductivity, which is still smaller than other transition metal oxides. In order to improve these conductivities, many efforts have been tried including introducing nanostructure with nanopores, conductive coating, such as carbon, TiN, and creation of $Ti^{3+}$ ions enabling the hopping of electronic charge carriers between the $Ti^{3+}$ and $Ti^{4+}$ ions in the lattice.[76-78] There are other examples for insertion-type transition metal oxides, such as $TiO_2$,[79-80] $MoO_2$,[9, 81-83] $V_2O_5$,[84-85] which can be used in high stable and safe lithium-ion batteries.

In contrast with insertion-type transition metal oxides, there are new type of transition metal-based oxides that can react with lithium through the *conversion reaction*. Poizot *et al.* in 2000 firstly reported the simple binary transition metal oxides with the rock salt structure (MO where M = Co, Cu, Ni, or Fe), having no free voids to intercalate lithium ions, and metallic elements (Co, Cu, Ni, or Fe) not forming alloys with lithium. However, they can react reversibly with lithium according to the followed reaction.[86]

$$MO + 2Li^+ + 2e^- \leftrightarrow M^0 + Li_2O$$

After this first paper, a thousand researches revealed that metal oxides that have several valence states also follows the conversion reaction.[87-90] The general reaction is re-written as in.

$$M_aO_b + nLi^+ + ne^- \leftrightarrow aM^0 + bLi_2O \ (n = 2b) \quad (4)$$

Full reduction leads to composite consisting of nanometric metallic particles (2-8 nm) dispersed in an amorphous $Li_2O$ matrix. Normally, the electrochemical reactivity of reverse reaction, although thermodynamically possible, is kinetically unexpected due

to the difficult task to reconvert $M^0 + Li_2O$ (solid-state phase) into metal oxide compound ($M_aO_b$). However, owing to the nanometric nature of this composite, that is the specific $M^0$ and $Li_2O$ particles confinement on a nanoscale, such reactions are shown to be highly reversible. With such an electrode configuration, the reaction mechanism easily can be ascribed to a simple acid-base reaction in which $Li_2O$ plays the role of oxygen reservoir and oxidant to oxidize $M^0$ (Fig. 3).[91]

Fig. 4 shows a typical voltage – capacity profiles of transition metal oxides which reacts with lithium through conversion reaction. There are three main reactions during lithiaiton: (i) insertion region (ii) flat-voltage region and followed by (iii) slope-voltage region. The first one is lithium ion insertion in the interstitial sites of transition metal oxide, which is dependent on the crystal structure of metal oxides. For example, rock-salt structure oxides cannot accommodate lithium ions by insertion reaction since they do not have any interstitial sites.

The second one shows a typical *two-phase reaction*: the breakage of bonds between metal and oxygen to be generated nanometric metals and lithium oxides. As mention above in equation (3) in *Chapter 2.1.*, reaction potential, or a flat-voltage *vs.* $Li/Li^+$, is determined by the change of the Gibbs free energy for reaction (4) as in:

$$\Delta G^0_{rxn} = 2n\Delta G^0_f(Li_2O) - \Delta G^0_f(M_aO_b) = -nFE^0 \quad (5)$$

The thermodynamic standard reduction potential of reaction (4) ($E^0$) is decided by the stability of $M_aO_b$, $\Delta G^0_f(M_aO_b)$, and/or the number of electrons and lithium ions involved reaction (4), n. The stability of $M_aO_b$ can be also expressed as the bond strength between metal and oxygen since the Gibbs free energy of formation means the relative stability of compounds compared ($M_aO_b$) with its elemental states (M, O). Therefore, the bond strength, the Gibbs free energy of reaction as well, can be a criteria for the flat-voltage, or main conversion reaction voltage in the first-cycle. Table 3 is summarized the Gibbs free energy of formation, the Gibbs free energy of reaction

calculated equation

[91]

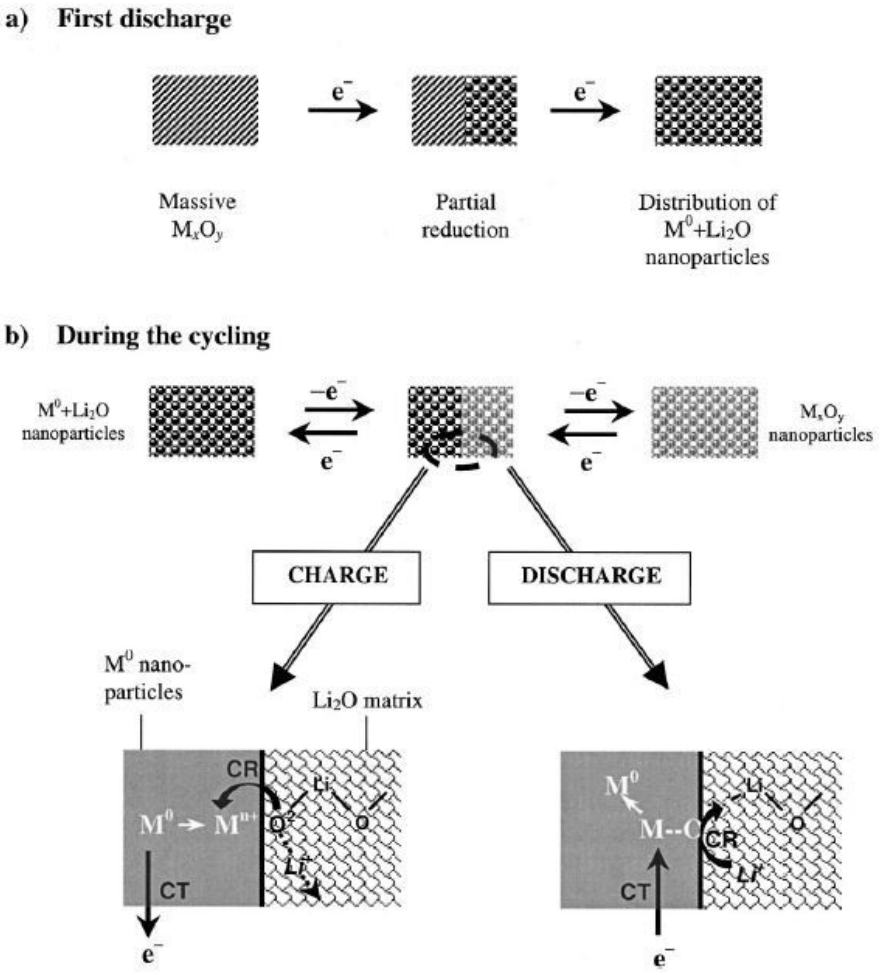


**Figure 3.** A schematic illustration for reaction mechanism of transition metal oxide which reacts with lithium through a conversion reaction: a) the first-cycle lithiation (discharge in the figure) and b) during the cycling. CT and CR means the charge transfer and the acid-base consecutive reaction,

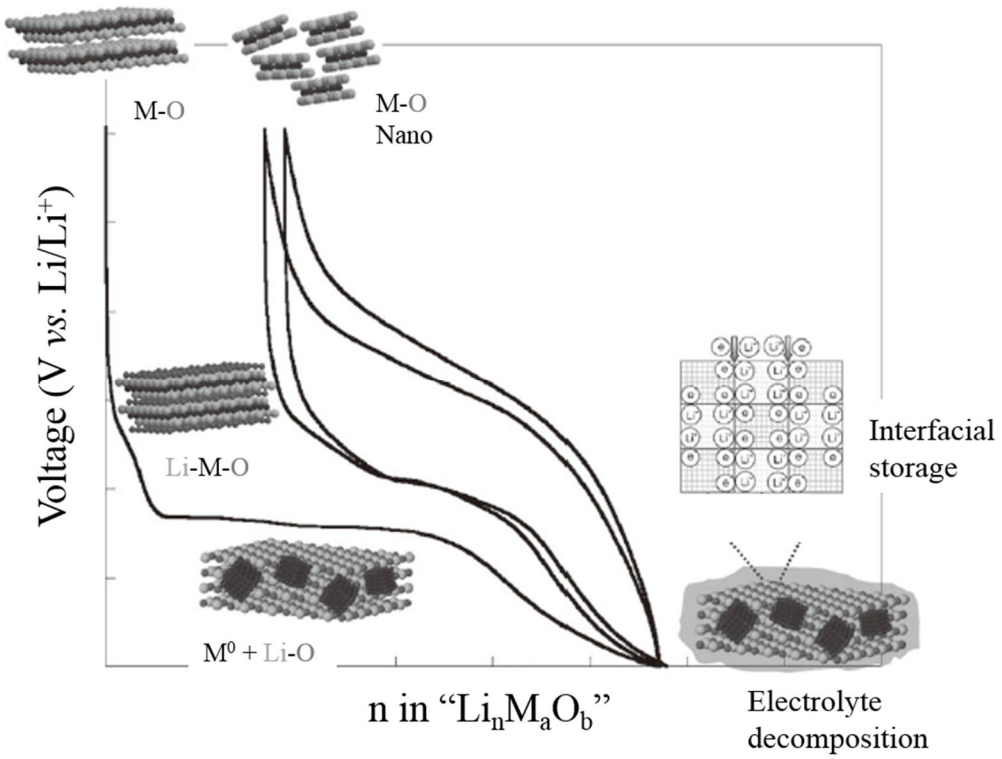


**Figure 4.** Typical voltage profile (voltage *vs.* composition profile) of transition metal oxide which reacts with lithium through a conversion reaction. The light gray, dark gray and black balls depict O, Li, and M, respectively.

[6]

**Table 3.** The standard Gibbs free energy of formation, reaction, and the standard reduction potential, and theoretical capacity for binary transition metal oxides.

| Compounds (Ref. [92]) | $\Delta G_f^0$ (kJ mol$^{-1}$) | $\Delta G_{rxn}^0$ (kJ mol$^{-1}$) | $E^0$ (V) | Specific capacity (mAh g$^{-1}$) |
|---|---|---|---|---|
| $Li_2O$ | -562 | - | - | - |
| $TiO_2$ | -890 | -234 | 0.606 | 1342 |
| VO | -404 | -158 | 0.819 | 801 |
| $V_2O_3$ | -1139 | -547 | 0.945 | 1073 |
| $VO_2$ | -1318 | 194 | -0.503 | 1293 |
| $V_2O_5$ | -1419 | -1391 | 1.442 | 1474 |
| $Cr_3O_4$ | -1531 | -717 | 0.929 | 975 |
| $Cr_2O_3$ | -1058 | -628 | 1.085 | 1058 |
| MnO | -363 | -199 | 1.031 | 756 |
| $Mn_2O_3$ | -881 | -805 | 1.391 | 1018 |
| $MnO_2$ | -465 | -659 | 1.708 | 1233 |
| FeO | -251 | -311 | 1.612 | 746 |
| $Fe_2O_3$ | -742 | -944 | 1.631 | 1007 |
| CoO | -214 | -348 | 1.803 | 715 |
| NiO | -212 | -350 | 1.814 | 718 |
| $Cu_2O$ | -148 | -414 | 2.145 | 375 |
| CuO | -128 | -434 | 2.249 | 674 |
| ZnO | -320 | -242 | 1.254 | 659 |
| NbO | -392 | -170 | 0.881 | 492 |
| $NbO_2$ | -795 | -329 | 0.852 | 858 |
| $Nb_2O_5$ | -1766 | -1044 | 1.082 | 1008 |
| $MoO_2$ | -533 | -591 | 1.531 | 838 |
| $MoO_3$ | -668 | -1018 | 1.758 | 1117 |
| $RuO_2$ | -280 | -844 | 2.187 | 806 |
| $Ag_2O$ | -11.2 | -550.8 | 2.854 | 231 |

(5), theoretical reaction voltage and specific capacity based on reaction (4) for various transition metal oxides.

The third one, slope voltage region, shows *additional capacity* exceeding the theoretical specific capacity (the number of lithium corresponding to the valence for metal oxide per formula unit). It is stemmed from the electrolyte decomposition at the surface of nanometric metal domain. In the negative electrode in LIBs, the electrolyte decomposition is inevitable due to the low reaction voltage, ~ 0 V (*vs.* $Li/Li^+$). Since nano-sized metal has a lot of surface area and catalytic ability to reduce organic species, there is an additional and severe electrolyte decomposition on the outside of *solid electrolyte interphase (SEI)*, by forming polymer/gel-like films, and such reaction is known as quite reversible.[93-94] J. Mayer group had been suggested the source of extra capacity as the capacitive charge storage at the surface nanometric metal.[95-97] However, this amount of extra capacity, around 200 mAh $g^{-1}$, cannot explain capacitive charge storage only, based on simple calculation reported by M. R. Palacin *et al.*.[98]

### 2.2.3. Electrolytes

In the LIBs, positive electrode and negative electrode are physically separated by a barrier. This barrier has to be electronically insulating in addition to being ionically conductive, so that mass transport of charge carriers (ionic species) through it can proceed to offset the charge separation incurred by the movement of electrons. This barrier is the *electrolyte*, and only in this manner the closed-loop across the cell can be maintained. Most LIBs utilize non-aqueous electrolyte solutions called *organic electrolytes*, which *lithium salts* are dissolved in *organic solvents*. As the electrodes in LIBs are porous composite electrodes, the liquid electrolyte must seep into the porous electrodes and transfer lithium ions smoothly at the interface between the liquid and solid phases. There are numerous organic solvents and lithium salts; however, a very limited number of materials fulfill the following physicochemical requirements for

practical use: (i) high electrolytic conductivity, (ii) high chemical and electrochemical stability, (iii) wide operational temperature range, (iv) high stability. Most compositions of electrolytes for LIBs are based on solution of one or more lithium salts in mixtures of two or more solvents.

#### 2.2.3.1. Lithium salts

The role of lithium salts in LIB cells is that it acts as the sources of lithium ions in electrolyte, so that participate in the redox reaction occurring at the surface of electrodes, making closed-loop. An ideal salts for LIBs should meet the following requirements: (i) complete dissolution and dissociation in the non-aqueous media, (ii) stable anion against oxidative decomposition at the positive electrode, (iii) inert anion to electrolyte solvents, (iv) nontoxic and stable against thermally induced reaction with electrolyte solvents and other cell components, (v) the formation of good SEI on the negative electrode, and (vi) the ability to passivate the electrolyte – Al interface to prevent corrosive pitting of the current collector during cell cycling to high voltage, i.e., > 3.6 V (*vs.* $Li/Li^+$).[17]

A number of lithium salts are well established what are used or have been previously used for LIB electrolytes, although many of these do not meet the necessary criterion for commercial battery electrolytes[99-100]: (i) $LiClO_4$: high ionic conductivity, solubility in aprotic solvents, thermal/electrochemical stability, and favorable SEI forming properties, but, no passivation of Al current collector. (ii) $LiPF_6$: used almost in commercial LIBs, showing the best balance of essential properties including conductivity, SEI forming, the protection of Al corrosion, however, the formation of HF which impact badly on cell performance and relatively low thermal stability. (iii) $LiAsF_6$: improved efficiency of lithium metal plating/stripping, similar properties with $LiPF_6$ but the potential hazards, especially $As^{3+}$ and $As^0$ states. (iv) $LiBF_4$: low conductivity than $LiPF_6$ due to the smaller dissociation constant, but less labile B-F

bond than P-F bond which results in less susceptible to hydrolysis and more thermally stable, thus there are attempts to replace $LiPF_6$ not only at elevated temperatures up to 50 $^oC$, but, surprisingly, also at low temperature as well.[101] (v) lithium bis(trifluoromethanesulfonly)imide, *LiTFSI*, $LiN(SO_2CF_3)_2$: TFSI anion has a high thermal stability and not susceptible to hydrolysis due to the very stable C-F bonds, but less conductive than $LiPF_6$ and strong corrosion on the Al current collector at high voltage.[102-103]

#### 2.2.3.2. Solvents

Solvents in LIBs act as medium to contain lithium ion moving during charge / discharge and electronic barrier between two electrodes. An ideal electrolyte solvent should meet the following minimal criteria: (i) able to dissolve salts with sufficient concentration, that is, a high dielectric constant (ε), (ii) low viscosity (η) for facile ion transport, (iii) inert to all cell components, (iv) remaining liquid in a wide temperature range (normally, -20 ~ 60 $^oC$), (v) sate, nontoxic and economical.[17]

Any solvents that have active protons must rule out since the nature of strongly reducing negative electrode, 0 ~ 0.2 V (*vs.* $Li/Li^+$) and strongly oxidizing positive electrode, 3 ~ 4.5 V (*vs.* $Li/Li^+$), respectively. Therefore, only organic solvents with polar groups such as carbonyl ($C=O$), nitrile ($C\equiv N$), sulfonyl ($S=O$), and ether-linkage ($-O-$) should be used. Among them, cyclic carbonate such as *propylene carbonate (PC)*, *ethylene carbonate (EC)* are commonly used in the commercial LIBs. In particularly, the unique position of EC as a LIB electrolyte was established in 1990 when Dahn and co-workers reported the fundamental difference between EC and PC. EC was found to form an effective protective film (SEI) on a graphite negative electrode, while PC exfoliates the graphene structure because of PC co-intercalation.[104]

However, these polar solvents have high viscosity due to interaction between

them and high melting point, for example, solid phase EC in room temperature. In 1994, Tarascon and Guyomard first describe to use a linear carbonate, *dimethyl carbonate (DMC)*, as a co-solvent with EC to solve viscosity and melting point issues. This nonpolar linear carbonates, *diethyl carbonate (DEC)*, *ethylmethyl carbonate (EMC)*, as well as DMC have low boiling points, low viscosity, and low dielectric constant. They can form homogeneous mixture with EC at any ratio, and the mixed electrolytes benefit from the suppression of melting temperature and the low viscosity and thus high ionic mobility.[105-106]

#### 2.2.3.3. Additives

Although Sony Corporation's batteries focused not only graphite negative electrode as the replacement of metallic lithium but also SEI on the graphite, intentional control of SEI was not considered in sufficient depth. The concept of SEI was suggested by Peled from Tel-Aviv University and Aurbach from Bar-Ilan University.[107-108] After 1999, in the industrial field, the concept of "*functional electrolytes*" was developed on the basis of intentional control of thick SEI and improvement of battery performance by adding small amount of various negative electrode additives. In addition, overcharge protection additives acting at the positive electrode also have been used in the commercial LIBs.

Following are many additive roles to be studied up to now. (i) Bulk electrolyte additive to enhance ion transport: using the ability of crown ether to coordinate with lithium ion, promotion the solvation of lithium salts in non-aqueous electrolyte and increase the solubility of lithium salts, for example, 12-crown-4 and 15-crown-5.[109-110] (ii) SEI forming agents on negative electrode: usually having high reduction potentials than bulk electrolyte, so that reduced on the negative electrode surface earlier than bulk electrolyte, resulting insoluble, compact, and having low impedance to lithium ion transport SEI films, for example, compounds containing unsaturated carbon-carbon

bond such as *vinylene carbonate (VC)*,[111-112] and carboxylic acid anhydrides, oxalates, sulfur-containing compounds. (iii) Overcharge protection agents on positive electrode: suppression for the increase in voltage of positive electrode by consuming charges through a redox shuttle process, for example, organometallic complexes consisting metal core (Fe and Co) coordinated organic ligands, anisole, alkylbenzenes, and halogen-containing benzene compounds.[113-114]

## 2.3. Energy efficiency in LIB

As mentioned in *Chapter 2.1.*, a rechargeable battery is a device that convert electric energy into chemical energy during charge, and reverse process during discharge. In such energy conversion processes, the energy efficiency is a key issue because nobody wants to use energy in battery lower than the amount of charging. The *energy efficiency* defined as the ratio of the discharged energy to the charged energy in the range of between discharge state and a certain *state-of-charge (SOC)* as in:[115]

$$\eta_{battery} = \frac{E_{out}}{E_{in}}$$

$$E_{in} = \int_{SOC(0)}^{SOC(t)} U_{charge} Q_n dSOC$$

$$E_{out} = \int_{SOC(0)}^{SOC(t)} U_{discharge} Q_n dSOC$$

where $\eta_{battery}$ is energy efficiency of battery, $E_{in}$ and $E_{out}$ are the charged and discharged energy, respectively. $U_{charge}$ and $U_{discharge}$ represent the cell voltage during charge and discharge, respectively, and $Q_n$ is standard capacity of the battery. SOC (0) is the initial state-of-charge when the battery begins to charge, SOC (t) is the terminal SOC when the process is complete. Energy efficiency is divided into two categories: voltage and

capacity efficiency.

### 2.3.1. Voltage hysteresis

Voltage efficiency, is somewhat unfamiliar. Instead, the voltage hysteresis is commonly used terminology to indicate efficiency related with cell voltage. The *voltage hysteresis* means the voltage difference in between charge and discharge. In fact, since cell voltage is determined according to the thermodynamics of positive and negative electrodes, it should be equal at the same SOC whether the battery is charged or discharged. However, in the current-flowed electrochemical cell, the kinetics also affects the cell voltages as well as thermodynamics. In other words, the cell voltage is different with the value calculated from thermodynamic one, because it is no longer equilibrium state. We call such voltage deviation as over-potential, or polarization, and it is dependent on the amount of current.

In the transition-metal oxide negative electrodes which react with lithium through conversion reaction, such voltage hysteresis is dominant due to its intrinsic difficulty of de-lithiation process, bond reforming reaction. As shown in reaction (4) in *Chapter 2.2.2.4.*, the reverse reaction of conversion reaction (de-conversion reaction) occurs in the surface between nano-size metal particle and $Li_2O$ by acid-base reaction, or metal-oxygen solid-state diffusion reaction. Although thermodynamically possible, it is difficult task kinetically to convert metal and $Li_2O$ (solid-state phase) into metal oxide ($M_xO_y$). The confinement of metal and $Li_2O$ with nanoscale decrease the activation energy considerably, therefore de-conversion reaction is feasible.[91] However, despite the reduced activation energy, the large voltage hysteresis, around 1.0 V (*vs.* $Li/Li^+$), is inevitably involved and it causes the low energy efficiency. Such voltage hysteresis can be reduced by using sulfides, nitrides, fluorides, and phosphides rather than oxide because $Li_nX$ (X=S, N, F, P) is highly reactive and more easily oxidized than $Li_2O$.[91-92]

### 2.3.2. Coulombic efficiency

The second category is about capacity efficiency. Similarly, rather than capacity efficiency, the Coulombic efficiency is more widely used. The *Coulombic efficiency* defined as the ratio of discharged capacity to charged capacity in each cycle. There are many reasons why the Coulombic efficiency is not 100 % in every cycle, in both positive and negative electrodes. (i) Negative electrode: (i-1) the irreversible charge consumption, or electrolyte decomposition (reduction), at the surface of negative electrode during charge (lithiation), and (i-2) lithium ion trapping in the active material due to the contact losses between active materials or with current collector during discharge (de-lithiation), especially large volumetric change materials such as Si.[116] (ii) Positive electrode: (ii-1) irreversible phase transition of the transition metal oxide during extraction of lithium ions (charge), resulting in no 'empty' space for re-insertion of lithium ion, (ii-2) the irreversible electrolyte oxidation at the surface of electrode having highly oxidation condition, and (iii-3) active material losses due to the dissolution of transition metal ions, especially $Mn^{2+}$ in LMO.[117]

The Coulombic efficiency is more important in full-cell rather than half-cell because, contrary to half-cell in which almost infinite amount of lithium is presented due to lithium metal counter electrode, this is limited in full-cell. If the Coulombic efficiency in every cycle is not reached 100 %, the cycleability should be fading due to the depletion of lithium ion sources in full-cell.

#### 2.3.2.1. The initial Coulombic efficiency

The *initial Coulombic efficiency (ICE),* which is the Coulombic efficiency in the first cycle, is the most important parameter since most of irreversible lithium ion consumptions occur in the first cycle. The ICE is much lower in the negative electrode than positive electrode, especially high-capacity negative electrode material such as

lithium alloying materials and conversion reaction-type transition metal oxides. Since such amount of irreversibly consumed charges in the negative electrode are supplied from the positive side, extra positive electrode materials which cannot be used in subsequent cycling are should be added, and it results in the decrease in specific capacity of battery.

In conversion reaction, the ICE is extremely low, around 60 %, and there are two main reasons. (i) Large amount of electrolyte decomposition at the surface of newly formed nano-size metal particles during lithiation. Metals, especially 3d or 4d transition-metals, are known to be a catalyst for decomposition of organic species. In addition, since the surface area of metal particles formed after lithiation is extremely large (3 ~ 5 nm scale metal domain), the catalytic effect is dramatically increased, which results in severe electrolyte reduction or decomposition in highly reducing atmosphere. (ii) During de-lithiation, bond reforming reaction between nanometric metal and oxygen in $Li_2O$ is kinetically tough task, similar with large voltage hysteresis, mentioned above. Thus, the ICE of conversion reaction-type metal oxide is low, and therefore it should be enhanced to be used as the high-capacity negative electrode for commercialized LIBs.

# 3. EXPERIMENTAL

## 3.1. Synthesis of active materials

### 3.1.1. Amorphous molybdenum oxides

The amorphous molybdenum oxides were prepared by modifying the previously reported procedure.[9, 118] In detail, 50 mL of 0.25 *M* $K_2MoO_4$ solution was prepared by dissolving 3.0 g of $K_2MoO_4$ (98 %; Sigma-Aldrich) in distilled water, and the solution pH was adjusted to be 0.8 or 4.0, respectively, with concentrated HCl (35 %; Dae-Jung). These pH values were chosen on the basis of that molybdenum oxide precipitates within the pH range of 0.8 ~ 4.0. Separately, 50 mL of 2.7 *M* $KBH_4$ (reducing agent) solution was prepared by dissolving 7.3 g of $KBH_4$ (98 +%; Sigma-Aldrich) in dilute KOH (85 +%; Dae-Jung) solution (pH = 11.0). For the reduction reaction, the $KBH_4$ solution was slowly added into the $K_2MoO_4$ solution using a micro-burette while the solution pH being maintained at the predetermined value by adding concentrated HCl. The resulting precipitates were collected by filtering and washed with hot distilled water. The precipitates were then dried at 300 °C for 2 h under vacuum. To identify oxides, heat treatment at 500°C in Ar atmosphere was conducted. The amorphous molybdenum oxides prepared at pH = 0.8 and 4.0 were named aM2-0.8 and aM2-4, respectively. In *Chapter 4.1.*, the results will be examined. As comparison groups, $MoO_2$ (99 %; Sigma-Aldrich) and $MoO_3$ (99.5 +%; Sigma-Aldrich)

were chosen.

### 3.1.2. Ball-milled $MoO_3$

High-crystalline and micro-sized molybdenum trioxide ($MoO_3$) powder was prepared by a solid-state reaction. In detail, ammonium heptamolybdate tetrahydrate, $(NH_4)_6Mo_7O_{24}•4H_2O$ (81-83 %, Alfa), was heated at 600 $^oC$ for 10 h in an air atmosphere. For hundreds of nanometric $MoO_3$, the heating temperature was decreased to 500 $^oC$ with same time and atmosphere. Ball-milling of $MoO_3$ was conducted by using *Planetary Micro Mill PULVERISETTE 7 premium line (FSITSCH)* with a low speed, 300 rpm, to minimize the reduction of $MoO_3$. Ball-milling time, which is a variable in experimental, is selected as 0 min (bare), 5 min, 30 min, 2 h, 4 h. Among these samples, bare and 30 min samples were chosen in detail electrochemical and spectroscopic analysis. In *Chapter 4.2.*, the results will be examined.

### 3.1.3. $Li_2MO_3$ (M=Mo or Ru)

The $Li_2MoO_3$ powder was synthesized by a solid–state reaction. In detail, a stoichiometric mixture of $Li_2CO_3$ (99 +%; Sigma-Aldrich) and $MoO_3$ (99.5 +%; Sigma-Aldrich) was heated at 900 °C for 6 h in an Ar + $H_2$ (5 %) atmosphere.[119] The $Li_2RuO_3$ powder was also obtained by a solid–state reaction in which a stoichiometric mixture of $Li_2CO_3$ and $RuO_2$ (99.9 %; Sigma-Aldrich) was heated at 900 °C for 24 h in air.[120] To prepare a physical mixture of $MoO_2$ (99 %; Sigma-Aldrich) and $Li_2O$ (97 %; Sigma-Aldrich), *Planetary Micro Mill PULVERISETTE 7 premium line (FSITSCH)* was used with 500 rpm for 24 h. Ball-mill bowl containing sample was sealed in a Ar-filled glove-box to suppress the oxidation of $MoO_2$. As comparison groups, 30 min ball-milled $MoO_2$ (99 %; Sigma-Aldrich) and $MoO_3$ (99.5 +%; Sigma-Aldrich) with 300 rpm were chosen. In *Chapter 4.3.*, the results will be examined.

## 3.2. Electrochemical analysis

### 3.2.1. Electrode preparation

The composite electrodes were fabricated by using an active material powder, Super P (carbon black) as a conducting agent, and carboxymethyl cellulose (CMC) as a binder with a weight ratio of 80:10:5. The active material and Super P were mixed with a CMC solution (1.2 *wt.%* in distilled water) to make a slurry. To the slurry, 5 *wt.%* of styrene-butadiene resin (SBR) was added to enhance binding ability. The slurry was then coated on copper foil (current collector, thickness: 20 μm) and dried under vacuum at 120 $^{o}$C for 12 h. In *Chapter. 4.3.*, $RuO_2$ and $Li_2RuO_3$ electrode were fabricated by using titanium foil as current collector.

### 3.2.2. Cell preparation

Electrochemical performance was evaluated by using a two-electrode 2032-type coin cells with a composite electrode as the working electrode and lithium foil (Cyprus Co.) as the counter and reference electrode. The used electrolyte was 1.0 *M* $LiPF_6$ dissolved in a mixture of ethylene carbonate (EC) and diethyl carbonate (DEC) with 1:1 volume ratio. A porous polypropylene (PP) – polyethylene (PE) – PP multi-layer film was used as the separator. The cells were assembled in an Ar-filled glove-box.

### 3.2.3. Galvanostatic charge/discharge cycling

A WonATech battery cycler (WBCS3000) was used for the galvanostatic charge/discharge test in a temperature-controlled oven (room temperature, 25 $^{o}$C).

Cycling was conducted at a current density of 100 mA $g^{-1}$ over the voltage range of (i) 0.01 ~ 3 V (*vs.* $Li/Li^+$) in *Chapter 4.1.*, (ii) 0 ~ 3 V (*vs.* $Li/Li^+$) in *Chapter 4.2.*, (iii) 0 ~ 4 V (*vs.* $Li/Li^+$) for $RuO_2$ and $Li_2RuO_3$ electrodes and 0 ~ 3 V (*vs.* $Li/Li^+$) for other oxide electrodes in *Chapter 4.3.*. For complete lithiation in (ii) and (iii), a constant voltage step at 0 V (*vs.* $Li/Li^+$) was added until the current density decayed to 10 mA $g^{-1}$.

### 3.2.4. Differential capacity (dQ/dV) plot

The dQ/dV plot is obtained by taking the derivative of the inverse of voltage – capacity profile. Through the simple mathematics, plateaus in voltage – capacity profile are converted into peaks in dQ/dV plot, and therefore it has advantage for the identification of reaction voltage with relatively high resolution. The resolution is determined by the number of points for interpolation, and in this study, lithiation and de-lithiation dQ/dV plots are obtained by interpolation with 100 points and 50 points on the voltage range of 0 ~ 3 V (*vs.* $Li/Li^+$), respectively.

### 3.2.5. Galvanostatic intermittent titration technique (GITT)

GITT is a technique to examine the change of voltage according to turn-on or -off of the current. From this technique, the difference between thermodynamics, when the current is zero, and real situation, when the current flow, can be obtained, that is kinetics. In this study, the current pulse of 100 mA $g^{-1}$ was injected for 10 min to measure the closed-circuit voltage (CCV) and turned off for 50 min to measure the quasi-open circuit voltage (QOCV). This sequence was repeated within the voltage range of 0 ~ 3 V (*vs.* $Li/Li^+$), and the constant voltage was injected at the 0 V (*vs.* $Li/Li^+$) until 10 mA $g^{-1}$ current-cut. The cell resistance was calculated from the

difference between QOCV and CCV divided by the injected current density.

### 3.2.6. Electrochemical voltage spectroscopy (EVS)

EVS, or potentiostatic intermittent titration technique (PITT) is a technique that constant voltage is applied in the cell until the current decay to a threshold current, and it moves to the next constant voltage injection step. Since threshold current and voltage step size is small enough, the obtained voltage against the composition of charge in the electrode is close to the thermodynamic value and its resolution is high. In this study, the voltage step of 10 mV was applied in the cell and moved to the next step after the current decayed to 10 mA $g^{-1}$.

## 3.3. Characterization

### 3.2.1. The analysis of physical properties

BET: The surface area of oxides were confirmed by Brunauer-Emmett-Teller (BET) method using Micromeritics analyzer (ASAP 2000) at 77 K with $N_2$ as analysis adsorptive.

TGA: The thermogravimetric analysis (TGA) was performed using a TA Instrument Q600 simultaneous DTA/TGA analyzer at a heating rate of 10 °C $min^{-1}$ under air and $N_2$ atmosphere.

### 3.2.2. Microscopic investigation

FE-SEM: Particle morphology and size were examined by using a field emission

scanning electron microscopy (FE-SEM, JEOL JSM-6700F). For the images of *ex-situ* electrodes, the cells were disassembled and washed with DMC in the Ar-filled glove-box.

TEM: Transmission electron microscopy (TEM, JEOL JEM-3010) was used to detect tens of nanometric particles with high resolution. Its acceleration voltage is 300 kV.

### 3.2.3. Structural analysis

XRD: The X-ray diffraction (XRD) patterns were obtained by a D8-Brucker diffractometer equipped with Cu-$K_\alpha$ radiation (1.54056 Å) operated at 40 kV and 40 mA with a 5 degree $min^{-1}$ continuous scanning mode. The XRD patterns of *ex-situ* electrodes were recorded using a high-power XRD (D-MAX2500-PC, Rigaku) operated at 50 kV and 200 mA with the same scan speed continuous mode.

XAS (X-ray absorption spectroscopy): The Mo K-edge X-ray absorption near-edge structure (XANES) spectra were obtained at a 7D XAFS beam-line at the Pohang Light Sources (PLS) with a ring current of 120 ~ 170 mA at 2.5 GeV. The light source was detuned to 80 % of the initial intensity to eliminate high-order harmonics. A Si (111) was used as a monochromator and the data were collected in a transmission mode using a gas-filled ionization chamber (30 % $N_2$ and 70 % Ar) as a detector. Energy calibration for Mo absorption edge was conducted using the data obtained from a molybdenum metal thin film. The extended X-ray absorption fine structure (EXAFS) spectra were obtained from the data-processing of XANES data by using Athena (Ifeffit) program.

# 4. RESULTS AND DISCUSSION

## 4.1. Electrode performance of amorphous molybdenum oxides of different molybdenum valence for lithium-ion batteries

Until now, graphite has been the most commonly used negative electrode for LIBs. Although the commercialized graphite negative electrode has various advantages, it only show one electron capacity per six carbon atoms ($LiC_6$), which results in small specific capacity and thus energy density (theoretical specific capacity of graphite: 372 mAh $g^{-1}$).[57, 121] To overcome these obstacles, negative electrode materials that can take and release more than one electron per molecule have been sought. Transition metal oxides ($MO_x$ with M = Fe, Co, Ti, V, etc.) are promising candidates, because

transition metal ions in oxides can react with more than one electron.[86, 92, 122-125] As mentioned in *Chapter 2.2.2.4.*, transition metal oxides react with lithium in two ways: conversion and insertion reaction. One characteristic for the conversion reaction-type metal oxide is its high specific capacity which amount corresponds to the valence of metal ion. For example, since Co valence in CoO is +2, CoO is lithiated by taking two $Li^+$/electrons per formula unit as in: $CoO + 2\ Li^+ + 2\ e^- \rightarrow Co + Li_2O$. Note that the metal – oxygen bond in metal oxide should be broken for such conversion reaction. In contrast, owing to the strong bond between metal and oxygen, some of transition metal oxide cannot react with lithium through the conversion reaction, rather take lithium ion in the crystallographic storage sites, what we called as the insertion reaction. Molybdenum oxides are good examples; according to the Mo valence, $MoO_3$ reacts with lithium through the conversion reaction at a low voltage, < 0.5 V (*vs.* $Li/Li^+$), but $MoO_2$, on the other hands, only take lithium ions at 1.5 V (*vs.* $Li/Li^+$) by the insertion reaction, which is due to the difference in bond strengths of $MoO_3$ and $MoO_2$ [81, 126-129] (bond dissociation energy of Mo-O in $MoO_3$ = 565 kJ $mol^{-1}$ *vs.* 678 kJ $mol^{-1}$ for Mo-O in $MoO_2$ [130]).

As mentioned above, since crystalline materials store lithium ion only in their crystallographic sites, the lithiation capacity is limited for the insertion-type metal oxides. Thus, increase in the specific capacity can be achieved by reducing the degree of crystallinity to create additional storage sites. It is known that carbonaceous materials, such as a soft and a hard carbon, have various defect sites than can store the

additional lithium ions as well as crystallographic sites and they show higher specific capacity than the graphite.[57, 121] An amorphization of transition metal oxides also enhances specific capacity by introducing bulk defects (vacancies and void spaces) and surface defects in host materials.[9, 118, 131] In addition to the advantage of high specific capacity, an amorphous material also has the good lithium ion mobility which directly yields superior rate performance.[9, 132] Moreover, since the conversion-type metal oxide shows poor Coulombic efficiency behavior, especially in the first cycle, the amorphous materials which take lithium by insertion reaction also have advantages in the aspects of Coulombic efficiency.

The electrode performances of the stoichiometric molybdenum oxides (for instance, $MoO_2$ and $MoO_3$) in either crystalline or amorphous form are reported in the literature.[81, 83, 126, 133-138] However, there are only few reports on the non-stoichiometric ones (for instance, $MoO_{2+\delta}$ and $MoO_{3-\delta}$) in their amorphous form. This study demonstrates that electrochemical performance of the amorphous molybdenum oxide can be altered by controlling synthetic parameters, especially the pH. In preparing transition metal oxides by precipitating aqueous precursors through the reducing agent, the solution pH is one of the most important parameters because the reducing power is dramatically affected by the pH. The pH condition determines the physical properties of the synthesized oxide, such as particle size, Mo valence, and ultimately reaction mechanism with lithium. Through the control of reaction mechanism of amorphous metal oxides, whether conversion or insertion, the electrochemical performance

including cycle performance and initial Coulombic efficiency can be improved.

Fig. 5 shows the field emission scanning electrons microscopy (FE-SEM) images of synthesized amorphous molybdenum oxides (designated as aM2-0.8 in pH 0.8, aM2-4 in pH 4) and crystalline $MoO_3$ (Sigma-Aldrich, 99.5 +%, designated as cM3). Apparent particle sizes of them are 1-10 μm, 100-500 μm and 5-20 μm, respectively. As seen in Fig. 6, the X-ray diffraction (XRD) patterns of aM2-0.8 and aM2-4 (marked as 300 °C vacuum 2 h in Fig. 6a and 6b) show the amorphous nature of these materials. A heat treatment in Ar atmosphere can identify the nature of aM2-0.8 and aM2-4 as molybdenum oxides, which are mainly composed of $MoO_2$ phase with small portion of $Mo_4O_{11}$ (Fig. 6a) and $K_2Mo_3O_{10}$ (Fig. 6b), respectively. The qualitative analysis of each valence of aM2-0.8 and aM2-4 can be carried out by comparing the phases after annealing: the oxidation state of aM2-4 is higher than that of aM2-0.8. However, the quantitative analysis of the valence through XRD analysis of annealed sample is inaccurate due to the reducing nature of high-temperature Ar atmosphere. The crystal cM3 shows high crystallinity (Fig. 6c).

To identify the Mo valence, thermogravimetric analysis (TGA) is conducted for two amorphous samples. The Mo valence can be calculated by monitoring the weight change after annealing in air atmosphere. The weight gain in Fig. 7 must be due to the oxygen uptake ultimately be $MoO_3$. However, since it was synthesized in aqueous solution, there are water and/or hydroxyl groups in the surface and bulk, which can also alter the weight percent curve. Therefore, the TG curve acquired in inert

atmosphere should also be needed to ascertain the pure oxygen gain. As indicated in Fig. 7, oxygen gain is 10 *wt.*%

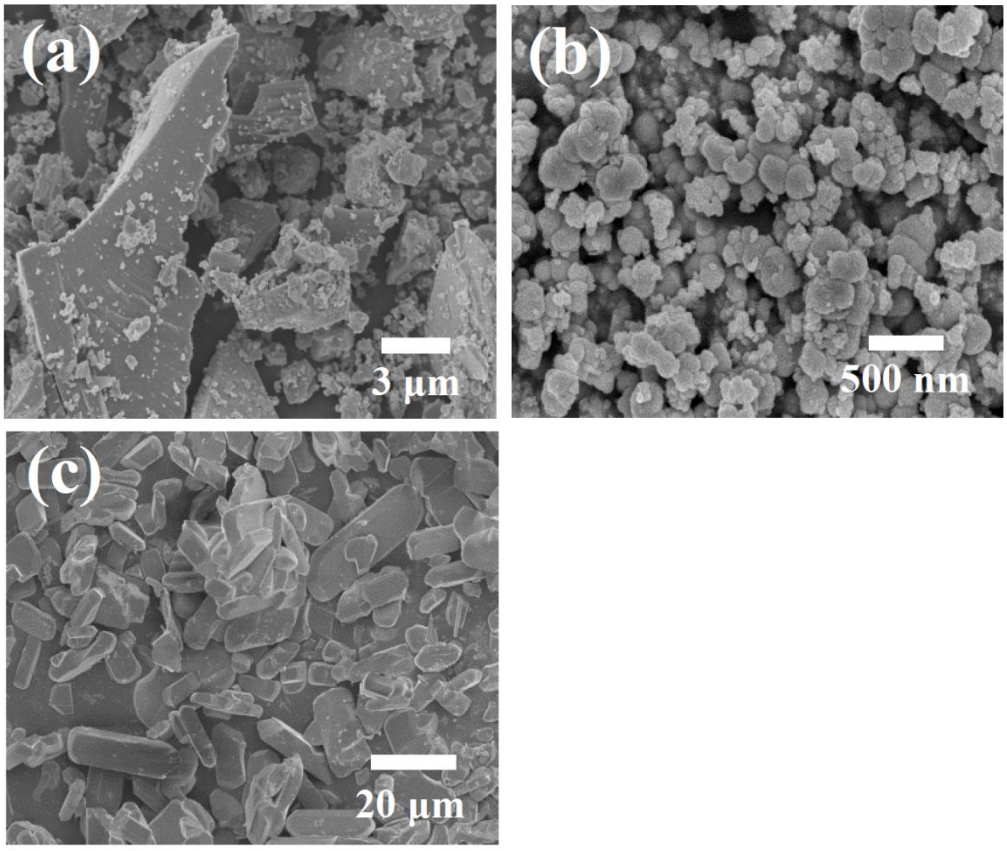


**Figure 5.** FE-SEM images of (a) aM2-0.8, (b) aM2-4, and (c) cM3, respectively.

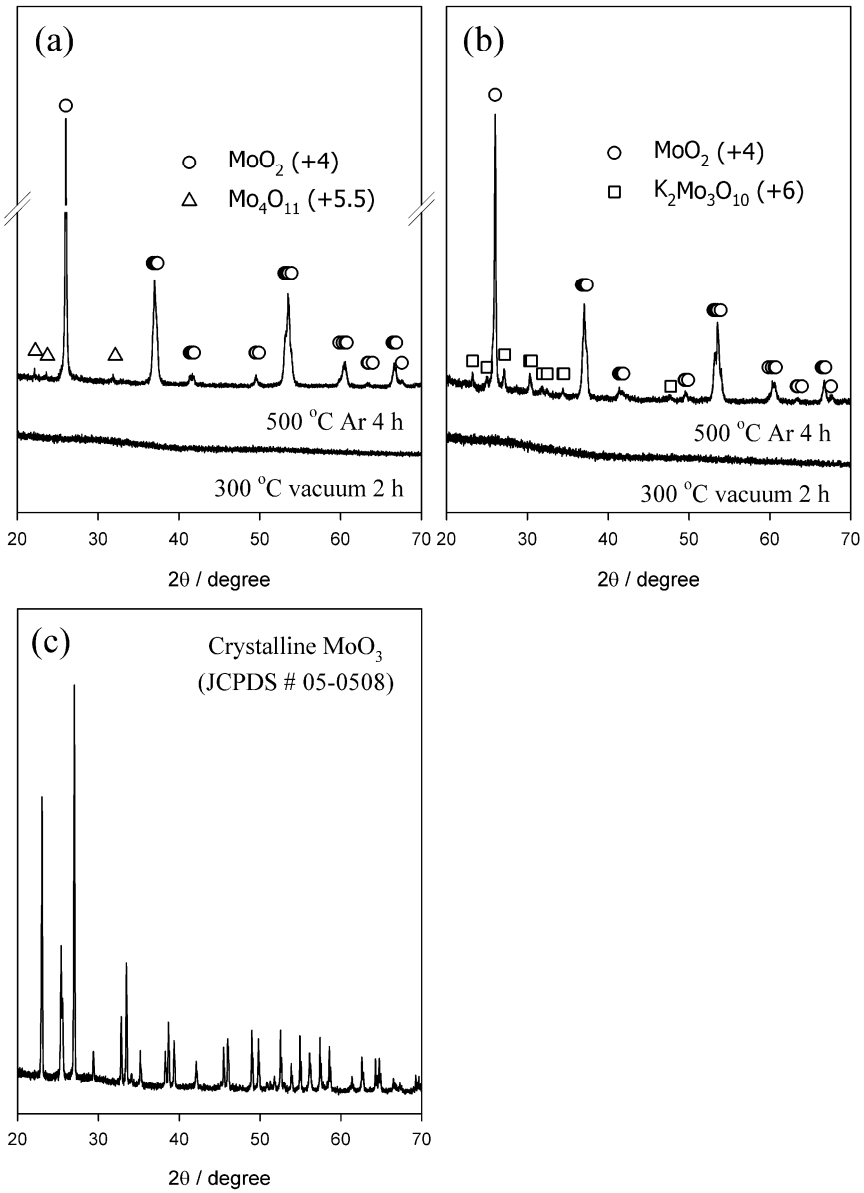


**Figure 6.** The XRD patterns of (a) aM2-0.8, (b) aM2-4 as prepared and after heat treatment, and (c) cM3. Peaks are assigned by the references: $MoO_2$ (JCPDS # 86-0135), $Mo_4O_{11}$ (JCPDS # 05-0337), and $K_2Mo_3O_{10}$ (JCPDS # 37-1467).

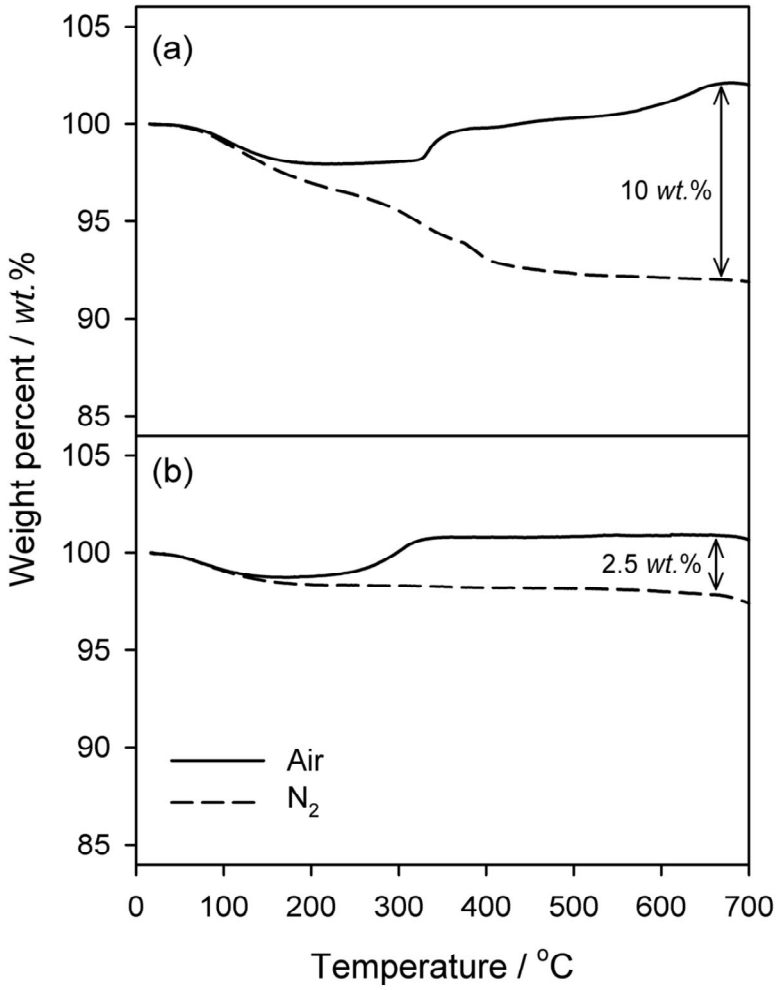


**Figure 7.** TG analysis of (a) aM2-0.8 and (b) aM2-4 in air and $N_2$ atmosphere, respectively. Oxygen gains are indicated in both figures.

for aM2-0.8and 2.5 *wt.*% for aM2-4, from which the average oxidation state of Mo is calculated to be +4.3 and +5.5, respectively.

Mo K-edge X-ray absorption near-edge structure (XANES) spectra are also used to estimate the Mo valence. Fig. 8a shows the normalized Mo K-edge XANES spectra for three samples. As a reference, the data obtained from the crystalline $MoO_2$ (Sigma-Aldrich, 99 %, designated as cM2) is also provided. From the position at the half-height of main absorption peak, the Mo K-edge shift is calculated with respect to the peak position for molybdenum metal.[139] The quantitative analysis of the valence can be feasible by plotting the average Mo oxidation state against the Mo K-edge shift (Fig. 8b). As shown in Fig. 8b, the average Mo valence of aM2-0.8 and aM2-4 is assessed to be +4.4 and +5.5, respectively. These values are very close to those obtained from the TG analysis within the error range of 3 %. Therefore, the non-stoichiometry (δ in $MoO_{2+\delta}$) for two samples is calculated to be 0.2 and 1.75, respectively.

As illustrated in the *Chapter 3.1.1.*, two amorphous samples of different Mo valence were prepared by changing the solution pH. This pH-dependent Mo valence can be accounted for from the following reducing reaction.

$$MoO_4^{2-} + BH_4^- + 2H^+ \rightarrow MoO_2 + BO_2^- + 3H_2 \quad (5)$$

In this reaction, the starting material ($MoO_4^{2-}$, Mo valence: +6) is reduced by $KBH_4$ to eventually be $MoO_2$ (Mo valence: +4). Meanwhile, $BO_2^-$, which is the product in reaction (5), tends to increase the solution pH. Hence, the reduction is favored at lower

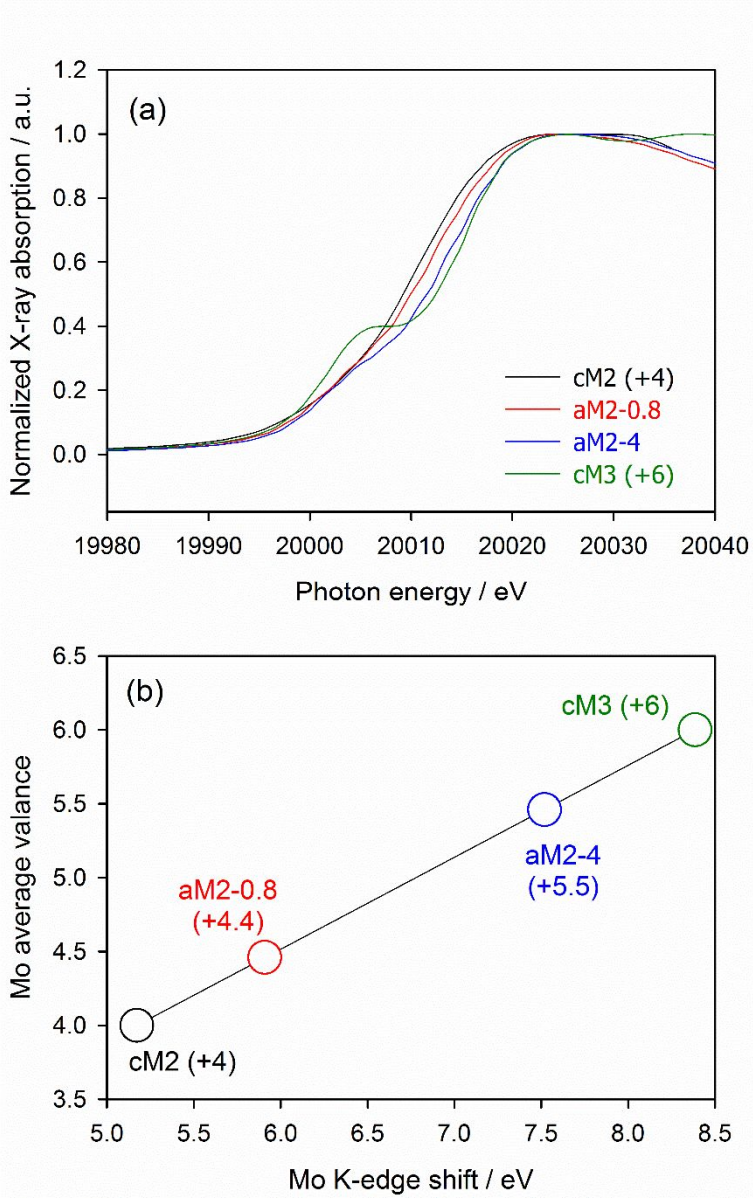


**Figure 8.** (a) The normalized XANES for cM2 (+4), aM2-0.8, aM2-4 and cM3 (+6). (b) The relationship between Mo K-edge shift energy derived from (a) and Mo valence.

pH (high $H^+$ concentration).[118, 140] In this work, the sample prepared at lower pH (aM2-0.8) exhibits a lower Mo valence in accordance with reaction (5). The opposite is true for the sample prepared at higher pH (aM2-4), higher Mo valence.

The galvanostatic charge/discharge voltage profiles of aM2-0.8, aM2-4 and cM3 electrodes are depicted in Fig. 9. The first-cycle lithiation / de-lithiation capacity delivered by these electrodes are 1019 / 836, 1109 / 930 and 1320 / 919 mAh $g^{-1}$, respectively. The first-cycle lithiation capacity delivered by three electrodes exceed their Mo valence owing to the lithiation capacity contribution from the conducting agent and the irreversible charge consumption associated with electrolyte decomposition. Note that, the capacity is roughly proportional to the Mo valence for three electrodes; +4.4 (aM2-0.8) < +5.5 (aM2-4) < +6.0 (cM3). The discussion on this feature will be advanced in the later section. The first and second-cycle voltage profiles of aM2-0.8 and aM2-4 electrodes, depicted in Fig. 9a and 9b, respectively, show a similar trend. A closer inspection of the second profiles of three electrodes, however, it is revealed that aM2-0.8 electrode behaves differently from aM2-4 and cM3 electrodes.

To understand the reaction mechanisms of aM2-0.8 and aM2-4 electrodes precisely, the differential lithiation and de-lithiation capacity (dQ/dV) plots are obtained as in Fig. 10. The cM3 electrode is a typical example that react with lithium through both the insertion and conversion reaction around 2 ~ 2.5 V (*vs.* $Li/Li^+$) and 0.3 ~ 0.4 V (*vs.* $Li/Li^+$), respectively. The peak from the conversion reaction in the second cycle is located at a lower voltage than that in the first cycle. It is a characteristic of

$MoO_3$ that

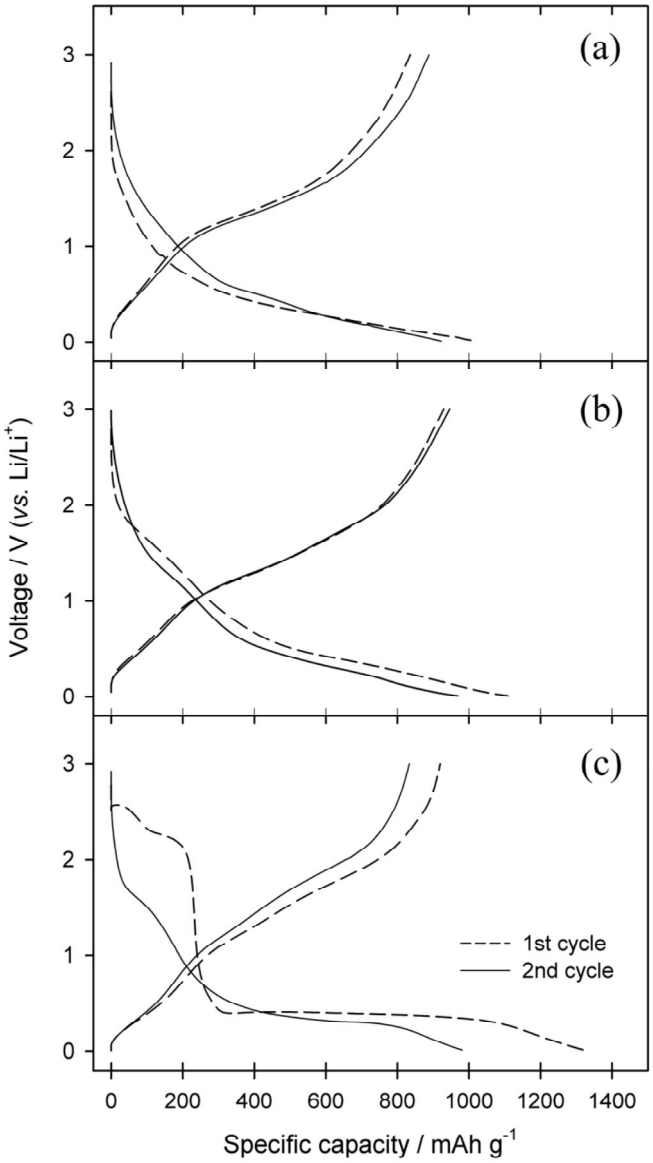


**Figure 9.** The first- and second-cycle voltage – capacity profiles of (a) aM2-0.8, (b) aM2-4, and (c) cM3 electrodes over the voltage range of 0.01 ~ 3.0 V (*vs.* $Li/Li^+$).

Mo metal and $Li_2O$ formed after the first-cycle lithiation does not fully oxidize up to $MoO_3$ during the first-cycle de-lithiation, resulting in $MoO_2$-like phase formed instead of $MoO_3$. Since this $MoO_2$-like phase has stronger bond dissociation energy than $MoO_3$, the activation energy for bond cleavage is larger, which results in that the conversion reaction appears at a lower voltage in the second cycle than that in the first cycle.[127] The much reduced peak area for the conversion reaction, 0.3 ~ 0.4 V (*vs.* $Li/Li^+$) in Fig. 10c, supports the incomplete de-lithiation to $MoO_3$ in the first cycle.

The aM2-4 and cM3 electrodes show similar behavior in several aspects. In the both dQ/dV plots, a single lithiation peak below 0.5 V (vs. $Li/Li^+$) appears, and the second lithiation peak is positioned at a lower voltage than that in the first cycle. Besides, two broad de-lithiation peaks appear at around 1 ~ 2 V (*vs.* $Li/Li^+$) (Fig. 10e and 10f). These similarities can be ascribed to the similar Mo valences of aM2-4 and cM3. Therefore, it can be deduced that both aM2-4 and cM3 electrodes react with lithium through a similar conversion reaction. The aM2-0.8 electrode, however, shows a different dQ/dV behavior compared with aM2-4 and cM3 electrodes, especially below 0.5 V (*vs.* $Li/Li^+$) for lithiation and 1 ~ 2 V (*vs.* $Li/Li^+$) for de-lithiation, as shown in Fig. 10a and 10d, which is an evidence that aM2-0.8 electrode reacts with a different mechanism. Since the Mo oxidation state of aM2-0.8 is closed to $Mo^{4+}$, aM2-0.8 electrode should follows the reaction mechanism of amorphous $MoO_2$ electrode, which is lithiated by the insertion reaction rather than the conversion reaction, as reported previous study.[9] Depending on the Mo valence in amorphous molybdenum

oxide, the

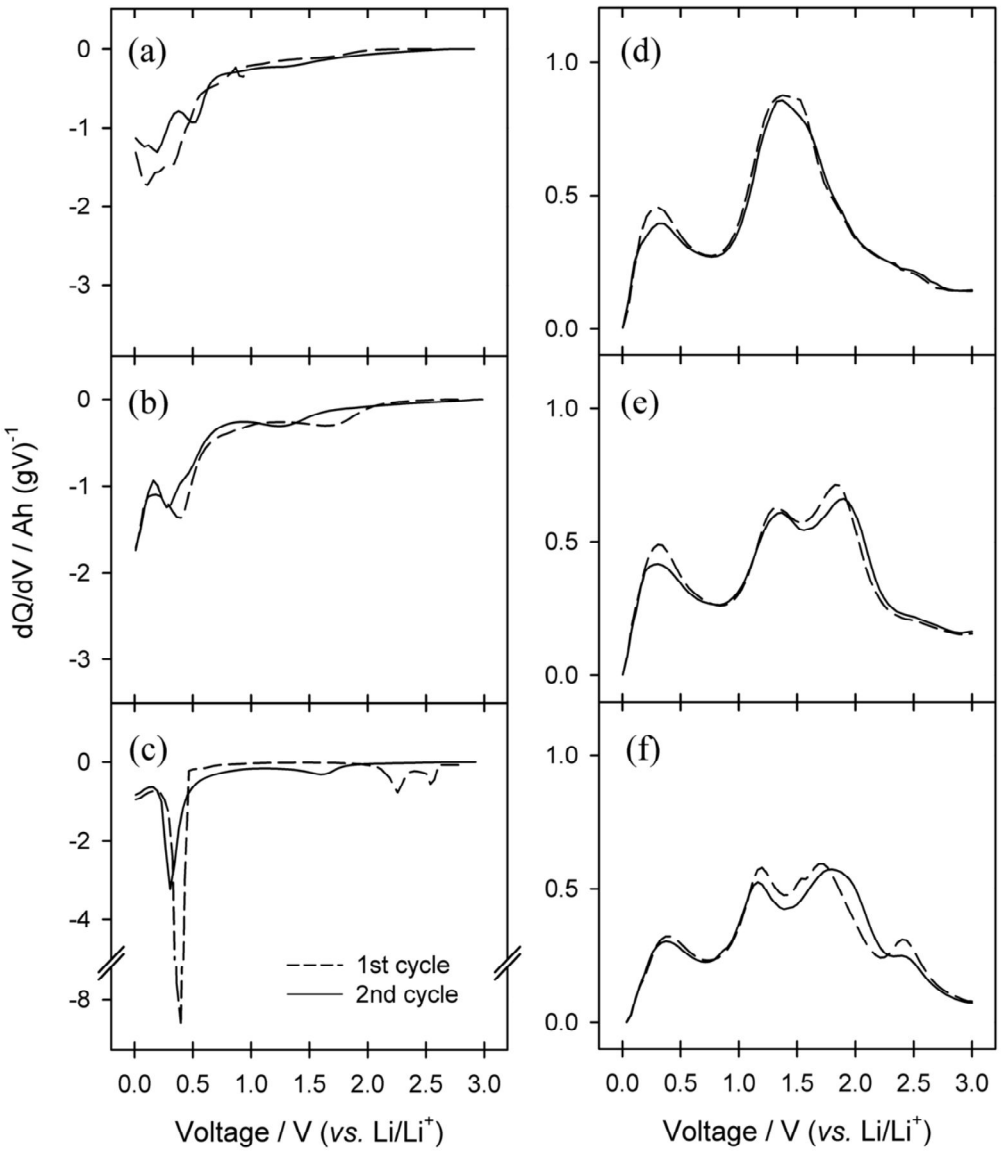


**Figure 10.** The first- and second-cycle differential capacity (dQ/dV) plots of (a) aM2-0.8, (b) aM2-4, and (c) cM3 electrodes for lithiation, and (d) aM2-0.8, (e) aM2-4, and (f) cM3 electrodes for de-lithiation, respectively.

reaction mechanism can change, just as cM2 and cM3.

In fact, on a closer view, three electrodes show similar peaks below 0.8 V (*vs.* $Li/Li^+$) in the de-lithiation dQ/dV plot. To identify the nature of this peak, the control of cut-off voltage in the de-lithiation was conducted (Fig. 11). After full lithiation and de-lithiation in the first cycle, and full lithiation in the second cycle, electrodes are de-lithiated up to only 0.8 V (*vs.* $Li/Li^+$). Fig. 11 reveals that the main peak in the third lithiation is absent, indicating the main oxidation reaction in the second de-lithiation do not occur due to the low cut-off voltage. However, broad peaks below 0.8 V (*vs.* $Li/Li^+$) in third de-lithiation still appear in all electrodes. It is very likely that these peaks stem from the de-lithiation of forced-stored lithium ions in highly reducing atmosphere, < 0.2 V (*vs.* $Li/Li^+$), not the main insertion and/or conversion reaction with redox reaction of molybdenum ions. Those capacity is known to be the capacity associated with the reversible formation/dissolution of polymeric species at a low voltage as mentioned in *Chapter 2.2.2.4.*.[6, 93, 96, 141] Therefore, broad peaks below 0.8 V (*vs.* $Li/Li^+$) in the de-lithiation dQ/dV plots for three electrodes are observed because there peaks are regardless of the Mo valences and reaction mechanisms of transition metal oxides (Fig. 10d, 10e and 10f).

Table 4 is summarized the first-cycle lithiation / de-lithiation capacity and the initial Coulombic efficiency of three electrodes. As mentioned in Fig. 9, the first-cycle lithiation /de-lithiation capacity delivered by three electrodes is roughly proportional to the Mo valence for three electrodes; +4.4 (aM2-0.8) < +5.5 (aM2-4) < +6.0 (cM3). The

maximum lithiation capacity for the latter two electrodes is determined by the average

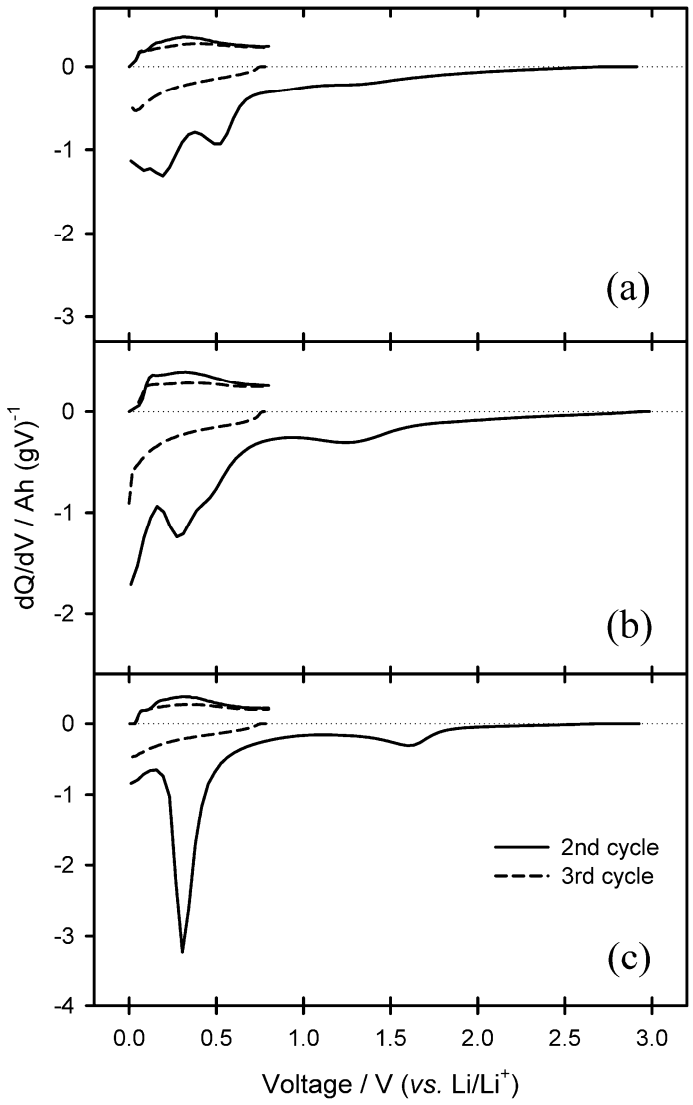


**Figure 11.** The second- and third-cycle differential capacity (dQ/dV) plots for cut-off controlled (a) aM2-0.8, (b) aM2-4, and (c) cM3 electrodes. The cut-off voltages are as follows: 0.01 V (*vs.* Li/Li$^+$) for the first-, second-, and third-cycle lithiation, and 3 V (*vs.* Li/Li$^+$) for the first-cycle de-lithiation, 0.8 V (*vs.* Li/Li$^+$) for the second- and third-cycle de-lithiation.

**Table 4.** Mo valence, the first-cycle lithiation / de-lithiation capacity and the initial Coulombic efficiency of aM2-0.8, aM2-4, and cM3 electrodes.

| The first cycle | Mo valence | Lithiation capacity (mAh $g^{-1}$) | De-lithiation capacity (mAh $g^{-1}$) | Coulombic efficiency (%) |
|---|---|---|---|---|
| aM2-0.8 | + 4.4 | 1019 | 836 | 82.0 |
| aM2-4 | + 5.5 | 1109 | 930 | 83.9 |
| cM3 | + 6 | 1320 | 919 | 69.6 |

Mo valence since they are lithiated by conversion reaction. The maximum lithiation capacity for aM2-0.8 electrode is also decided by the Mo valence even if it is lithiated by insertion reaction. That is, for the insertion-type lithiation, lithium ions and the equivalent amount of electrons should be co-injected into the metal oxides, and thus the sites that can store both lithium ions and electrons are needed. Lithium ions can be stored in structural defects, and any redox centers which should be electrochemically reduced are needed to accommodate the injected electrons. In metal oxide lattice, only the metal ions can serve as the redox center, such that the maximum storage capacity for electrons is determined the metal valence. Therefore, the first-cycle lithiation capacity is roughly proportional to the maximum capacity to be expected from the Mo valence.

As seen in Table. 4, the initial Coulombic efficiency (ICE) of aM2-0.8 and aM2-4 electrodes is much higher than that of cM3 electrode. As mentioned in *Chapter 2.3.2.1.*, due to the severe electrolyte decomposition and poor reversibility of conversion reaction, the ICE of crystal cM3 electrode is extremely low, 69.6 %. In contrast, aM2-0.8 and aM2-4 electrodes show relatively high ICE, > 80 %, because the lithium ions are stored in defects sites in them. In fact, although aM2-4 electrode revealed to be lithiated by conversion reaction, since there are also lots of defects sites as in aM2-0.8 and the bond breakage pattern of conversion reaction in amorphous oxide must be different obviously with that in crystal oxide, it shows similar ICE value with aM2-0.8.

The cycle performances of amorphous molybdenum oxides, however, are different according to reaction mechanism. Fig. 12 indicates the cycle performance of the three electrodes obtained at a current density of 100 mA $g^{-1}$ over the voltage range of 0.01 ~ 3.0 V (*vs.* $Li/Li^+$). A cycle performance of three electrode are significantly different, which is resulted from the difference in reaction mechanisms. The crystal cM3 and aM2-4 lost their capacity in a few tens of cycles because, as it is known widely, the conversion reaction oxide show poor cycle performance due to the repetitive bond breaking and reforming reaction. Otherwise, aM2-0.8 shows good cycle performance until 80 cycles, which is mainly due to the fact that it react with lithium ion through the insertion reaction rather than conversion reaction, as reported previously.[9] Therefore, the Mo valence of amorphous molybdenum oxide can determine the reaction mechanism and thus the electrochemical performance including cycle performance.

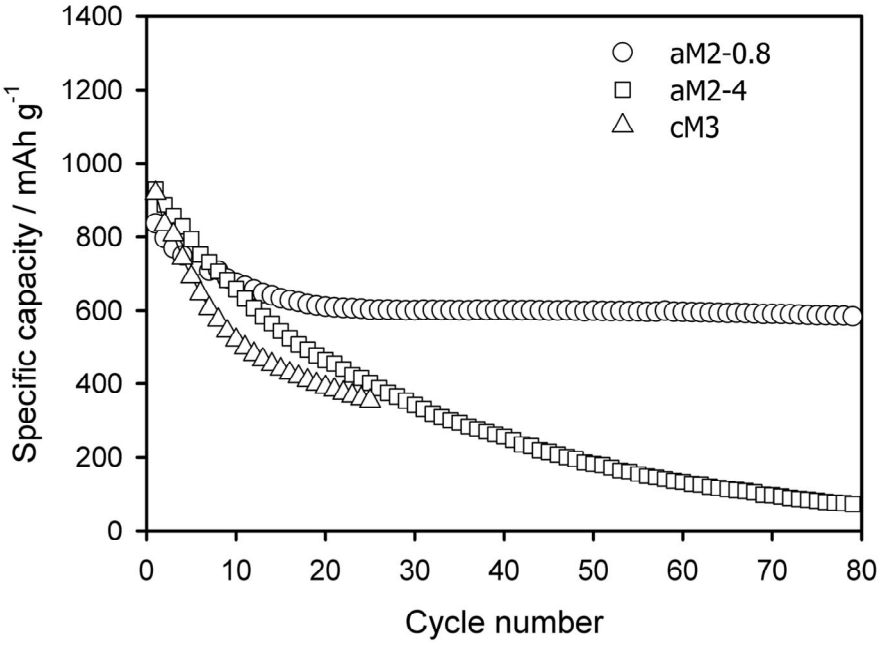


**Figure 12.** Cycle performance of aM2-0.8, aM2-4 and cM3 electrodes with current density of 100 mA $g^{-1}$ over voltage range of 0.01 ~ 3.0 V (*vs.* $Li/Li^{+}$). Only the de-lithiation capacity is shown.

# 4. RESULTS AND DISCUSSION

## 4.2. Enhancement of an initial Coulombic efficiency of molybdenum trioxide negative electrode by ball-milling

High capacity negative electrode has been spotlighted due to the demand for the high-capacity LIB in electric vehicles and energy storage systems. As mentioned in *Chapter 2.2.2.4.*, the transition metal oxides which are lithiated by conversion reaction exhibit high specific capacity (3 ~ 4 times higher than graphite negative electrode).[86, 142-143] The specific capacity of conversion reaction-type transition metal oxides is determined by the valence of transition metal ion since such oxides react as in reaction (4) in *Chapter 2.2.2.4.*, redox reaction between metal ion and elemental metal.

Molybdenum trioxide ($MoO_3$) is one of the most promising conversion reaction-type negative electrode materials since it shows a considerably high specific capacity (theoretical specific capacity of $MoO_3$: 1117 mAh $g^{-1}$), followed by the reaction:[127]

$$MoO_3 + 6Li^+ + 6e^- \rightarrow Mo + 3Li_2O \quad (6)$$

It is reacted with six $Li^+$/electrons per formula unit or per one transition metal ion due to the Mo valence is +6. Among conversion reaction-type transition oxides, there are few or no oxides having valence of +6, and therefore, $MoO_3$ exhibits higher specific capacity than other transition metal oxides.

However, it also has several drawbacks including poor cycleability, low Coulombic efficiency: these issues are not only in $MoO_3$, but in almost every conversion reaction-type transition metal oxides. Above all, the low initial Coulombic efficiency (ICE) is a critical issue, as mentioned in *Chapter 2.3.2.1.*. In particularly, ICE is extremely low in $MoO_3$ electrode, around 60 %. Rather than other oxides, the de-lithiation process of $MoO_3$, the reverse of reaction (6) involved six electrons transfer reaction per one transition metal. Since many electron involved reaction is generally difficult and should occur through many steps, it is hard to oxidize Mo (valence: 0) up to $MoO_3$ (valence: 6). The first part of this study is the analysis of the reaction mechanism of $MoO_3$ electrode, especially de-lithiation process. It is followed by the enhancement of ICE of $MoO_3$ electrode by enlarging the de-lithiation capacity, especially de-conversion reaction capacity, through the ball-milling. Ball-milled $MoO_3$ shows the improved reversibility of conversion reaction, and therefore, the

enhancement of ICE up to around 75 %.

First of all, the reaction mechanism of the first-cycle in $MoO_3$ electrode with lithium is examined. The $MoO_3$ (99.5 +%; Sigma-Aldrich) electrode was used. X-ray diffraction (XRD) and X-ray absorption near edge structure (XANES) were used to investigate the structure and valence change during the first-cycle lithiation and de-lithiation. As seen in Fig. 13, $MoO_3$ electrode is lithiated by three reactions, already mentioned in *Chapter 2.2.2.4.*: (i) insertion reaction near 2.5 V (*vs.* $Li/Li^+$), (ii) conversion reaction near 0.5 V (*vs.* $Li/Li^+$), (iii) additional surface-related reaction below 0.2 V (*vs.* $Li/Li^+$), and such behaviors show much more clearly in dQ/dV plot (Fig. 13b).

Through *ex-situ* XRD patterns, the structural analysis during the first-cycle lithiation is conducted (Fig. 14). Note that XRD pattern of $MoO_3$ electrode before cycling (designated OCV in Fig 14) shows much stronger *(0k0)* plane peaks than that in reference (JCPDS # 05-0508), which causes the preferred orientation of platy-type $MoO_3$ powder in the electrode. This powder tends to lie during electrode fabrication (hand-mixing by a mortar and coating by blade), resulting much higher preferred orientation than powder itself. After insertion reaction up to 2 V (*vs.* $Li/Li^+$), *(0k0)* plane peaks move to the lower angles due to the expansion of $MoO_3$ layers derived by lithium ion insertion.[144] The electrode gives a featureless XRD pattern after conversion reaction starts (400 mAh $g^{-1}$), and it remains until 0 V (*vs.* $Li/Li^+$). It is a characteristic of conversion reaction, also mentioned *Chapter 2.2.2.4.*: the collapse of

highly crystalline $MoO_3$ structure into an amorphous and/or nano-crystalline phase after lithiation.[145]

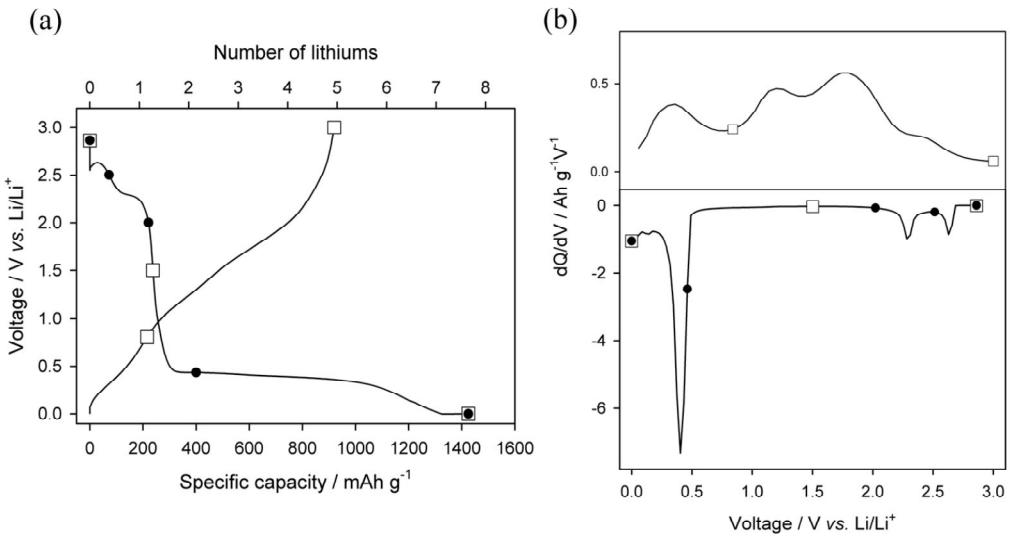


**Figure 13.** (a) The first-cycle voltage – capacity profile and (b) dQ/dV plot of $MoO_3$ (99.5 +%; Sigma-Aldrich) electrode. Black spots and white squares are the points for *ex-situ* XRD, and *ex-situ* XANES, respectively.

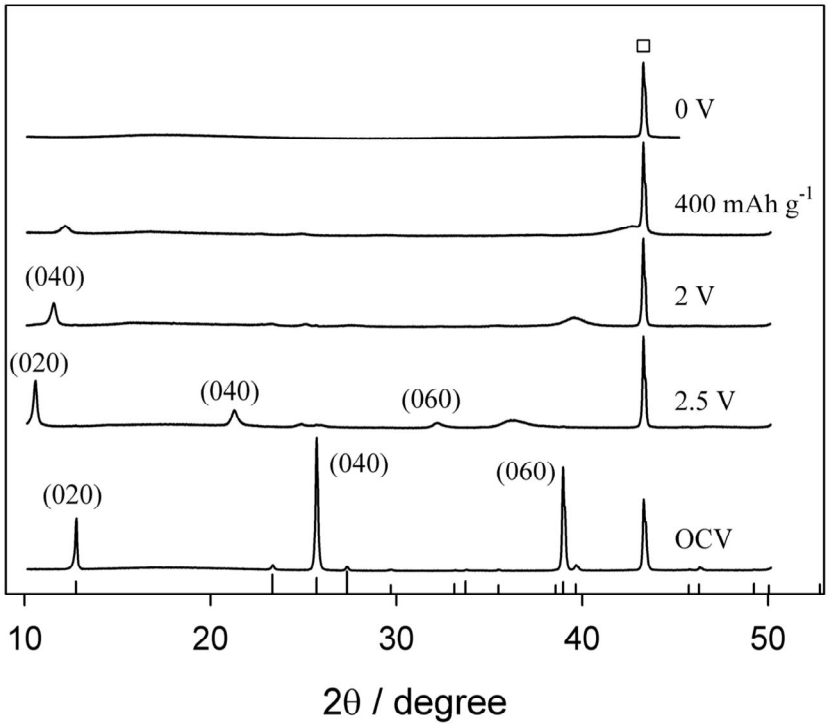


**Figure 14.** *Ex-situ* XRD patterns of $MoO_3$ (Sigma-Aldrich) electrode before cycling (OCV), after lithiation until 2.5 V, 2 V, 400 mAh $g^{-1}$, and 0 V (*vs.* $Li/Li^+$). White square is peak from Cu current collector. Reference $MoO_3$ (JCPDS # 05-0508) is indicated as the gray drop line.

The Mo valence change during lithiation and de-lithiation of $MoO_3$ electrode is examined by *ex-situ* XANES spectra (Fig. 15). Note that, before cycling of $MoO_3$ electrode, indicated OCV in Fig. 15a, the pre-edge is observed in the front of main edge. This pre-edge is originated from 1s to 4d transition, which is a forbidden in principle. However, it is known that if molybdenum ions are located in the tetrahedral sites or distorted octahedral sites, this forbidden transition can occur.[146] Since the sites of molybdenum ions in $MoO_3$ are distorted octahedral sites, the pre-edge appears and therefore, it can be the specific feature of $MoO_3$, or $Mo^{6+}$, whereas no pre-edge in $MoO_2$, or $Mo^{4+}$ located in ordinary octahedral site.[147] As seen in Fig. 15a, after lithiation until 2 V (*vs.* $Li/Li^+$), pre-edge disappear and the main absorption edge moves to the low energy level (eV) because $Mo^{6+}$ in $MoO_3$ is reduced to $Mo^{4+}$ by taking about 2 $Li^+$/electrons per formula unit by following as in.[127]

$$MoO_3 + xLi^+ + xe^- \rightarrow Li_xMoO_3 \ (x \sim 2)$$

Further lithiation up to 0 V (*vs.* $Li/Li^+$) results in the shift of main edge to that of Mo metal reference. Such change of Mo valence can be an evidence for conversion reaction of $MoO_3$ electrode resulting nano-grains of molybdenum metal dispersed $Li_2O$ matrix.

$$Li_xMoO_3 + (6-x)Li^+ + (6-x)e^- \rightarrow Mo^0 + 3Li_2O$$

During de-lithiation of $MoO_3$ electrode, *ex-situ* XANES spectra were obtained at the two points, 0.8 V and 3 V (*vs.* $Li/Li^+$) (Fig. 15b). At the 0.8 V (*vs.* $Li/Li^+$), it is

interesting that the main edge still remains its position at that of Mo metal reference even though the capacity amount of 200 mAh $g^{-1}$ are de-lithiated in 0 ~ 0.8 V (*vs.* $Li/Li^+$). Hence, it can be proven that such capacity is stemmed from the dissolution of polymer/gel-like film, called as an *additional de-lithiation capacity*, already demonstrated by Tarascon group in 2002.[93] Such dissolution reaction does not related to the reaction (6), and therefore, the Mo valence is still the metallic state even oxidation until 0.8 V (*vs.* $Li/Li^+$). After de-lithiation up to the 3 V (*vs.* $Li/Li^+$), pre-edge appear again, but this intensity is smaller and the position of main edge is lower energy than those in OCV, which means that this electrode cannot be fully-oxidized up to $Mo^{6+}$ (average Mo valence after the first-cycle de-lithiation < +6) because the reverse of reaction (6) is not completely reversible, as mentioned in *Chapter 2.2.2.4.*. De-conversion reaction of $MoO_3$ electrode follows as in.

$$Mo^0 + 3Li_2O \rightarrow MoO_y + 2yLi^+ + 2ye^-$$

Due to these phenomena, the $MoO_3$ electrode shows the extremely low initial Coulombic efficiency (ICE), around 65%.

Fig. 16 indicates the reaction mechanism of the first-cycle in $MoO_3$ electrode confirmed by XRD and XANES data. Among the first-cycle de-lithiation reaction of $MoO_3$ electrode, which are an additional de-lithiation reaction and de-conversion reaction, the poor reactivity of latter is a main reason for low ICE. Therefore, in order to enhance the ICE of $MoO_3$ electrode, the reactivity of de-conversion reaction should

be increased, and in this study, it is achieved by a simple and short ball-milling of $MoO_3$.

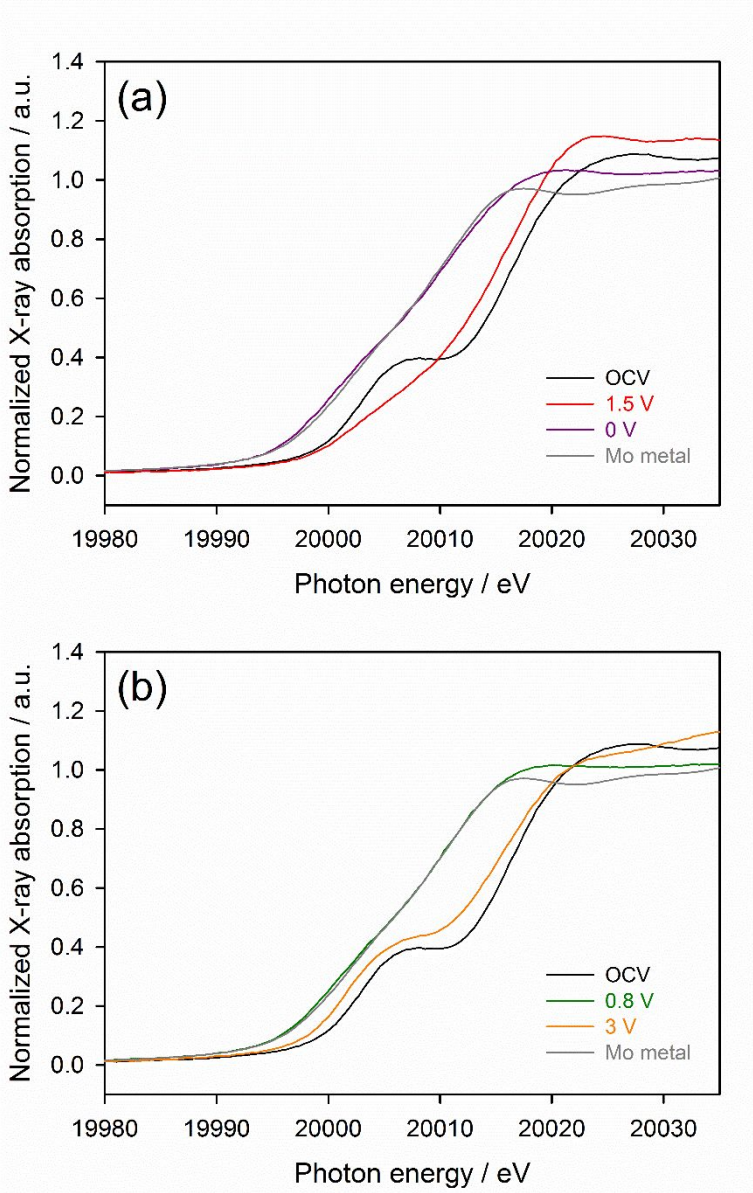




**Figure 15.** *Ex-situ* XANES of $MoO_3$ (Sigma-Aldrich) electrodes (a) before cycling (OCV), after lithiation until 1.5 V, 0 V (*vs.* $Li/Li^+$), and (b) before cycling (OCV), after de-lithiation up to 0.8 V, 3 V (*vs.* $Li/Li^+$). XANES spectrum for Mo metal is also indicated as the reference (gray line).

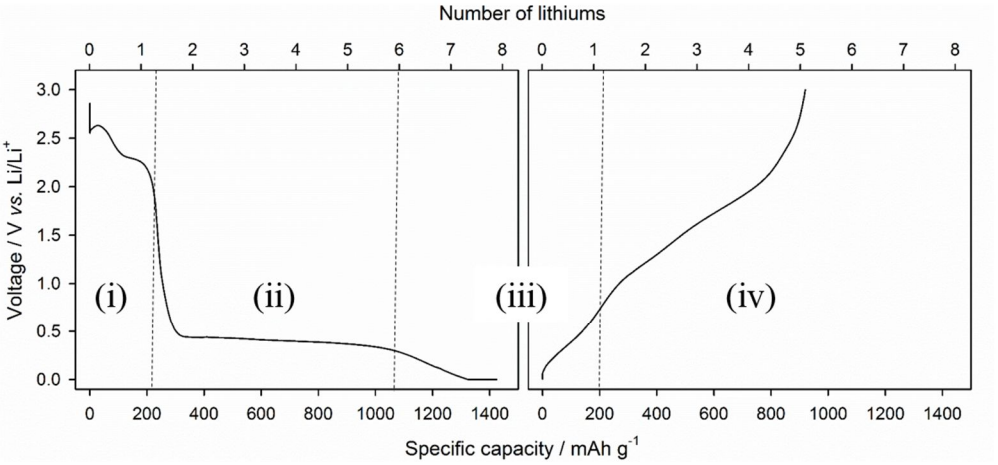


(i) Insertion reaction:
$MoO_3 + xLi^+ + xe^- \rightarrow Li_xMoO_3$

(ii) Conversion reaction:
$Li_xMoO_3 + yLi^+ + ye^- \rightarrow Mo^0 + 3Li_2O$

(iii) Additional lithiation / de-lithiation capacity (polymer/gel-like film formation / dissolution)

(iv) De-conversion reaction:
$Mo^0 + 3Li_2O \rightarrow MoO_z + 2zLi^+ + 2ze^-$

**Figure 16.** The summarized the first-cycle reaction mechanism following $MoO_3$ (Sigma-Aldrich) electrode investigated by *ex-situ* XRD and XANES.

Active material was prepared by solid-state reaction of ammonium heptamolybdate tetrahydrate (AHM), and ball-milling was conducted with low speed (300 rpm) to minimize the reduction of $MoO_3$, as mentioned in *Experimental (Chapter 3.1.2.)*. Heating temperature during solid-state reaction was chosen, based on TGA data (Fig. 17). AHM is thermally decomposed by following as in (stoichiometry is ignored).[148]

$$(NH_4)_6Mo_7O_{24} \cdot 4H_2O \rightarrow (NH_4)_4Mo_5O_{17} \rightarrow (NH_4)_2Mo_4O_{13} \rightarrow MoO_3$$

As seen in Fig. 17, since thermal decomposition of AHM is finished in below 400 $^oC$, a heating above 400 $^oC$ can give $MoO_3$ powder.

FE-SEM image shows the well-synthesized micro-sized $MoO_3$ powder (indicated as bare in Fig. 18a). Synthesized $MoO_3$ powder (bare, hereafter) has platy shape and smooth surface. Even 5 min ball-milling, the particles are crushed, and tens of nanometric particles begin to form. Further ball-milling results that micro-sized particles is very little or none. BET surface of ball-milled powders are increasing with ball-milling time, but seem to be saturated (Fig. 18b).

As represented in Fig. 19a, the XRD patterns of ball-milled $MoO_3$ still show the crystalline nature. Note that, as mentioned in Fig. 14, strong peaks corresponding to *(0k0)* planes in bare indicate the anisotropy of platy shape $MoO_3$ powder (bare in Fig. 18a). On the contrary, the peak ratio of ball-milled $MoO_3$ powder are well-matched with that of reference, which means the breakage of particles removes the

anisotropy.[127] In addition, the diffraction peaks are broadened indicating the reduction of crystalline size

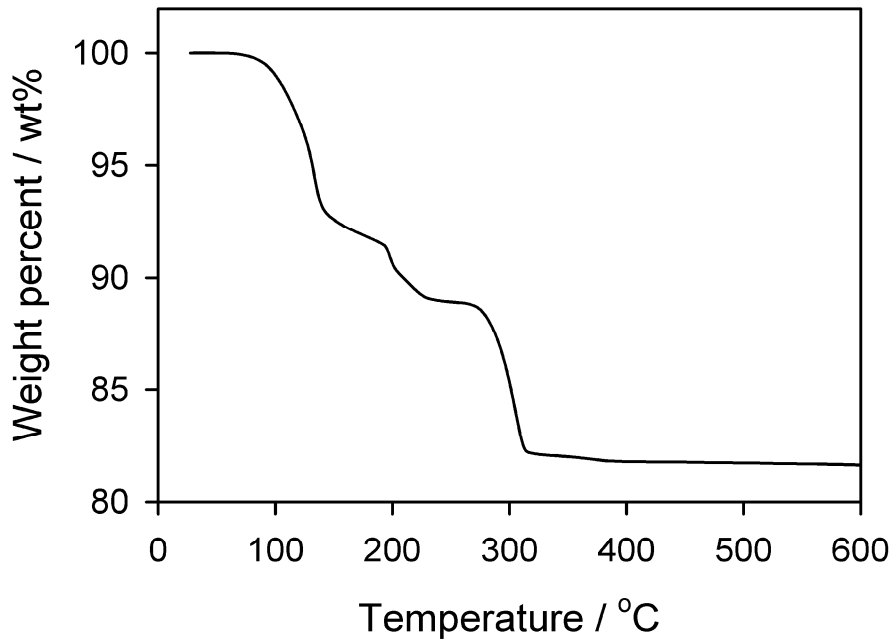


**Figure 17.** TGA data of ammonium heptamolybdate tetrahydrate, $(NH_4)_6Mo_7O_{24}•4H_2O$.

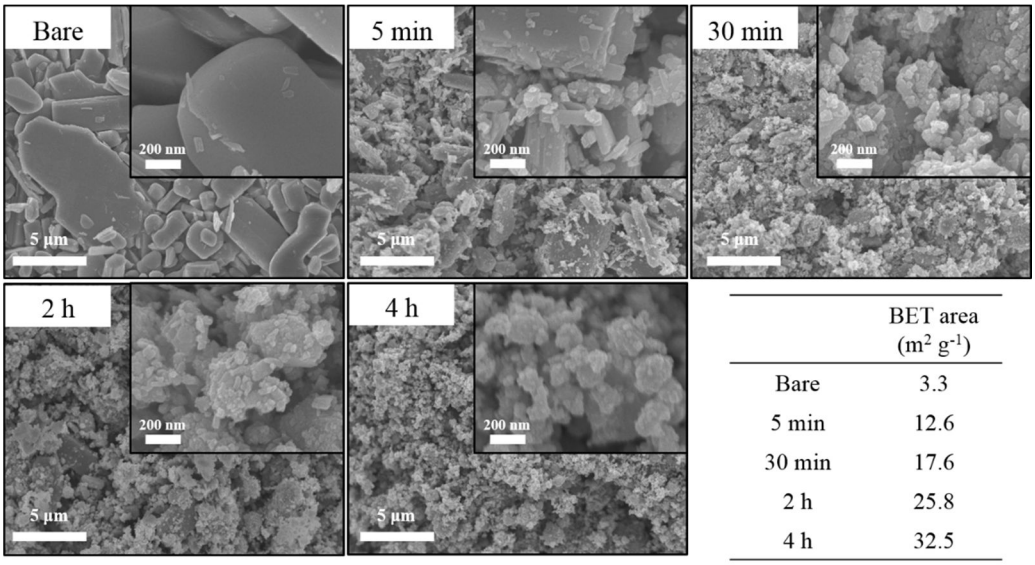


| | BET area ($m^2$ $g^{-1}$) |
|---|---|
| Bare | 3.3 |
| 5 min | 12.6 |
| 30 min | 17.6 |
| 2 h | 25.8 |
| 4 h | 32.5 |

**Figure 18.** FE-SEM images and BET surface areas of bare and ball-milled (during 5 min, 30 min, 2 h, and 4 h) $MoO_3$ powders.

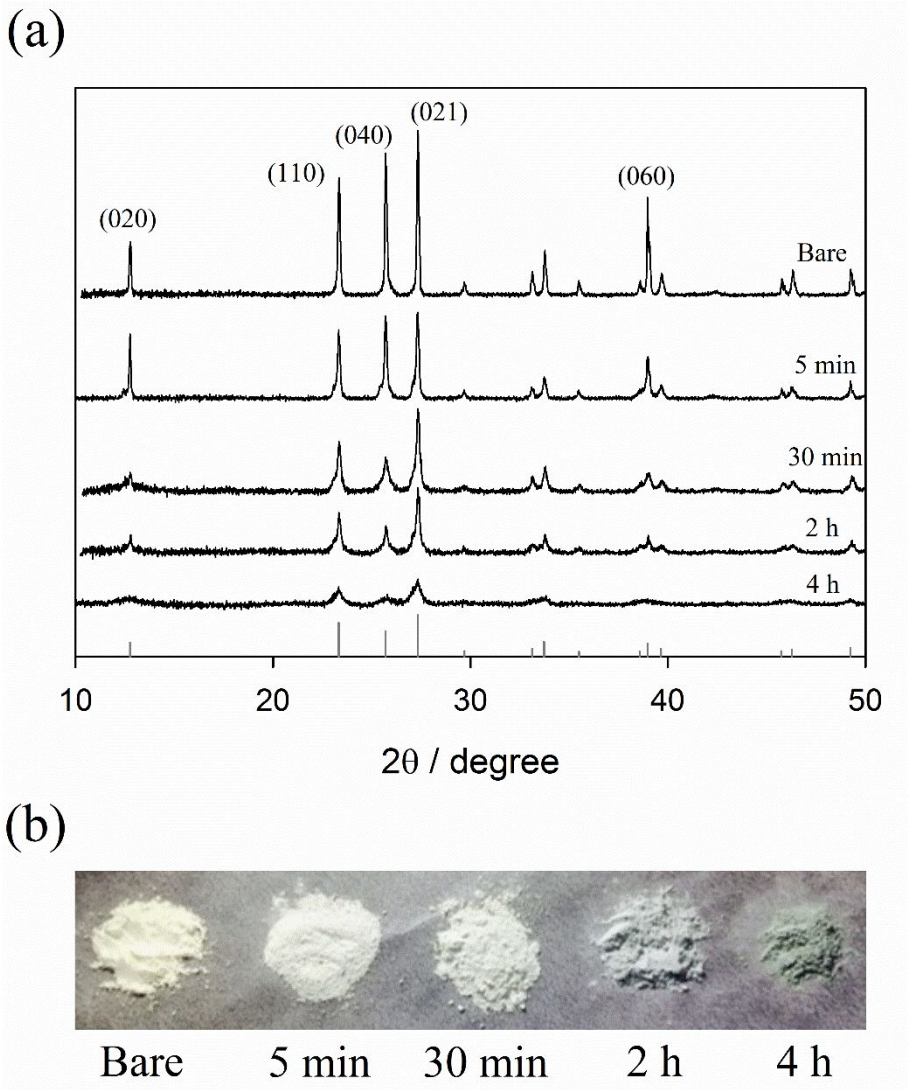


**Figure 19.** (a) XRD patterns and (b) powder colors of bare and ball-milled (during 5 min, 30 min, 2 h, and 4 h) $MoO_3$ powders. Reference $MoO_3$ (JCPDS # 05-0508) is indicated as the gray drop line in (a).

and/or crystallinity. Owing to low ball-milling speed (low energy), the bulk phase of $MoO_3$ does not change to reduced form such as $Mo_4O_{11}$ (+5.5). However, the colors of ball-milled $MoO_3$ gradually becomes dark (Fig. 19b). It is likely due to the partial reduction of surface of $MoO_3$ after 2 h ball-milling, even though low ball-milling energy. It is known that the color of $MoO_{3-x}$ is a light green, and therefore, powder after 2 h ball-milling seem to be partially reduced, but still not changed bulk phase.

Fig. 20 shows the first-cycle voltage – capacity profiles bare and 5 min, 30 min ball-milled $MoO_3$ electrodes (designated as 5 min and 30 min electrode, respectively, hereafter), and the first-cycle lithiation / de-lithiation capacity and Coulombic efficiency are indicated in Table 5. Other samples are discussed in a later section. Even enlarged BET surface area with ball-milling, the first-cycle lithiation capacity of three electrodes are similar (1465, 1454, and 1503 mAh $g^{-1}$ for bare and 5 min, 30 min electrodes, respectively) which means the first-cycle irreversible charge consumption at the surface of $MoO_3$ electrode is independent with BET surface area. In fact, since the irreversible electrolyte decomposition occurs at the surface of electrode, the amount of such reaction should be proportional to the surface area of active material, but not in ball-milled $MoO_3$ electrode. The reason is likely due to the large volume expansion of conversion reaction of $MoO_3$ electrode, around 175 % calculated by the basis of reaction (6). Due to such a large volume expansion, additional electrolyte decomposition occurs at the newly exposed surface (Fig. 21), and therefore there is no

relationship between the BET surface area before cycling and irreversible charge consumption in the lithiation. On the other

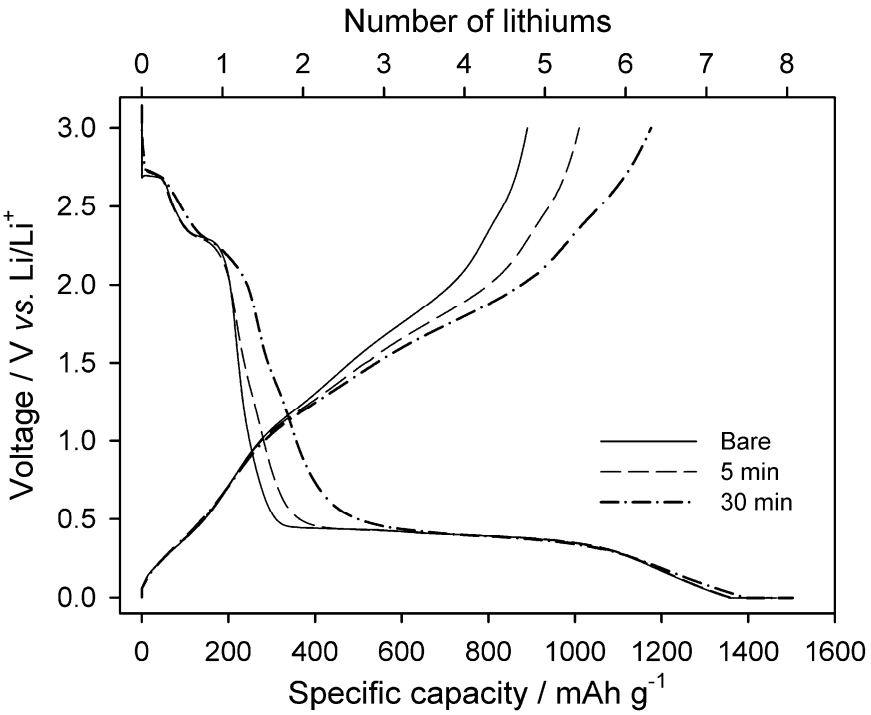


**Figure 20.** The first-cycle voltage – capacity profiles of bare, 5 min, and 30 min ball-milled $MoO_3$ electrodes.

**Table 5.** The first-cycle lithiation / de-lithiation capacity and the initial Coulombic efficiency of bare, 5 min, and 30 min ball-milled $MoO_3$ electrodes.

| The first cycle | Lithiation capacity (mAh $g^{-1}$) | De-lithiation capacity (mAh $g^{-1}$) | Coulombic efficiency (%) |
|---|---|---|---|
| Bare | 1465 | 890 | 60.8 |
| 5 min | 1454 | 1010 | 69.5 |
| 30 min | 1503 | 1176 | 78.2 |

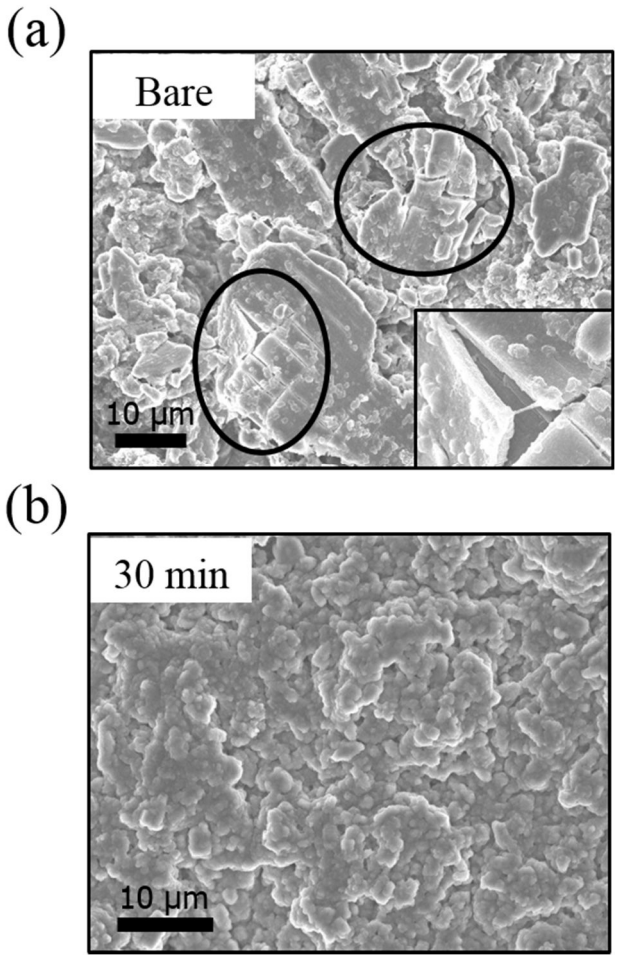


**Figure 21.** FE-SEM images of (a) bare and (b) 30 min ball-milled $MoO_3$ electrodes after the first-cycle de-lithiation. Note that cracks in (a) due to volume expansion, whereas not in (b).

hands, the first-cycle de-lithiation capacity of these electrodes are getting enlarging with ball-milling time (890, 1010, 1176 mAh $g^{-1}$ for bare and 5 min, 30 min electrodes, respectively), which results in enhanced ICE up to around 78 % in 30 min electrode. Note that the first-cycle de-lithiation capacity of 30 min electrode exceeds theoretical capacity of MoO3 (1117 mAh g-1). It is feasible that there are additional de-lithiation capacity, mentioned in Fig. 16.

A closer look at the de-lithiation dQ/dV plots in Fig. 21 reveals two noticeable issues. Among two kinds of de-lithiation reaction mentioned in Fig. 16, the de-conversion reaction capacity of ball-milled $MoO_3$ electrodes, above 0.8 V (*vs.* $Li/Li^+$), are enlarged, whereas similar an additional de-lithiation capacity, below 0.8 V (*vs.* $Li/Li^+$). It means that the reactivity of de-conversion reaction, or the reversibility of conversion reaction, of $MoO_3$ electrode is enhanced by just short-time ball-milling.

This result is further confirmed by *ex-situ* XANES after the first cycle (Fig. 22). As mentioned in Fig. 15, after the first cycle of $MoO_3$ electrode, the pre-edge is recovered and main edge is shifted to similar position with that in before cycling. The main edge of 30 min electrode after the first cycle is located higher eV than that of bare electrode (Fig. 22a). In addition, Mo-$O_I$ bonding in 30 min electrode is more recovered than that in bare electrode (Fig. 22b).[149] It is indicating that higher Mo valence in 30 min electrode than that in bare electrode. In other words, during de-lithiation, larger amount of lithium ions and electrons are extracted in 30 min electrode. Note that

intense peak at around 2.5 Å is observed in both electrodes, which corresponds to Mo – Mo bond

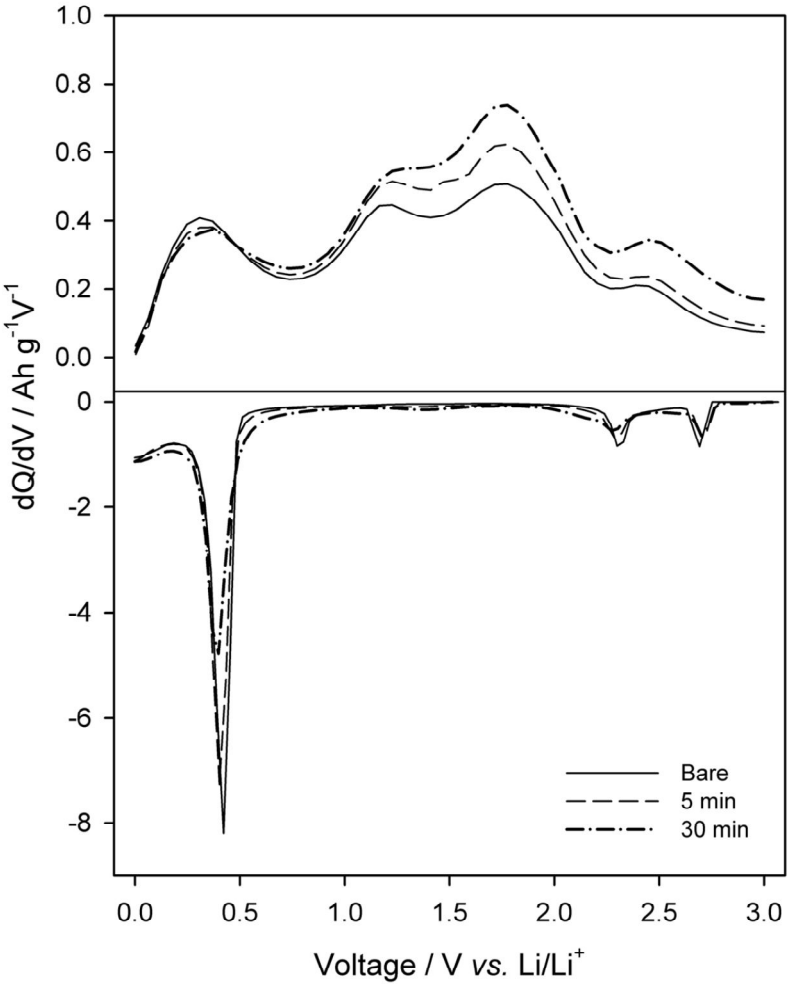


**Figure 22.** The lithiation and de-lithiation dQ/dV plots for first cycle of bare, 5 min and 30 min ball-milled $MoO_3$ electrodes.

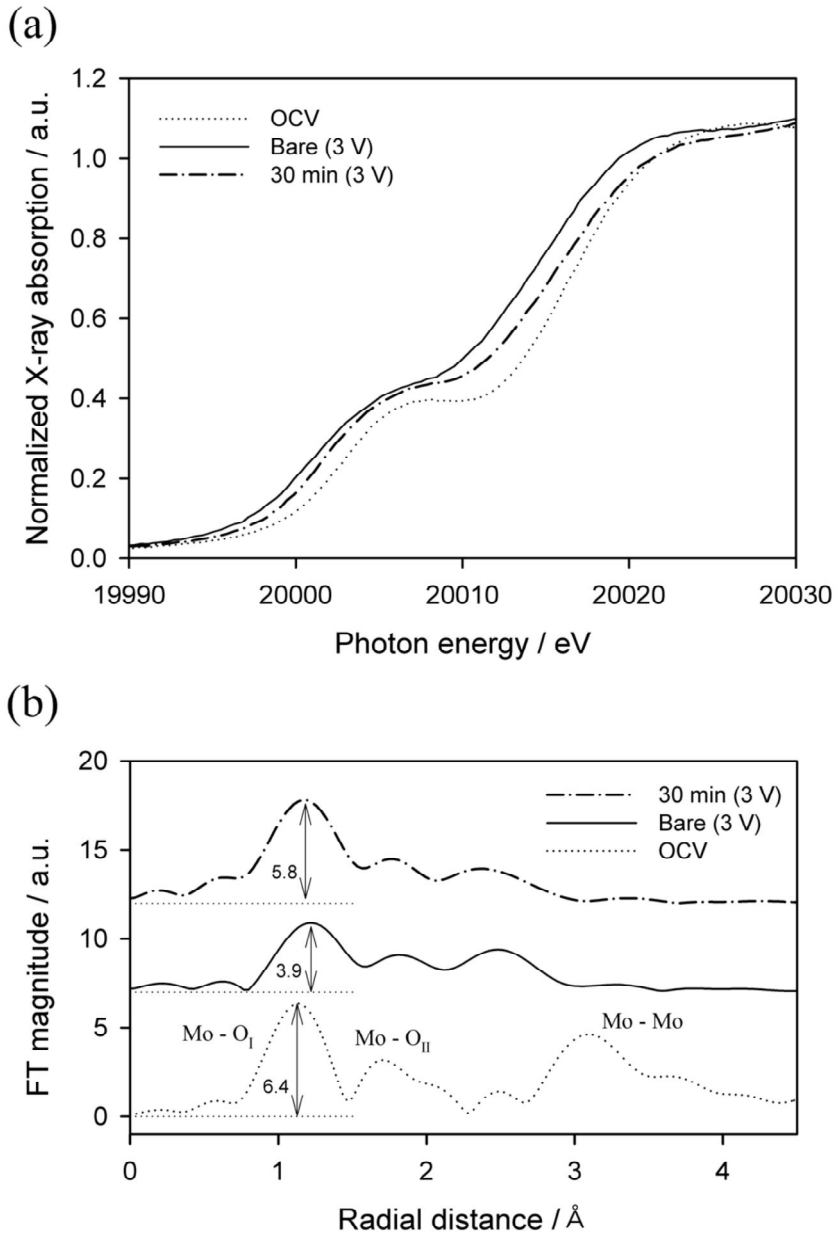


**Figure 23.** (a) *Ex-situ* XANES spectra and (b) EXAFS spectra for bare and 30 min ball-milled $MoO_3$ electrodes after the first-cycle de-lithiation. Numbers in (b) are FT magnitudes for Mo – $O_I$ bond. Spectra for bare electrode before cycling is also depicted as dotted line (indicated as OCV).

between edge shared $MoO_6$ octahedral in $MoO_{3-x}$.[149] In $MoO_3$ structure, there are no edge shared $MoO_6$ octahedral, and therefore, it means that both electrode cannot be fully-oxidized until $MoO_3$ phase.

Higher Mo valence in 30 min electrode than bare electrode is also verified by the comparison of initial voltage in the second cycle. Fig 23 indicates the first points in second-cycle voltage – capacity profiles. This value is very similar with the quasi-open circuit voltage (QOCV) after finishing the first cycle, and QOCV can represent the relative amount of electrons in electrode. The higher initial voltage in ball-milled electrode, 2.61 and 2.85 V (*vs.* $Li/Li^+$) for 5 min and 30 min electrodes, respectively, than bare electrode, 2.48 V (*vs.* $Li/Li^+$), is due to the higher oxidation state of molybdenum ion at the end of the first cycle. Such sequence of QOCV value (bare < 5 min < 30 min) is the same in that of the first-cycle de-lithiation capacity. In addition, in second cycle, reaction between $Mo^{6+}$ and $Mo^{4+}$ around 1.5 V (*vs.* $Li/Li^+$) is much dominant in ball-milled electrode, indicating again that there are larger amount of $Mo^{6+}$ ion in ball-milled electrode than bare electrode after finishing the first cycle. Therefore, these behaviors are also the evidence for highly reversible conversion reaction in ball-milled electrode. Among ball-milled electrodes, 30 min electrode shows higher specific capacity and higher ICE than 5 min electrode, which means the ball-milling affects positively, at least up to 30 min.

Galvanostatic intermittent titration technique (GITT) experimental was conducted to evaluate the difference in resistance, or kinetic issue between bare and 30 min

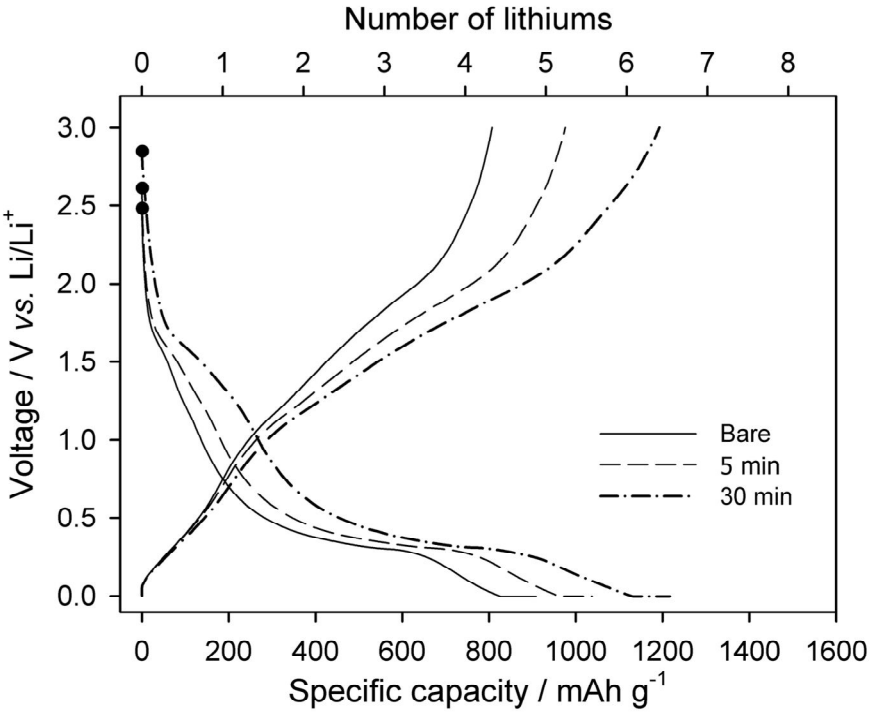


**Figure 24.** The second-cycle voltage – capacity profiles of bare and 5 min, 30 min ball-milled $MoO_3$ electrodes. Dots are indicated the initial voltages for second cycle.

electrodes. Through the GITT, the total resistance in the cell can be obtained (*Chapter 3.2.5.*). In this study, components in two cells are the same except the working electrode (bare and 30 min electrodes), and therefore, the resistance difference between bare and 30 min electrodes can be clearly obtained (Fig. 24). As seen in Fig. 25, there are two different regions in resistance: just before conversion reaction, between 2.5 ~ 0.5 V (*vs.* $Li/Li^+$) during lithiation, and above 1.5 V (*vs.* $Li/Li^+$) during de-lithiation. The former difference may be due to the decrease in resistance for Mo – O bond breakage by ball-milling. However, it is not true. Instead, it is more proper interpretation that, in bare electrode, there are no empty space to insert lithium ion in this voltage region, whereas 30 min electrode has something which can accept lithium ions in this voltage region. Meanwhile, the de-conversion reaction capacity of two electrodes may be different owing to the latter resistance difference.

The firstly expected reason for resistance difference and the enhancement of ICE of ball-milled electrode is the effect of decrease in size, because the tens of micrometric $MoO_3$ powders are easily crushed to be generated small piece of particles even 5 min ball-milling (FE-SEM images in Fig. 18). In order to demonstrate the size effect of $MoO_3$ powder, hundreds of nanometric particles was synthesized by heating precursor at 500 $^oC$ rather than 600 $^oC$, and also ball-milled during 30 min. Fig. 26 shows FE-SEM images of $MoO_3$ powders prepared at 500 $^oC$ and after 30 min ball-milling, compared with 600 $^oC$ samples (already shown in Fig. 18). Note that the size

of bare $MoO_3$ powders are considerably reduced by decrease of heating temperature. Unfortunately however,

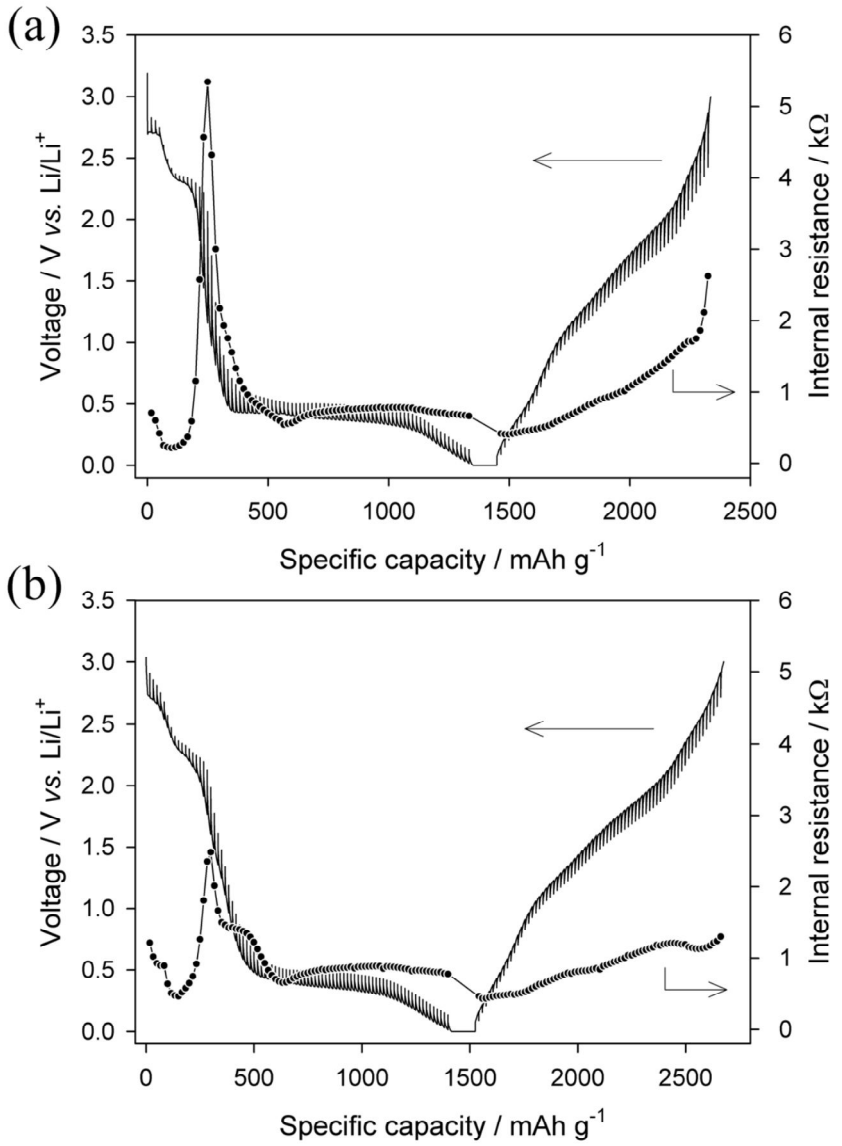


**Figure 25.** The voltage – capacity profiles in GITT and calculated internal resistance of (a) bare, (b) 30 min ball-milled $MoO_3$ electrodes.

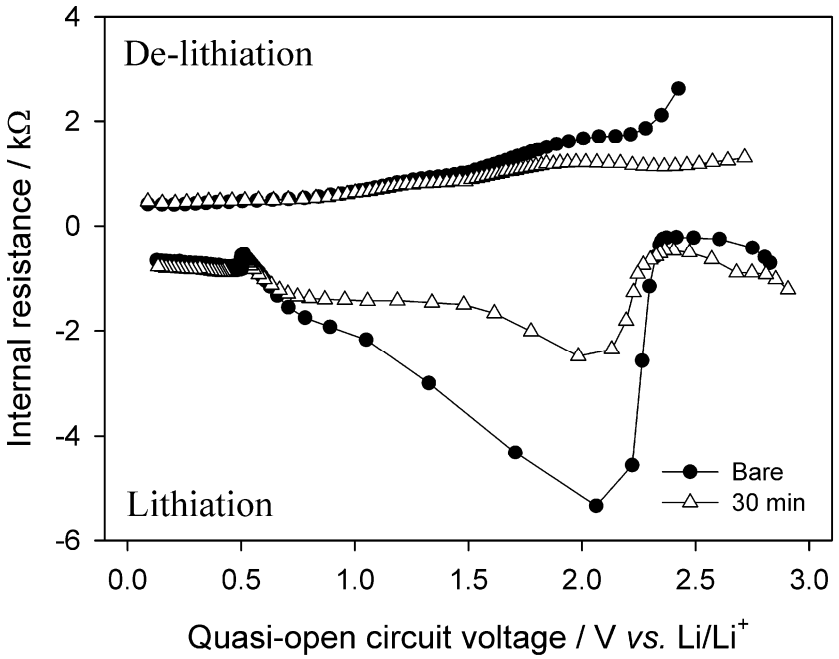


**Figure 26.** QOCV value *vs.* internal resistance plot from GITT (Fig. 24) for bare and 30 min ball-milled $MoO_3$ electrodes. Internal resistance in lithiation and de-lithiation are depicted as the negative and positive values, respectively.

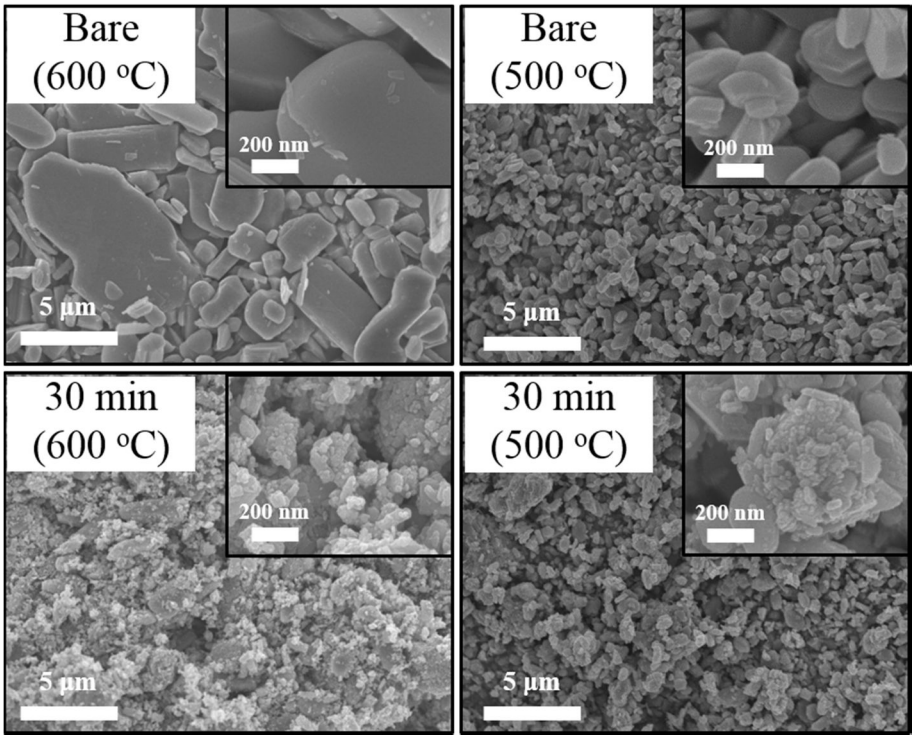


**Figure 27.** FE-SEM images of bare and 30 min ball-milled $MoO_3$ powders synthesized at 600 °C and 500 °C, respectively.

as seen in Fig. 27, its electrochemical performance, especially the first-cycle de-lithiation capacity, is still similar with 600 $^{o}$C bare electrode. On the other hands, 500 $^{o}$C – 30 min ball-milled electrode shows enlarged de-lithiation capacity, similar with 600 $^{o}$C – 30 min ball-milled electrode. In particular, likewise in previous electrodes, it is also exhibited the enlarged de-conversion reaction capacity in above 0.8 V (*vs.* $Li/Li^{+}$) (Fig. 27b). Therefore, it is deduced that such enhanced the reversibility of conversion reaction stems from the ball-milling, not size effect (until hundreds of nanometers at least).

Transmission electron microscopy (TEM) experimental was conducted to examine the ball-mill effect more precisely. As shown in Fig. 28, decrease in heating temperature during preparation of $MoO_3$ results particles having hundreds of nanometric size and clean surface. After 30 min ball-milling, however, images show the grinded surfaces and tens of nanometric particles like dusts. These features cannot be made by heating process, only possible by ball-milling. Regardless of heating temperature, the improved electrochemical performance is observed in 30 min electrodes. The difference between them is revealed as particle size, especially the existence of the grinded surfaces and tens of nanometric particles, not the bulk structure and the oxidation state of them confirmed by XRD and the color of powder. Therefore, such electrochemical performance difference should be originated from such grinded surface and/or tens of nanometric particles formed by ball-milling.

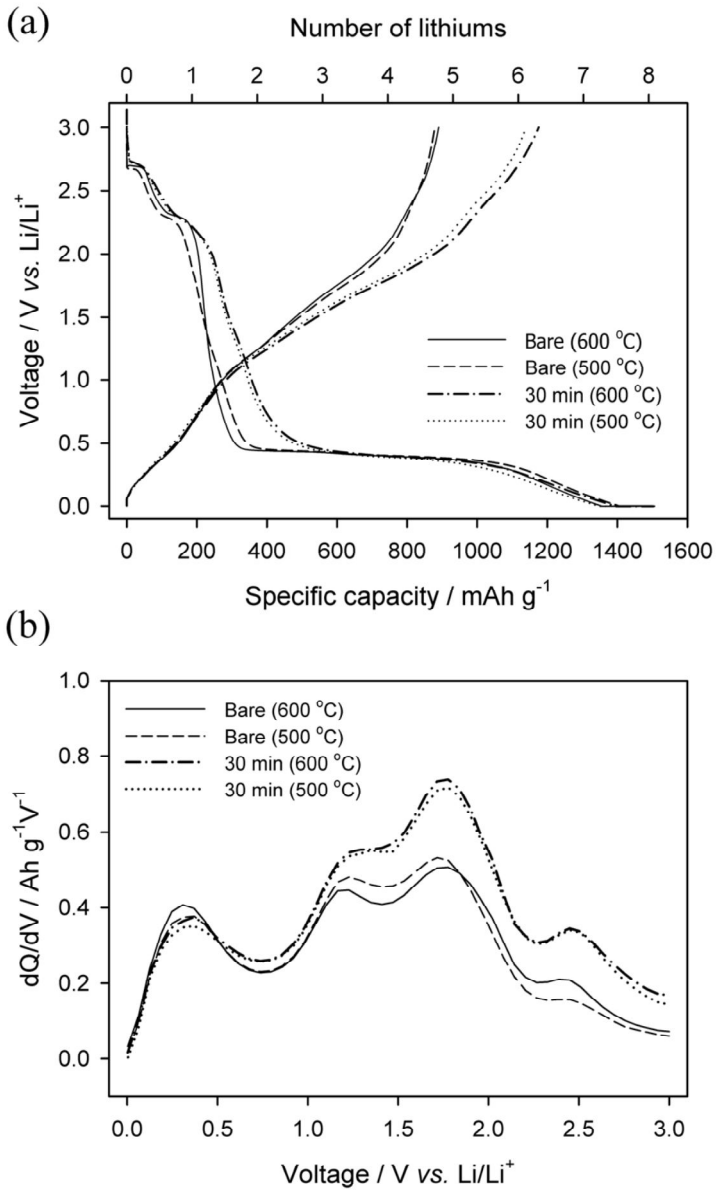


**Figure 28.** (a) The first-cycle voltage – capacity profiles and (b) de-lithiation dQ/dV plots of electrodes for bare and 30 min ball-milled $MoO_3$ synthesized at 600 $^{o}$C and 500 $^{o}$C, respectively.

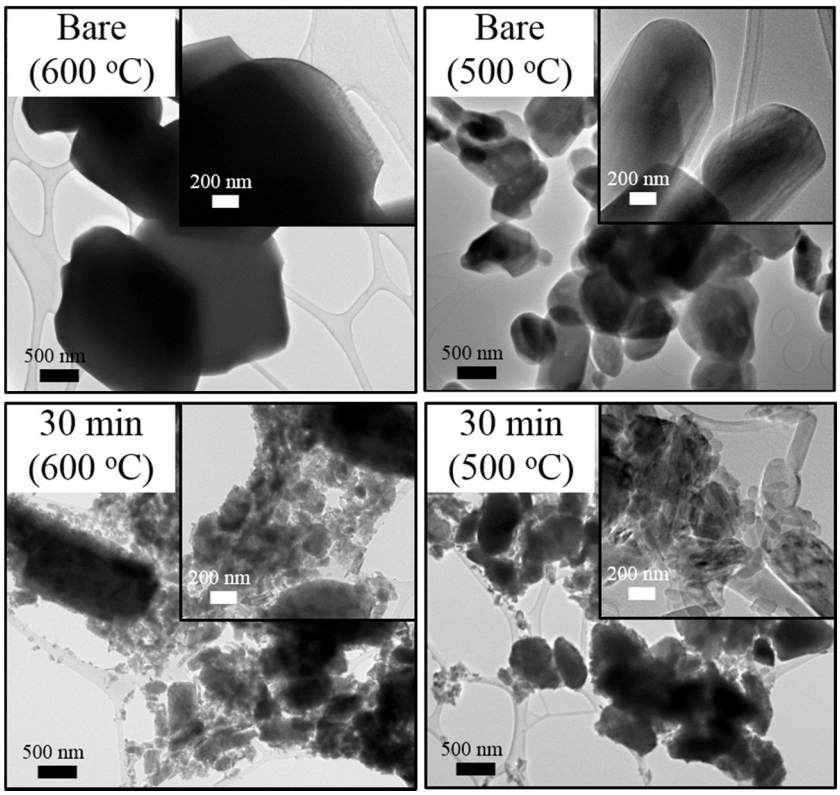


**Figure 29.** TEM images of bare and 30 min ball-milled $MoO_3$ powders synthesized at 600 °C and 500 °C, respectively.

Effects of the grinded surfaces and tens of nanometric particles are evaluated by voltage spectroscopy (EVS) or potentiostatic intermittent titration technique (PITT). As mentioned in *Chapter 3.2.6.*, thermodynamic potential can be obtained during relatively short time by this method. Thermodynamic potential is also represented as the electrochemical potential of lithium ($\mu_{Li}$) (*Chapter 2.1.*). Fig. 29a shows the EVS profiles of bare and 30 min electrodes during lithiation, and capacity at each step (10 mV) in voltage range of 0.5 ~ 2.3 V (*vs.* $Li/Li^+$) are indicated in inset. Reactions above 2.2 V (*vs.* $Li/Li^+$) and below 0.5 V (*vs.* $Li/Li^+$) are insertion and conversion reactions, respectively. Between them, there are no reactions thermodynamically, and thus, bare electrode exhibits almost no capacity in this voltage range. The 30 min electrode, however, shows somewhat capacity, around 200 mAh $g^{-1}$ higher than bare electrode, calculated from the area between bare and 30 min plots in inset. Since, in this voltage range, bulk $MoO_3$ cannot react with lithium ion, such capacity must come from the new lithium storage sites formed by ball-milling. Therefore, from HR-TEM images and EVS data, it is inferred that the grinded surfaces and tens of nanometric particles mentioned in Fig. 28 have various chemical potentials and react with lithium in voltage range of 0.5 ~ 2.2 V (*vs.* $Li/Li^+$).

Since they are created by ball-milling, the nature of these particles should be amorphous. As mentioned in the front of this chapter, conversion reaction after finishing insertion reaction follows as in.

$$Li_xMoO_3 + (6-x)Li^+ + (6-x)e^- \rightarrow Mo^0 + 3Li_2O$$

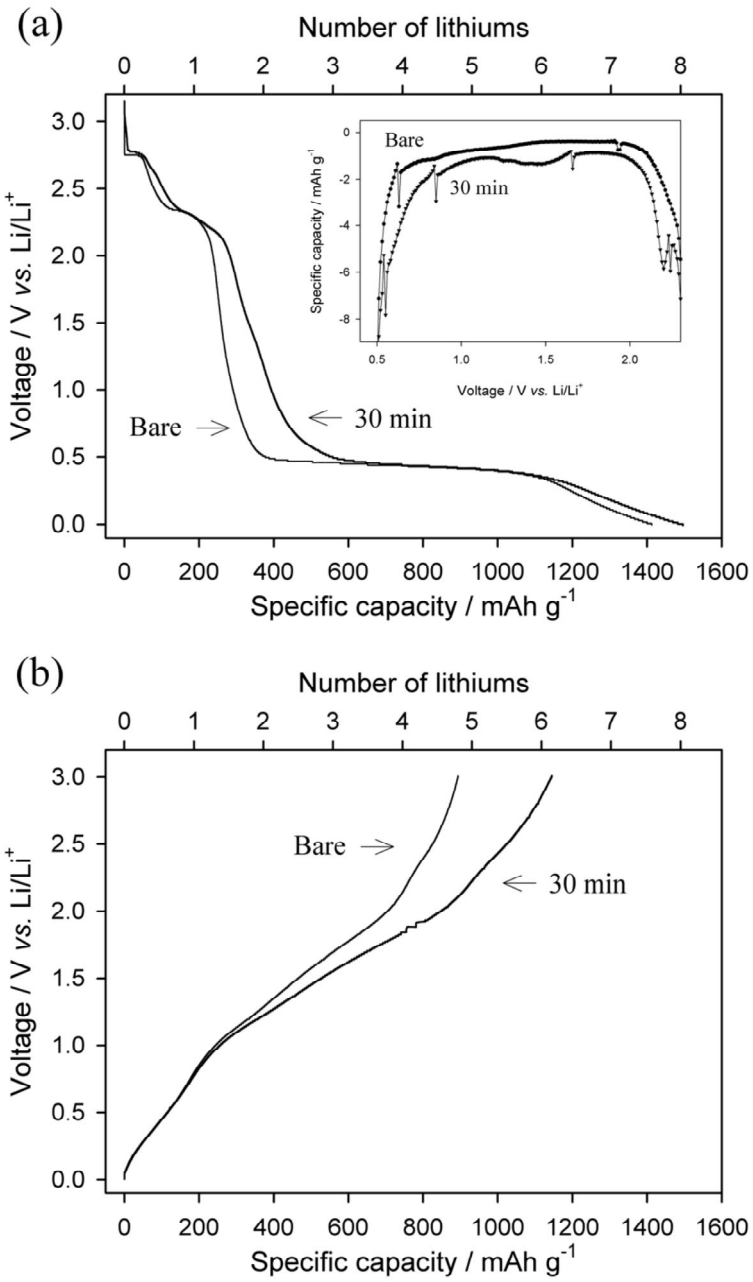


**Figure 30.** The voltage – capacity profiles in EVS of bare and 30 min ball-milled $MoO_3$ electrodes during (a) lithiation and (b) de-lithiation. Inset in (a) indicates the capacity at each step in voltage range of 0.5 ~ 2.3 V (*vs.* $Li/Li^+$).

The standard reaction potential of this reaction is determined by the standard Gibbs free energy of reaction, which is the difference of standard Gibbs free energy of formation between reactant and product (refer to equation (3) in *Chapter 2.1.*).

$$E^0 = \left[\Delta G_f^0(Li_xMoO_3) - 3\Delta G_f^0(Li_2O)\right] \Big/ nF$$

The insertion of lithium ions in amorphous $MoO_3$ particles results in amorphous $Li_xMoO_3$. It is widely known that, in the same material, the amorphous form is more unstable than crystalline form.[150] Thus, in this situation, standard Gibbs free energy of formation of amorphous $Li_xMoO_3$ should be larger than that in crystalline phase as in.

$$\Delta G_{f\ amor}^0(Li_xMoO_3) = \Delta G_{f\ crys}^0(Li_xMoO_3) + \delta G$$

Another issue for grinded surface and tens of nanometric particles in ball-milled $MoO_3$ is the surface area. Since the grinded surfaces of micro-sized particles and the size of particles peeled off by ball-milling is tens of nanometers, the surface area of them should be extremely larger than bare $MoO_3$ particle. The standard Gibbs free energy of formation of $Li_xMoO_3$ having extremely large surface area also different than that of bulk $Li_xMoO_3$ particle as in:

$$\Delta G_f^0(Li_xMoO_3) = \Delta G_f^0(Li_xMoO_3)_{r\to\infty} + \sum_\alpha 2\left(\gamma/r\right)V$$

where γ is the effective surface tension, V is the partial molar volume, and r is the effective grain radius.[151] Due to these two reasons, the standard Gibbs free energy of

formation of $Li_xMoO_3$ in ball-milled $MoO_3$ electrode is larger, and thus, the reaction voltage of conversion reaction is higher than that of bare electrode. Note that, such increasing reaction voltage should occur in the grinded surfaces and tens of nanometric particles formed by ball-milling, not in bulk micro-sized particles in ball-milled $MoO_3$. That is why the only $Li_xMoO_3$ corresponding to capacity around 200 mAh $g^{-1}$ in 30 min electrode reacts at higher reaction voltage than that in bare electrode, and a reminder reacts at the same voltage with bare electrode (overlapping region around 0.5 V (*vs.* $Li/Li^+$) in Fig. 29a).

From the EVS profiles during de-lithiation (Fig. 29b), it is also confirmed that the de-conversion reaction capacity, above 0.8 V (*vs.* $Li/Li^+$), in two electrodes are different thermodynamically. The resistance difference above 1.5 V (*vs.* $Li/Li^+$) mentioned in Fig. 24 is, therefore, originated from the thermodynamic difference, not kinetic issues.

As mentioned above, the grinded surfaces and tens of nanometric particles formed by ball-milling react with lithium at the higher reaction voltage than that in bare electrode, in lithiation process (Fig. 29a). Likewise, enlarged capacity in 30 min electrode, during de-lithiation, also must be originated from them (Fig. 29b). Fig. 30 illustrates the proposed lithiation and de-lithiation process to explain such behaviors of bare and 30 min electrodes. In the process of de-lithiation, the extraction of lithium ions and the oxidation of molybdenum should begin at the surface of bulk phase. Since

the molybdenum oxide having +6 valence has poor electric conductivity (smaller than $10^{-6}\,S\,m^{-1}$, $MoO_2$ (around $1.1 \times 10^{6}\,S\,m^{-1}$)), $MoO_{3-x}$ formed at the surface of

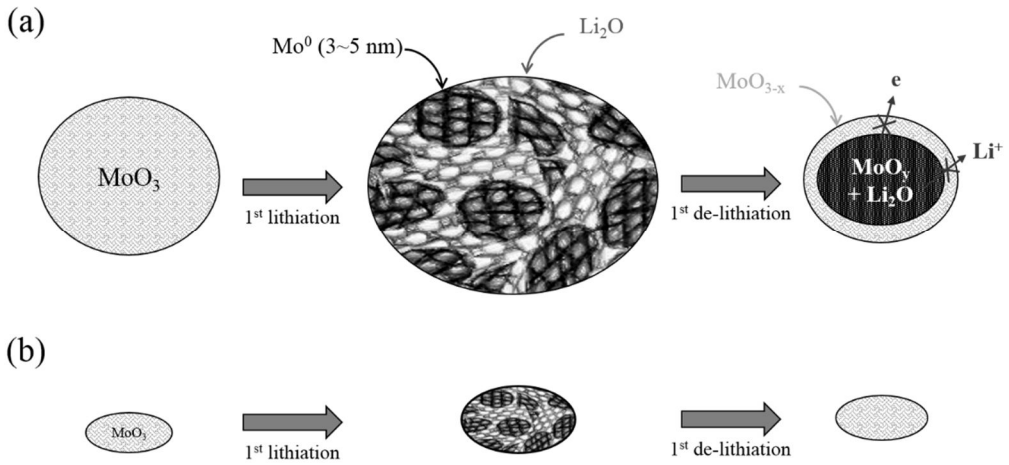


**Figure 31.** Schematic illustration of lithiation and de-lithiation processes of (a) bare and (b) 30 min ball-milled $MoO_3$ electrodes. Note that the size of $MoO_3$ in (a) is about 10 μm, whereas about 50 nm in (b).

bulk phase obviously hinders further oxidation of Mo or $MoO_y$ presented in inner space.[152-153] This phenomenon is occurring due to the characteristic of oxidation reaction of molybdenum, which is stepwise oxidation:

$$Mo^0 \rightarrow Mo^{4\pm\delta} \rightarrow Mo^{6-\delta} \quad (7)$$

In addition, owing to the short lithium ion and electron diffusion length, they are free for the hindrance by electric insulator ($MoO_{3-x}$) during de-lithiation, and therefore, the complete oxidation of inner molybdenum oxide spices can be feasible. For this reason, the latter oxidation of reaction (7) in around 2 ~ 3 V (*vs.* $Li/Li^+$) can occur more easily. Therefore, 30 min electrode shows the lower resistance obtained by GITT (Fig. 24) and higher de-lithiation capacity in this voltage range than bare electrode (Fig. 20 and 27).

Since the small sized $MoO_3$ particles show the better electrochemical performance, especially ICE, it is necessary to increase the amount of these particles. In this experimental, easy way to do is the increase in ball-milling time. As seen in FE-SEM images, BET surface areas (Fig. 18) and XRD patterns (Fig. 19), a lot of tens of nanometric particles, enlarged surface area, and more amorphous nature can be obtained by increasing ball-milling time. Unfortunately however, their electrochemical performances are different with such expectation. Fig. 32 shows the first-cycle voltage – capacity profiles and de-lithiation dQ/dV plots of 30 min, 2 h, and 4 h ball-milled $MoO_3$ electrodes (designated as 2 h and 4 h electrode, respectively, hereafter) and their lithiation / de-lithiation capacity and ICE are indicated in Table 6. Although the first-cycle lithiation capacity of three electrodes are still similar (1503, 1442, 1463 mAh $g^{-1}$

for 30 min, 2 h, and 4 h electrodes, respectively), the de-lithiation capacity (1176, 1057, 648 mAh $g^{-1}$) and ICE (78.2, 73.3, 44.3 %) of them decrease significantly. The main reason seems to be a water-soluble nature of $MoO_{3-x}$. As mentioned in Fig. 19, the color of powder becomes dark, which means the surface of $MoO_3$ is getting slightly reduced. Since $MoO_{3-x}$ is known to be much more soluble in water than $MoO_3$ and binder used in this study is water-based SBR-CMC, $MoO_{3-x}$ electrode inevitably has poor dispersion property. Such problems in electrode fabrication process results in poor electrochemical performance in 2 h and 4 h electrodes. As seen in Fig. 33b, there are many cracks in long-time ball-milled $MoO_{3-x}$ electrodes, which is maybe due to that they dissolved in solvent (water) and dried. In addition, due to long time ball-milling, the crushed small sized particles are aggregated to reduce surface energy (Fig. 33a),[154] which also results in the dispersion problem in electrode and poor electrochemical performance. As mentioned in *Chapter 4.1.*, the Mo valence, that is x in $MoO_{3-x}$ can be obtained by TG analysis in air and $N_2$ atmosphere. As seen in Fig. 34, bare and 5 min, 30 min ball-milled $MoO_3$ shows no difference profile in air and $N_2$ atmosphere, whereas different in 4 h ball-milled $MoO_3$, around 0.34 %. From this value, x in $MoO_{3-x}$ is calculated as 0.03, or $MoO_{2.97}$. In fact, although the reduced species are presented in the surface of oxide, it is deduced that the amount of reduction is small.

It is interesting that 30 min and 2 h electrodes show a different behavior only in around 2.5 V (*vs.* $Li/Li^+$) in Fig. 32b. The nature of this oxidation reaction can be

ascertained by *ex-situ* XANES experimental before and after 2.5 V (*vs.* $Li/Li^+$) peak. As

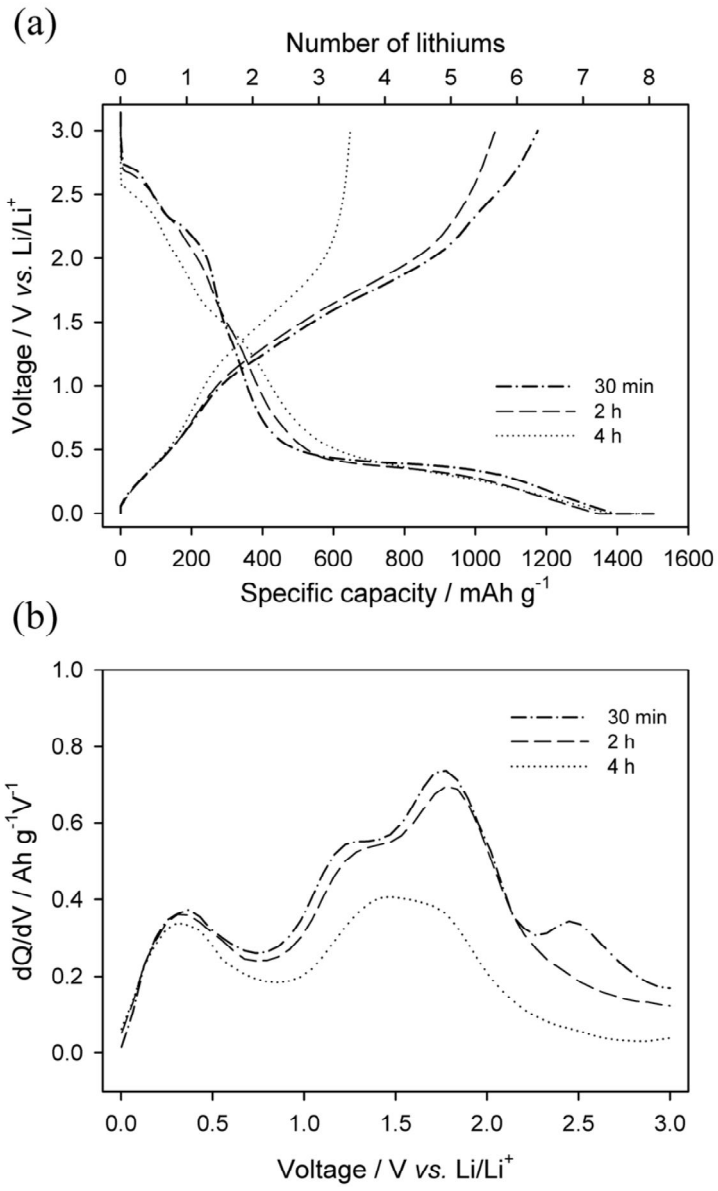


**Figure 32.** (a) The first-cycle voltage – capacity profiles and (b) de-lithiation dQ/dV plots of electrodes for 30 min, 2 h, and 4 h ball-milled $MoO_3$ electrodes.

**Table 6.** The first-cycle lithiation / de-lithiation capacity and the initial Coulombic efficiency of 30 min, 2 h, and 4 h ball-milled $MoO_3$ electrodes.

| The first cycle | Lithiation capacity (mAh $g^{-1}$) | De-lithiation capacity (mAh $g^{-1}$) | Coulombic efficiency (%) |
|---|---|---|---|
| 30 min | 1503 | 1176 | 78.2 |
| 2 h | 1442 | 1057 | 73.3 |
| 4 h | 1463 | 648 | 44.3 |

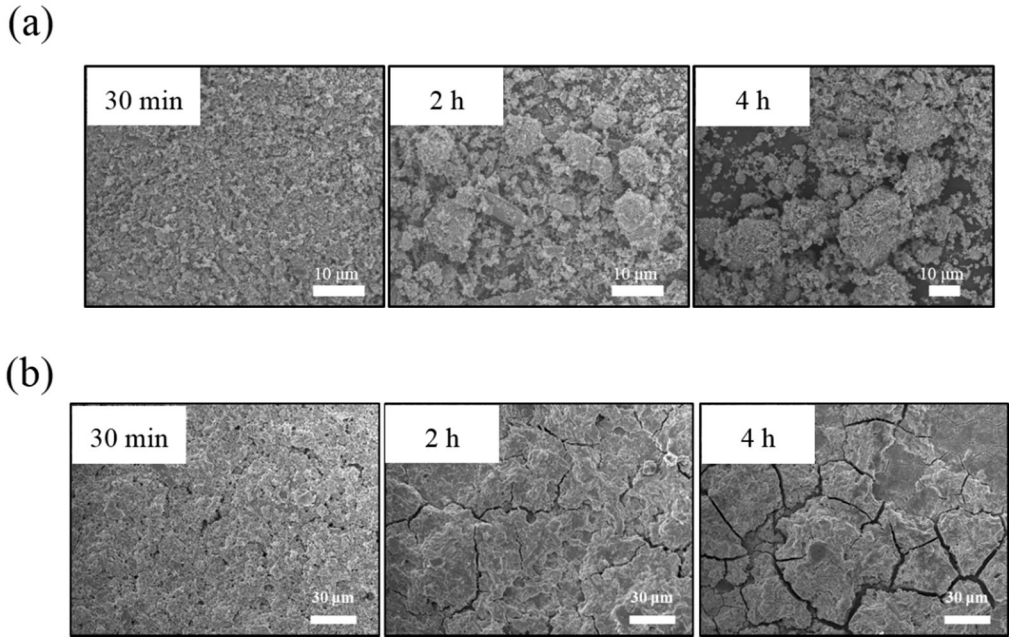


**Figure 33.** FE-SEM images of 30 min, 2 h, and 4 h ball-milled $MoO_3$ (a) powders and (b) electrodes with low magnification. Note that aggregates and cracks in 2 h and 4 h.

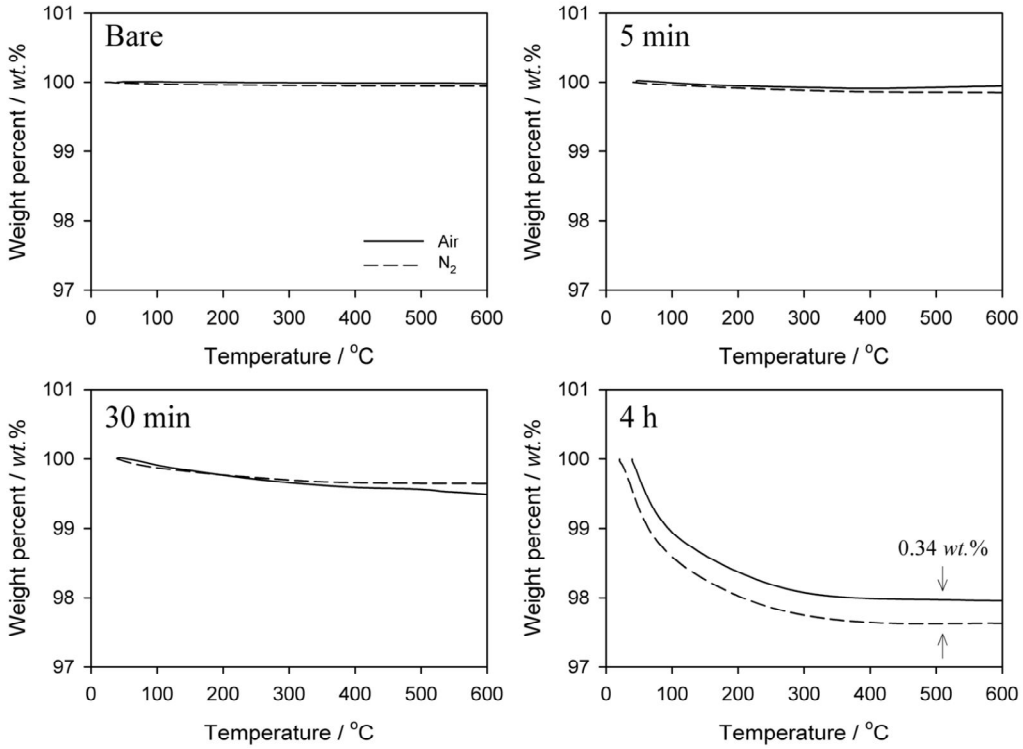


**Figure 34.** TG analysis of bare and 5 min, 30 min, 4 h ball-milled $MoO_3$ powders. Note that different weight percent profiles between air and $N_2$ atmosphere only in 4 h sample.

seen in Fig. 35, there is no pre-edge in de-lithiated 30 min electrode until 2.2 V (*vs.* $Li/Li^+$). That means the Mo valence is still +4, and therefore, the de-lithiation reaction at around 2.5 V (*vs.* $Li/Li^+$) should be the oxidation reaction of $Mo^{+4}$ to $Mo^{+6}$, the latter of reaction (7). It seems to be due to that, since the Mo valence of 2 h ball-milled $MoO_3$ ($MoO_{3-x}$) is not +6, the amount of capacity in latter of reaction (7) should be reduced, as well as the poor de-conversion reaction because of problems in electrode fabrication.

Cycle performance of these electrodes are indicated in Fig. 36. In ball-milled $MoO_3$ until 30 min, the specific capacity and its retention are enhanced, which behavior is evidently due to the same reason for the enhancement of capacity and ICE. It is interesting that capacity is increasing in bare, 5 min, and 30 min electrodes during cycling, and it even exceeds the theoretical capacity of $MoO_3$ (1117 mAh $g^{-1}$). The reason seems to be that, according to cycling, the particles are pulverized and electrochemically grinded. Thus, the use of full range of Mo valence (6 $Li^+$/electrons per formula unit) can be thermodynamically and kinetically feasible by the same reason in ball-milling effects. In addition, since there are also capacity from the surface reaction (polymer/gel-like film formation & dissolution, about 200 mAh $g^{-1}$, mentioned in Fig. 16), capacity around 1400 mAh $g^{-1}$ can be obtained in 30 min electrode. However, cycle performances are poorer after 2 h ball-milling because of problem in electrode fabrication mentioned above. In fast charging/discharging (500 mAh $g^{-1}$), the difference in cycleability is also observed (Fig. 36b). Therefore, it can be deduced that

the ball-milling of $MoO_3$ improves the cycle performance, as well as the first-cycle delithiation

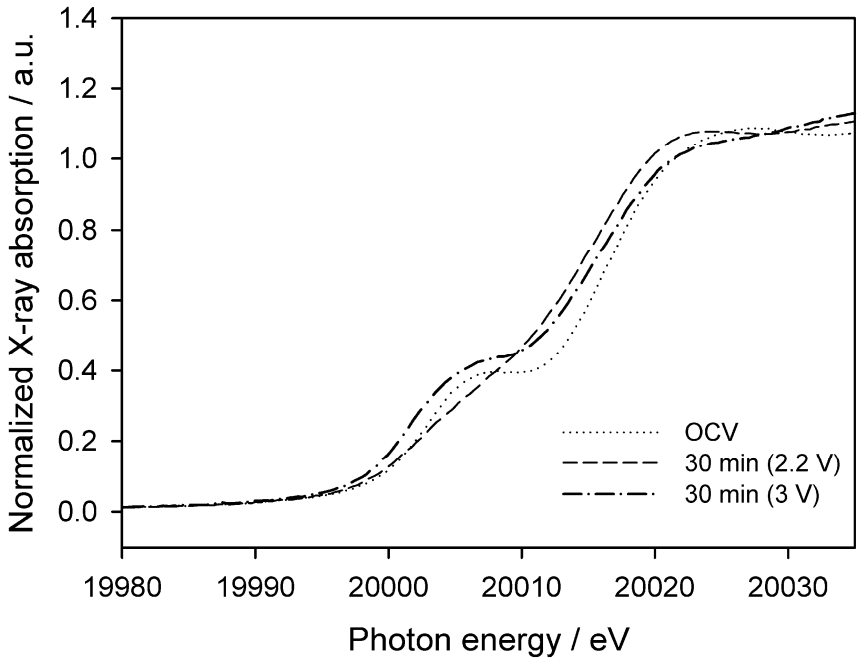


**Figure 35.** *Ex-situ* XANES spectra for 30 min ball-milled $MoO_3$ electrode after de-lithiation until 2.2 V and 3 V (*vs.* $Li/Li^+$). Spectra for bare electrode before cycling is also depicted as gray dash line (indicated as OCV).

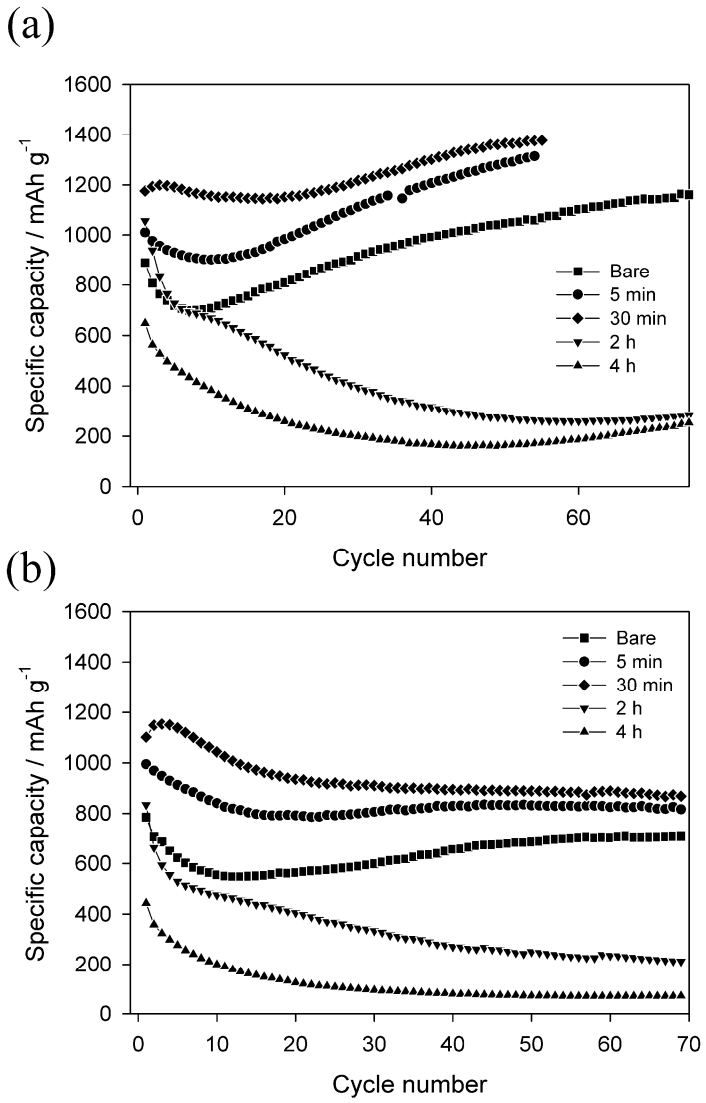


**Figure 36.** Cycle performance of bare and ball-milled $MoO_3$ electrodes at the current density of (a) 100 mA $g^{-1}$ and (b) 500 mA $g^{-1}$.

capacity and ICE, but unfortunately until 30 min.

Other ball-mill conditions such as ball-milling speed and ball to powder ratio also affects the electrochemical performances of ball-milled $MoO_3$ electrodes. Ball-milling speed and ball to powder ratio were varied, in which ball-milling time was fixed as 30 min (condition for the highest ICE in 300 rpm & 20:1 ratio). As seen in Table 7, there is no improvement in 100 rpm, and some improvement in 200 rpm & 20:1 and 400 rpm & after 10:1. Coincidently, the highest ICE was shown in 300 rpm & 20:1 among these conditions, which is the ball-milling condition set initially.

**Table 7.** Initial Coulombic efficiency of ball-milled $MoO_3$ electrodes with various ball-milling speed and ball to powder ratio.

| Initial Coulombic efficiency (%) | | Ball-milling speed (rpm) | | | |
|---|---|---|---|---|---|
| | | 100 | 200 | 300 | 400 |
| Ball to powder ratio | Bare | 60.8 | | | |
| | 5:1 | - | - | 62.1 | - |
| | 10:1 | 60.8 | 63.6 | 70.6 | 76.1 |
| | 20:1 | 62.0 | 74.4 | 78.2 | 78.0 |
| | 40:1 | - | 75.0 | 75.5 | - |

# 4. RESULTS AND DISCUSSION

## 4.3. An initial Coulombic efficiency higher than 100% observed for a $Li_2MoO_3$ electrode

Since *lithium-ion batteries (LIB)* has been commercialized, the need of high capacity LIB has been highlighted due to the application into hybrid electric vehicles (HEVs), electric vehicles (EVs) and high-capacity energy storage system (ESS).[2-3] The commercialized LIB consists of graphite as negative electrode and $LiCoO_2$ as positive electrode, which shows limited capacity because of small amount of lithium storage sites.[57, 121] In case of negative electrode, there were several efforts to develop high-capacity materials, such as alloys (Si, Sn, Zn, etc.) and transition metal oxides ($MO_x$ with M = Fe, Co, Ti, V, etc.) which can accept more than one lithium ion and electron per molecule.[9, 91, 155] Above all, several researches about transition metal oxides that

react with lithium through a conversion reaction have been studied, which shows high capacity through uptake of electrons up to its metallic state with the dissociation of metal – oxygen bond.[86, 125]

Until now, however, these materials are not used in practical LIBs. The major drawbacks to be overcome are the large voltage hysteresis and poor initial Coulombic efficiency (ICE). As mentioned in detail in *Chapter 2.3.2.1*., the latter problem results from two issues: (i) the irreversible electrolyte decomposition caused by catalytic effect on the surface of newly formed metal,[156] and (ii) poor reversibility for the metal (M) – oxygen (O) bond-forming reaction in the de-lithiation period ($M + 2\ Li_2O \rightarrow MO_2 + 4\ Li^+ + 4\ e$).[93, 127, 157] The ICE of negative electrode is one of the critical issues because it is directly related to energy efficiency and reversible capacity in full-cell configuration.

To date, for enhancement of the ICE of metal oxides, a great deal of research has been proceeding. Most of such studies, however, were focused on the surface treatment of active materials and electrolyte additives to reduce the irreversible electrolyte decomposition.[158-159] Unlike that, researches to improve the reversibility of conversion reaction, or enhance bond-forming reaction in de-lithiation process, by adding metal (M) have been also conducted. For instance, as indicated in reactions below, Fe was added in $Fe_2O_3$, and ternary metal oxide ($CuGeO_3$) was used.[145, 160-161] In case of $CuGeO_3$, Cu metal was generated before the reduction of Ge (IV) and it remained in its metallic state until the Ge metal was oxidized.

$$Fe_2O_3 + Fe` + 6Li^+ + 6e^- \leftrightarrow 2Fe + Fe` + 3Li_2O$$

$$CuGeO_3 + 2Li^+ + 2e^- \rightarrow Cu + GeO_2 + 2Li_2O$$

$$Cu + GeO_2 + 4Li^+ + 4e^- \leftrightarrow Cu + Ge + 4Li_2O$$

$$Ge + xLi^+ + xe^- \leftrightarrow Li_xGe$$

From these examples, it is confirmed that the extra metal component acts as follows: (i) the electrocatalyst for $Li_2O$ decomposition, (ii) the electrical network formation between metal and $Li_2O$ to facilitate the oxidation of metal. Both facts result in the improvement of reversibility of conversion reaction.

On the other hands, as a way to enhancing the bond-forming reaction, $Li_2O$ is added as a physical mixture with $MO_2$. Here, the bond-forming reaction is promoted since the concentration of $Li_2O$, which makes an intimate contact with metal component, are enlarged as a result of $Li_2O$ addition in the electrode preparation step. For example, CoO-$Li_2O$ composite film was prepared by the electrostatic spray deposition technique. [162] This additional $Li_2O$ acts as an oxidant to convert CoO into $Co_3O_4$ or even $Co_2O_3$ in the de-lithiation process like reactions below, increasing the de-lithiation capacity.

$$Li_2O + 3CoO \rightarrow Co_3O_4 + 2Li^+ + 2e^-$$

$$Li_2O + 2CoO \rightarrow Co_2O_3 + 2Li^+ + 2e^-$$

In this study, as an extension of such approach, $Li_2O$ was added as a molecular-

level mixture with $MO_2$ by preparing $Li_2MO_3$ to enhance the ICE of transition metal oxide. When the metal oxide component ($MO_2$) is lithiated by the conversion reaction, the $Li_2O$ component in $Li_2MO_3$ might be idling in the lithiated state. In the de-lithiation, however, this *idling* $Li_2O$ now can participates in the bond-forming reaction. In addition, since lithium ions and electrons move simultaneously, additional electrons should be supplied to release lithium ions from the idling $Li_2O$. That means metal oxide component must be oxidized further than its initial state by releasing additional electrons. It is known that molybdenum (Mo) and ruthenium (Ru) can have the stable valences as 4+ and 6+ in electrochemical cell, and thus we selected $Li_2MO_3$ (M = Mo and Ru) as active material and they showed > 100% Coulombic efficiency in the first cycle. This unusual behavior has been accounted for by the participation of idling $Li_2O$ in the bond-forming reaction. These materials can be good candidates as the negative electrode materials for LIBs because they show high de-lithiation capacity, high Coulombic efficiency and good cycle performance. Moreover, in virtue of unusually-high ICE, they can be blended with high capacity but poor efficiency materials such as $SiO_x$ which has been considered as active material of negative electrode for the practical LIBs.

Fig. 37 and 38 represents the voltage – capacity profiles of $Li_2MoO_3$ electrode and also 30 min ball-milled $MoO_2$ (99 %; Sigma-Aldrich) and $MoO_3$ (99.5 +%; Sigma-Aldrich) electrodes for the comparison. Since the particle size of oxides purchased in Sigma-Aldrich is too large to use as active materials, the ball-milled oxides are used as

control groups. $MoO_2$ electrode (Fig. 37a) shows typical insertion reaction at around 1.5 V (*vs.* $Li/Li^+$) and conversion reaction in constant voltage injection region at 0 V (*vs.* $Li/Li^+$). Although it was known that $MoO_2$ does not lithiated by a conversion reaction in room temperature [81], constant voltage at 0 V (*vs.* $Li/Li^+$) is extremely high reducing condition enough to break the Mo – O bond. $MoO_3$ electrode (Fig. 37b) also shows similar behavior, both insertion and conversion reaction at around 2.0 V (*vs.* $Li/Li^+$) and 0.5 V (*vs.* $Li/Li^+$), respectively. The different reactivity with lithium between $MoO_2$ and $MoO_3$ is caused by the difference of bond dissociation energy (bond dissociation energies of Mo – O in $MoO_3$ and $MoO_2$ are 565 kJ $mol^{-1}$ and 678 kJ $mol^{-1}$, respectively).[130]

$Li_2MoO_3$ electrode (Fig. 38a) exhibits the capacity in constant voltage injection region at 0 V (*vs.* $Li/Li^+$), similar as that of $MoO_2$ electrode. The reason seems to be the Mo valence of them is the same as +4, which means the similar bond strengths in $MoO_2$ and $Li_2MoO_3$. However, it should be figured out more clearly because $Li_2MoO_3$ is firstly considered as negative electrode. Fig. 38b shows the current – time profile in constant voltage step of $Li_2MoO_3$ electrode (gray line) and also virtual current profile for following the Cottrell behavior (gray dash line). Note that the current is indicated as the absolute value since the negative current is injected during lithiation. If there is only solid-state diffusion reaction in this step, the shape of current profile is similar with Cottrell equation driven profile ($i \propto t^{-1/2}$), but much more current flowed in case of constant voltage step in $Li_2MoO_3$ electrode. The reason is that the additional

reaction called nucleation reaction or two-phase reaction, occurs, which can be an evidence for a formation of new phase, metal and $Li_2O$ by the conversion reaction or metallic lithium by plating the lithium reaction at 0 V (*vs.* $Li/Li^+$). If the latter is true, the current is not

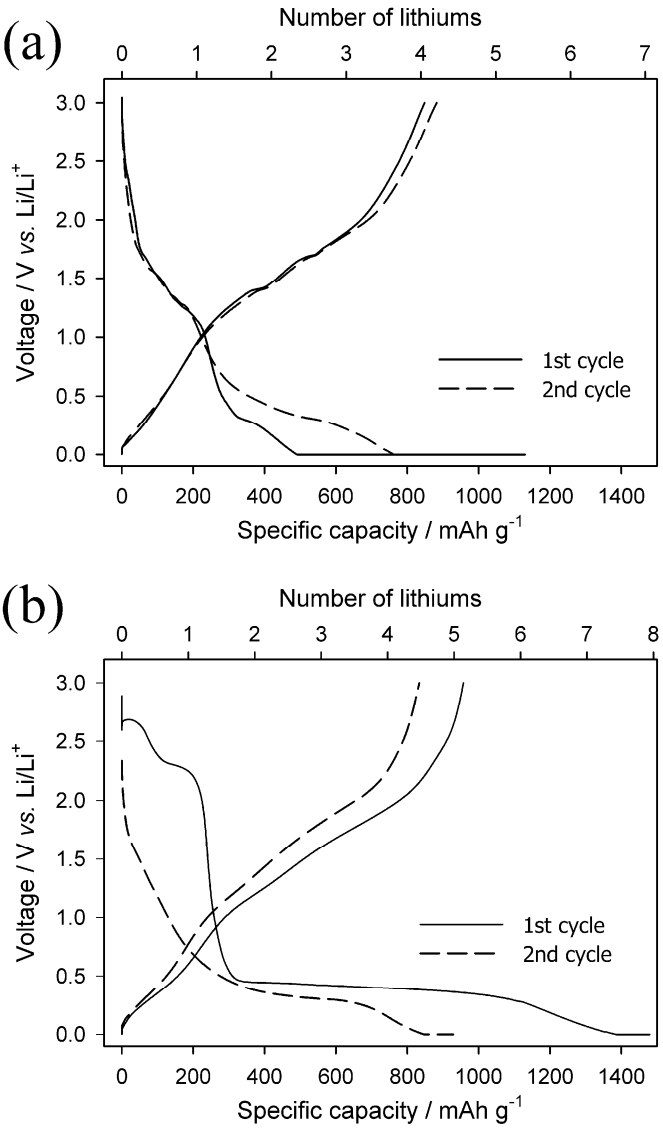




**Figure 37.** The first- and second-cycle voltage – capacity profiles of 30 min ball-milled (a) $MoO_2$ (99 %; Sigma-Aldrich) and (b) $MoO_3$ (99.5 +%; Sigma-Aldrich) electrodes.

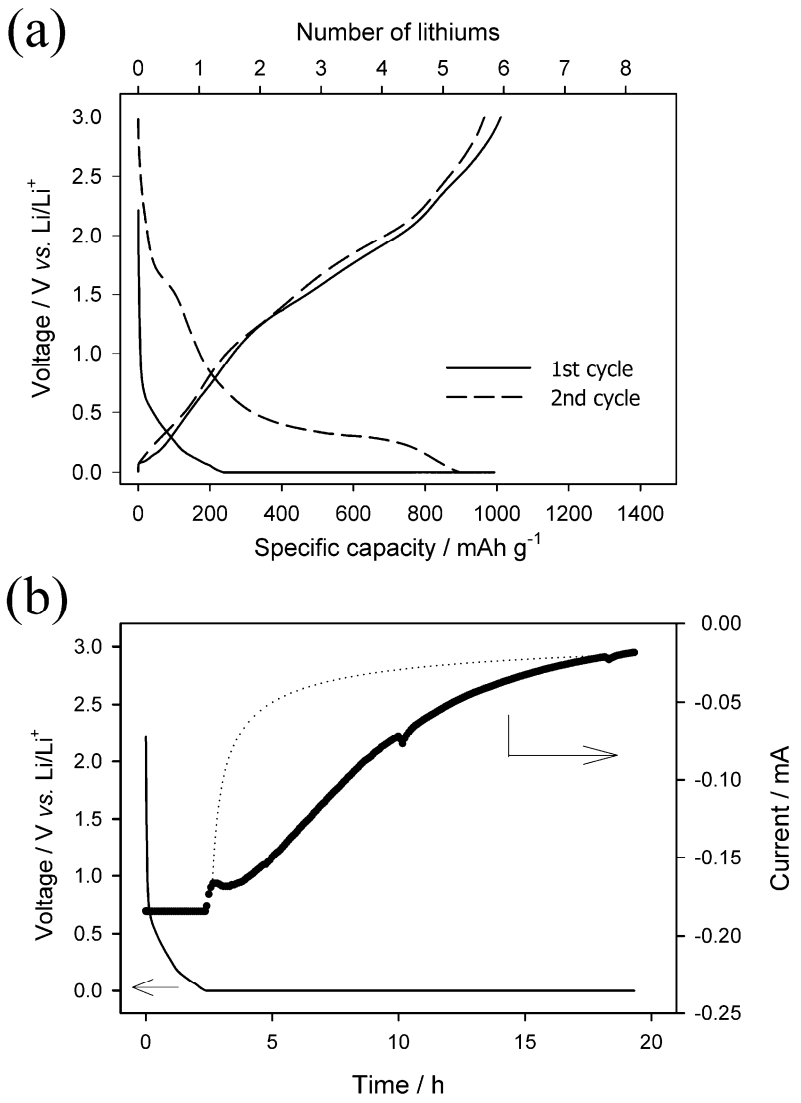


**Figure 38.** (a) The first- and second- cycle voltage – capacity profiles and (b) the current behavior of $Li_2MoO_3$ electrode in the first-cycle lithiation. Dotted line in (b) indicates the expected current profile for Cottrell behavior.

decayed to 0 mA due to the presence of almost infinite lithium sources in the counter electrode. However, reaction is finished by current decaying to around 0 mA, and thus, reaction mechanism of $Li_2MoO_3$ electrode should be bond breakage of transition metal oxide, not lithium plating. Through the *ex-situ* XRD, the conversion reaction of $Li_2MoO_3$ is also confirmed. As shown in Fig. 39, after the first-cycle lithiation of $Li_2MoO_3$ electrode, its high crystalline material changes to amorphous and/or nano-crystalline material, and this feature remains after the de-lithiation.

As indicated in Table 8, the first-cycle lithiation / de-lithiation capacity of 30 min ball-milled $MoO_2$ and $MoO_3$ electrodes are 1130 / 848 and 1479 / 1120 mAh $g^{-1}$, and ICE of them are 75.0 % and 75.7 %, respectively. On the other hands, $Li_2MoO_3$ electrode exhibit 955 / 1011 mAh $g^{-1}$, which results in 105.9 % ICE. Why $Li_2MoO_3$ electrode shows the ICE of > 100 %? $MoO_2$ and $MoO_3$ electrodes are lithiated by taking 4 $Li^+$/electrons and 6 $Li^+$/electrons per formula unit, respectively.

$$MoO_2\,(IV) + 4Li^+ + 4e^- \leftrightarrow Mo + 2Li_2O \quad (8)$$

$$MoO_3\,(VI) + 6Li^+ + 6e^- \leftrightarrow Mo + 3Li_2O \quad (9)$$

As seen in Figure 37, $MoO_2$ and $MoO_3$ electrodes release about 4 $Li^+$/electrons and 6 $Li^+$/electrons per formula unit in the first-cycle de-lithiation. Note that the de-lithiation capacity of these electrodes is well-matched with Mo valences, because it is de-lithiated by following the reverse of reaction (8) and (9), respectively. Nevertheless,

ICE of these electrodes is less than 80 % due to the irreversible charge consumption at the surface of

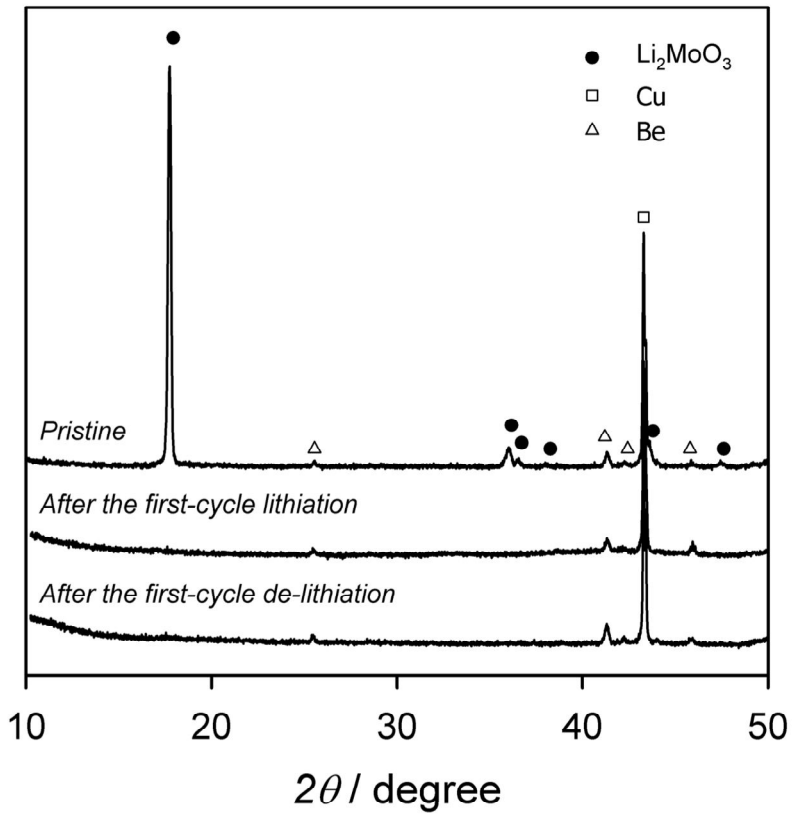


**Figure 39.** *Ex-situ* XRD patterns of $Li_2MoO_3$ electrode before cycling (pristine), after lithiation until 0 V (*vs.* $Li/Li^+$), and de-lithiation up to 3 V (*vs.* $Li/Li^+$). White square and triangles are peaks from copper current collector and beryllium window, respectively.

**Table 8.** The first-cycle lithiation / de-lithiation capacity and the initial Coulombic efficiency of $MoO_2$, $MoO_3$ and $Li_2MoO_3$ electrodes.

| The first cycle | Lithiation capacity (mAh $g^{-1}$) | De-lithiation capacity (mAh $g^{-1}$) | Coulombic efficiency (%) |
|---|---|---|---|
| $MoO_2$ | 1130 | 848 | 75.0 |
| $MoO_3$ | 1479 | 1120 | 75.7 |
| $Li_2MoO_3$ | 955 | 1011 | 105.9 |

newly formed metal in the lithiation process and poor reversibility of conversion reaction, as continually mentioned in *Chapter 2.3.2.1.*.

In contrast, $Li_2MoO_3$ electrode is reacted somewhat different with other electrodes as in.

$$Li_2MoO_3(IV) + 4Li^+ + 4e^- \rightarrow Mo + 2Li_2O + Li_2O \quad (10a)$$

$$Mo + 3Li_2O \rightarrow MoO_3(VI) + 6Li^+ + 6e^- \quad (10b)$$

$Li_2MoO_3$ can be regarded as the mixture of $Li_2O$ and $MoO_2$ with a molecular-level. To be exact, the $Li_2O$ component in $Li_2MoO_3$ is idling while $MoO_2$ component is lithiated by conversion reaction. As a result, even though only 4 $Li^+$/electrons are taken, the lithiated $Li_2MoO_3$ electrode consists Mo metal and 3 $Li_2O$ per formula unit. That state is the theoretically same with that in $MoO_3$ electrode, right-hand side of reaction (9) and (10a). In the de-lithiation, however, the idling $Li_2O$ component in $Li_2MoO_3$ electrode now participate in the bond-forming reaction, releasing 6 $Li^+$/electrons by following reaction (10b), which is the same with reverse of reaction (9). If the $Li_2MoO_3$ electrode is lithiated and de-lithiated according to reaction (10), its theoretical ICE should be 150 % due to taking 4 $Li^+$/electrons and releasing 6 $Li^+$/electrons per formula unit. However, it is obvious that there are severe irreversible charge consumption in the lithiation, which results in low measured ICE value than 150 %, 105.9 % in this study (Fig. 38a and Table 8). Nevertheless, to the best of our knowledge, it is a world record in negative electrode for LIBs.

The first-cycle de-lithiation dQ/dV plots of three electrodes are represented in Fig. 40. From these plot, what happens in $Li_2MoO_3$ electrode during de-lithiation can be examined precisely, compared with $MoO_2$ and $MoO_3$ electrode. As seen in arrow in Fig. 40, there are peaks around 2.5 V (*vs.* $Li/Li^+$) in $MoO_3$ and $Li_2MoO_3$ electrodes, whereas not in $MoO_2$ electrode. During de-lithiation, Mo metal in the $MoO_2$ electrode reacts with 2 $Li_2O$, which results in the oxidization up to 4+ by following the reverse of reaction (8). Mo metal in the $MoO_3$ and $Li_2MoO_3$ electrodes, however, can react with 3 $Li_2O$ to be generated $Mo^{6+}$ species by the reverse of reaction (9) or reaction (10b). Therefore, the oxidation peak at around 2.5 V (*vs.* $Li/Li^+$) can be designated as the oxidation reaction of $Mo^{4+}$ to $Mo^{6+}$ In other words, the fact that Mo valence in the de-lithiated $Li_2MoO_3$ electrode is 6+ is confirmed by this peak. Note that the oxidation reaction of $Mo^{4+}$ to $Mo^{6+}$ at 2.5 V (*vs.* $Li/Li^+$) in 30 min ball-milled $MoO_3$ electrode is already demonstrated by *ex-situ* XANES in Fig. 35 (*Chapter 4.2.*), and this reaction in $Li_2MoO_3$ electrode will be also discussed in latter section.

There are other electrochemical evidences for which $Li_2MoO_3$ electrode oxidizes up to the higher Mo valence than +4: comparison of lithiation capacity and OCV value in the first and second cycles. As indicating in Table 9, the second-cycle lithiation capacity of $Li_2MoO_3$ electrode (993 mAh $g^{-1}$) is higher than that of the first cycle (955 mAh $g^{-1}$), even though the large amount of irreversible capacity would be included in the first-cycle lithiation capacity. In addition, the initial voltage in the second cycle is higher than that in first cycle. These results are due to that Mo valence in $Li_2MoO_3$

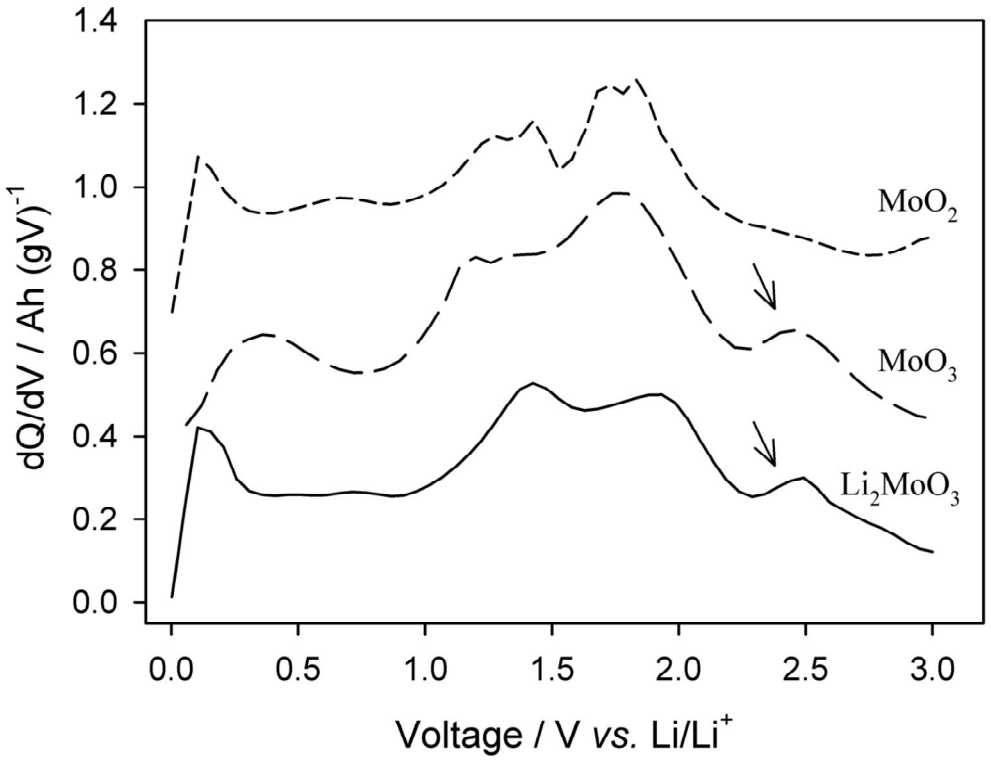


**Figure 40.** The first-cycle de-lithiation dQ/dV plots of $MoO_2$, $MoO_3$ and $Li_2MoO_3$ electrodes. Arrows are indicated the peak at around 2.5 V (*vs.* $Li/Li^+$).

**Table 9.** The lithiation capacity and initial voltage in the first and second cycle of $MoO_2$, $MoO_3$, and $Li_2MoO_3$ electrodes.

| | The 1st cycle lithiation capacity (mAh $g^{-1}$) | The 2nd cycle lithiation capacity (mAh $g^{-1}$) | Initial voltage in the 1st cycle (V) | Initial voltage in the 2nd cycle (V) |
|---|---|---|---|---|
| $MoO_2$ | 1130 | 951 | 3.04 | 2.99 |
| $MoO_3$ | 1479 | 1198 | 3.04 | 2.81 |
| $Li_2MoO_3$ | 955 | 993 | 2.22 | 2.98 |

electrode after the first-cycle de-lithiation (almost +6) is higher than that before cycling (+4). In $MoO_2$ and $MoO_3$ electrodes, however, different situations happen: the first-cycle lithiation capacity is higher than that in second cycle, and initial voltage in first cycle is higher than that in second cycle (Table 9). It is likely due to the poor reversibility of conversion reaction, and it is generally observed in conversion reaction-type transition metal oxides.

Even though Mo valence in $Li_2MoO_3$ electrode is 4+ before cycling, it should increase up to 6+ ($MoO_3$) to release 6 $Li^+$/electrons in the first-cycle de-lithiation. Thus, this phenomenon can be also demonstrated by tracing the change of Mo valence according to cycling. Fig. 41, 42, and 43 represent *ex-situ* Mo K-edge XANES spectra of $MoO_2$, $MoO_3$, and $Li_2MoO_3$ electrodes according to cycling. As mentioned in previous Chapters, XANES spectra of molybdenum are known to be different according to the valence, especially in a pre-edge region. A pre-edge appears when molybdenum located in the tetrahedral site, whereas not in octahedral site.[146] Since molybdenum ions in $MoO_2$ and $Li_2MoO_3$ are located in slightly distorted Mo – O octahedron and ordinary octahedron, respectively, the pre-edge does not appear in their spectra (Fig. 41a).[163] In contrast, $MoO_3$ crystallite has more complex structure with four short Mo – O bonds and two additional long Mo – O bonds, which makes a completely deformed octahedral coordination. Thus, the forbidden electronic transition between 1s and 4d is feasible, and pre-edge appears (Fig. 41a).[147] In addition, *ex-situ* EXAFS spectra of three electrodes before cycling also represent in Fig. 41b with the

corresponding bonds.[149, 163]

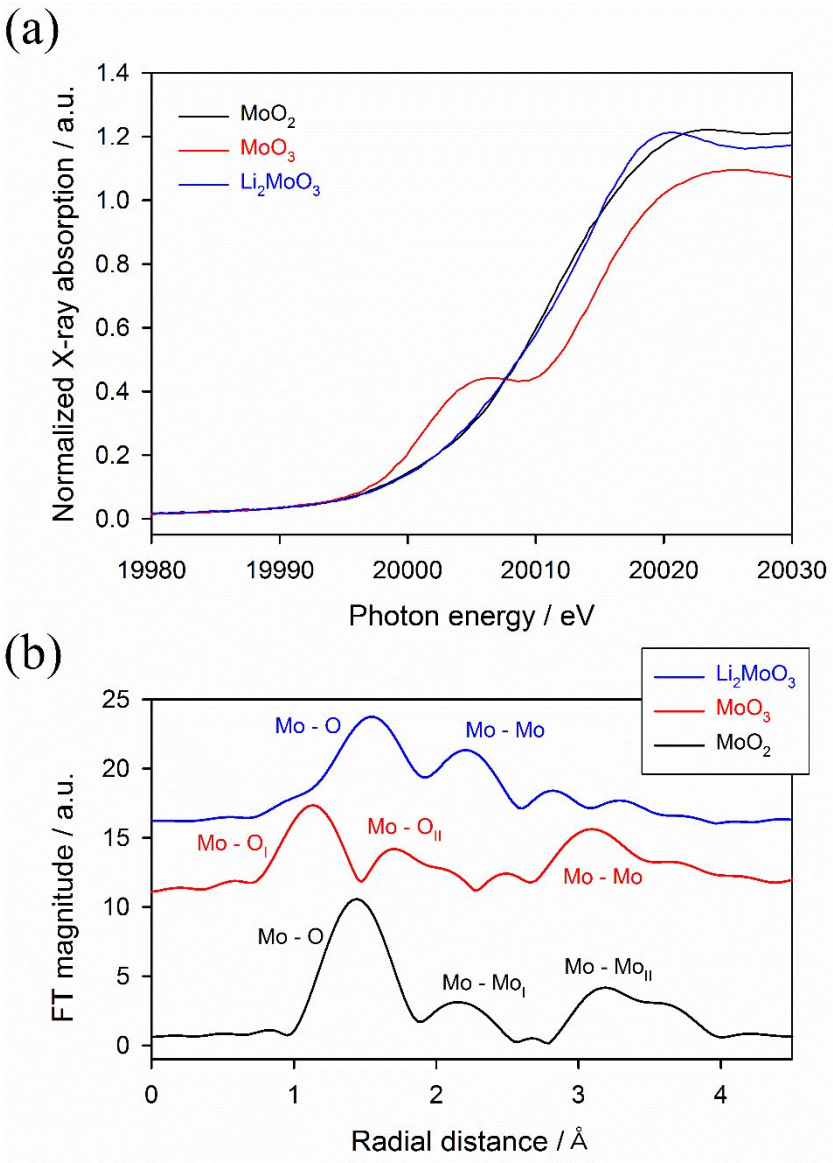


**Figure 41.** *Ex-situ* (a) XANES and (b) EXAFS spectra of $MoO_2$, $MoO_3$, and $Li_2MoO_3$ electrodes before cycling.

After the first-cycle lithiation, main edges of three electrodes move to main edge of molybdenum metal reference, which indicates that three electrodes are lithiated by conversion reaction (Fig. 42a). Note that main edges in $MoO_3$ and $Li_2MoO_3$ electrodes in Fig. 42a are located lower eV than molybdenum metal reference, whereas not in $MoO_2$ electrode. The reason seems to be that there are large amount of $Li_2O$ species, three per Mo metal generated by conversion reaction, and it can increase the electron density of nano-grained Mo metal. The reduction until Mo metal is also confirmed by EXAFS spectra (Fig. 42b).

As seen in Fig. 43a, after finishing the first cycle, spectra of $MoO_2$ and $MoO_3$ electrodes recover those spectra in before cycling. Note that pre-edge appears in $MoO_3$ electrode again. Interesting point is that pre-edge also can be observed in $Li_2MoO_3$ electrode, which location is the same with that in $MoO_3$ electrode. Since such pre-edge is an evidence for the existence of 6+ species, it can be deduced that Mo valence in the de-lithiated $Li_2MoO_3$ electrode is close to that in $MoO_3$, by releasing 6 $Li^+$/electrons per formula unit, as in reaction (10b). Formation of $MoO_3$-like species in $Li_2MoO_3$ electrode after the first cycle can be also confirmed by EXAFS spectra (Fig. 43b). Note that spectra of $Li_2MoO_3$ is much more similar with that in $MoO_3$ rather than $MoO_2$. Fig 44 shows the quantitative analysis of Mo valence after the first cycle by means of method already mentioned in *Chapter 4.1.*, which is the comparison of Mo K-edge shift at the half-height of main absorption edge. The results are as follows: the Mo

valence after the first cycle is $MoO_2$, $MoO_3$ and $Li_2MoO_3$ are about 3.7, 5.3, and 5.1, respectively.

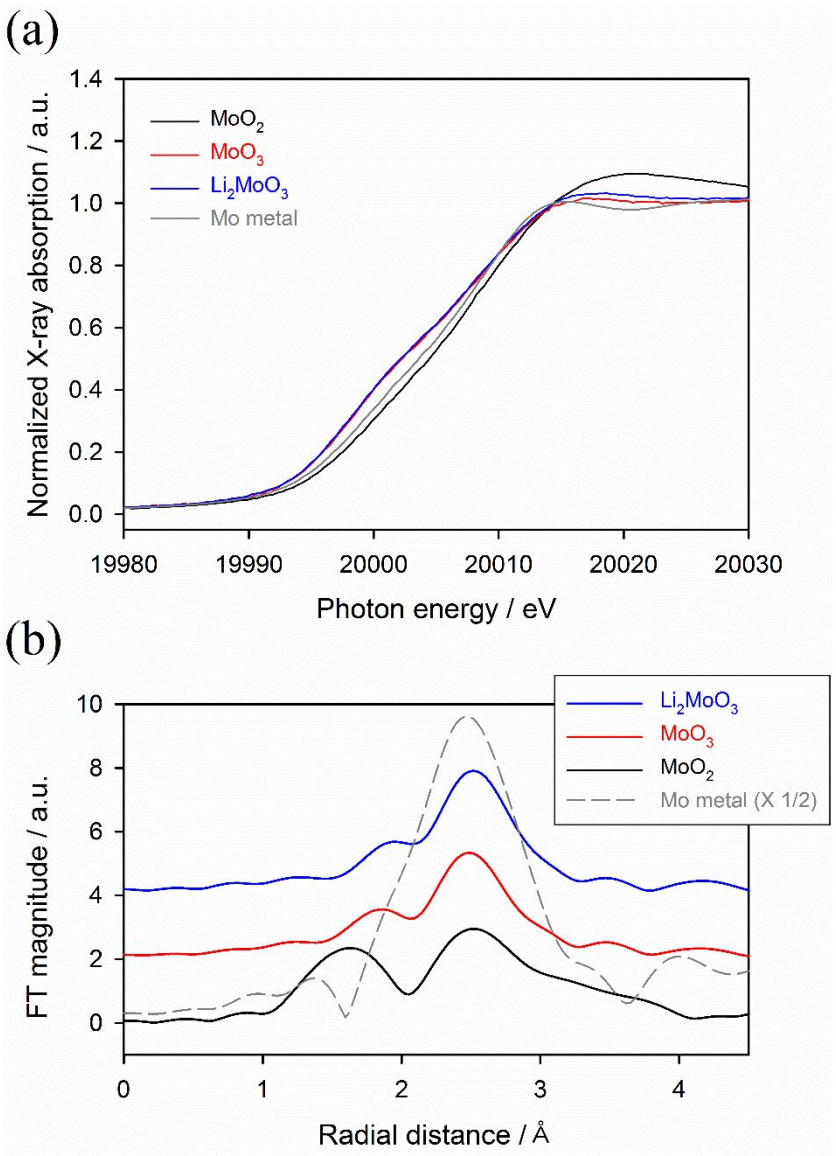


**Figure 42.** *Ex-situ* (a) XANES and (b) EXAFS spectra of $MoO_2$, $MoO_3$, and $Li_2MoO_3$ electrodes after the first-cycle lithiation. Reference Mo metal is also indicated and peak intensity of it in (b) decreases by half.

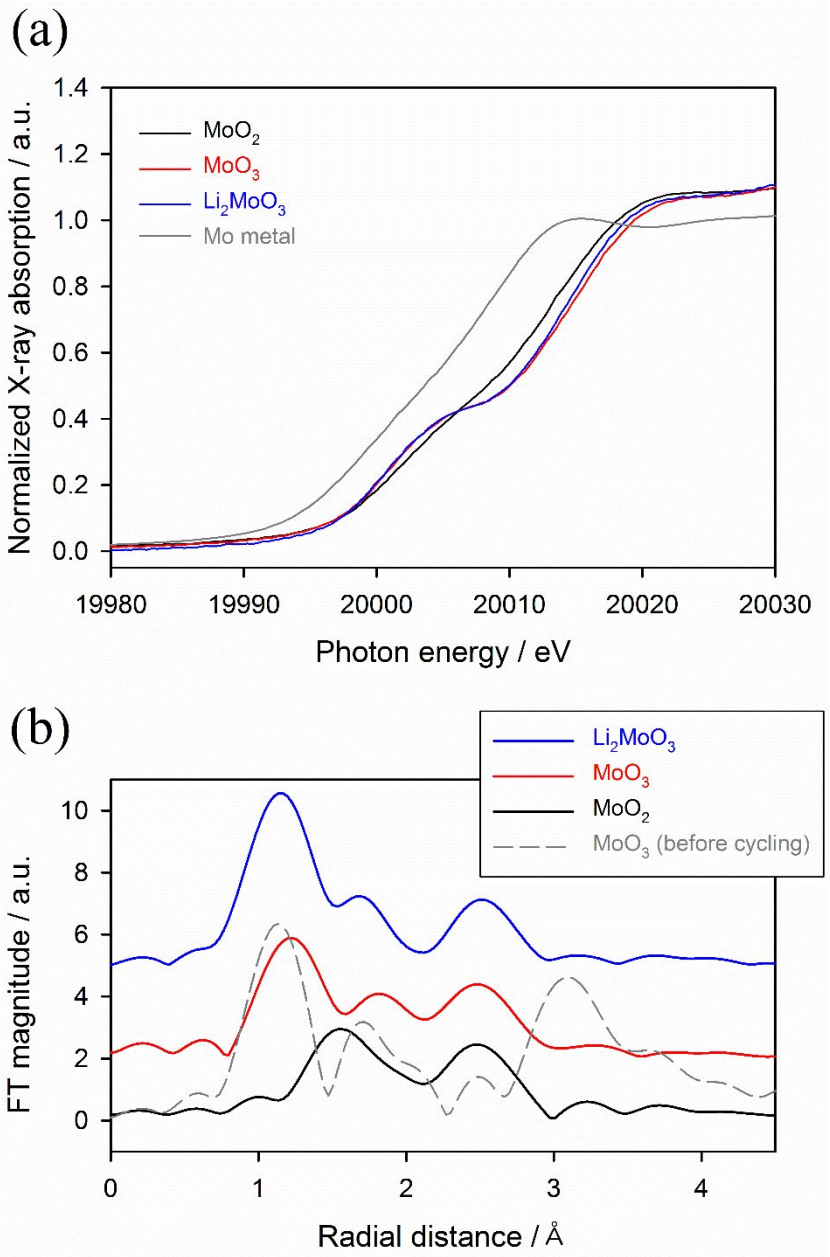


**Figure 43.** *Ex-situ* (a) XANES and (b) EXAFS spectra of $MoO_2$, $MoO_3$, and $Li_2MoO_3$ electrodes after the first-cycle de-lithiation. EXAFS spectra of $MoO_3$ before cycling is also depicted in (b) for the comparison.

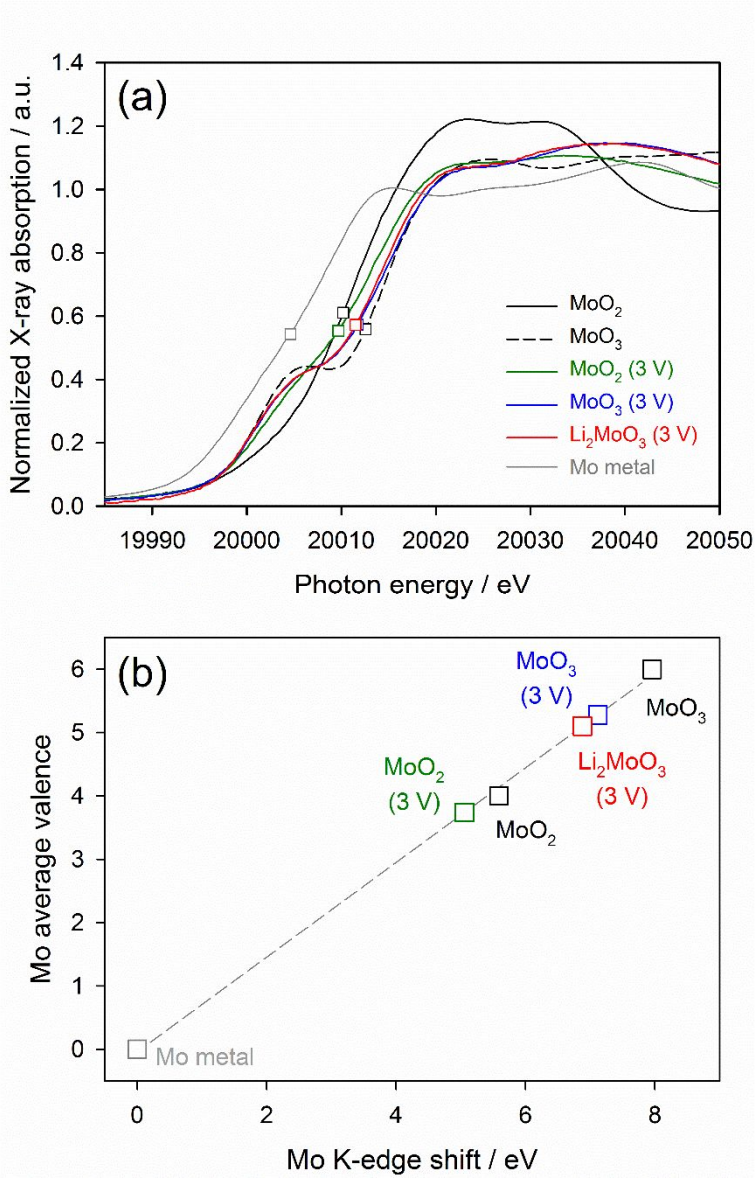


**Figure 44.** (a) *Ex-situ* XANES spectra of $MoO_2$, $MoO_3$ and $Li_2MoO_3$ electrode after the first cycle. Spectra of Mo metal and $MoO_2$, $MoO_3$ electrodes before cycling are also depicted for the reference. (b) The relationship between Mo K-edge shift energy derived from (a) and Mo valence.

Fig. 45 represents *ex-situ* XANES and EXAFS spectra of $Li_2MoO_3$ electrodes after the de-lithiation until 2.2 V (*vs.* $Li/Li^+$) to examine the nature of oxidation reaction at 2.5 V (*vs.* $Li/Li^+$), indicated by arrow in Fig. 40. Spectra of $Li_2MoO_3$ electrode at 2.2 V (*vs.* $Li/Li^+$) are similar with those of de-lithiated $MoO_2$ electrode, which means the Mo valence in that electrode is +4. Note that Mo – $O_I$ bond for $MoO_3$ (peak around 1 Å) is well-observed in 3 V (*vs.* $Li/Li^+$) de-lithiated $Li_2MoO_3$ electrode (blue line in Fig. 44b), whereas not in 2.2 V de-lithiated electrode (green line in Fig. 45b). Therefore, as expected in Fig. 40, it is demonstrated that the oxidation reaction occurring at 2.5 V (*vs.* $Li/Li^+$) should be the oxidation of $Mo^{4+}$ to $Mo^{6+}$, the latter of reaction (7) in *Chapter 4.2.*.

Based on these results, we suggests the reaction mechanism of $Li_2MoO_3$ (Fig. 46). From these results, it can be generalized with some requirements: (i) the added $Li_2O$ is idling during the lithiation and it participates in the bond-forming reaction in the de-lithiation, (ii) the supply of additional electrons in metal oxide component by oxidizing further than its initial valence, and (iii) stable after further oxidization. In addition, this phenomenon is well-achieved when $Li_2O$ is dispersed as a molecular-level mixture and an intimate contact with metal oxide component. Since $Li_2MoO_3$ electrode is satisfied with these requirements, it can show the ICE higher than 100 %.

Two additional experiments were conducted to support such suggested mechanism. The first one is the test for the proof of requirement (i). The electrode was fabricated using a composite of $Li_2O$ and $MoO_2$ prepared by planetary ball-miller with

same molar ratio (1:1). Ball-

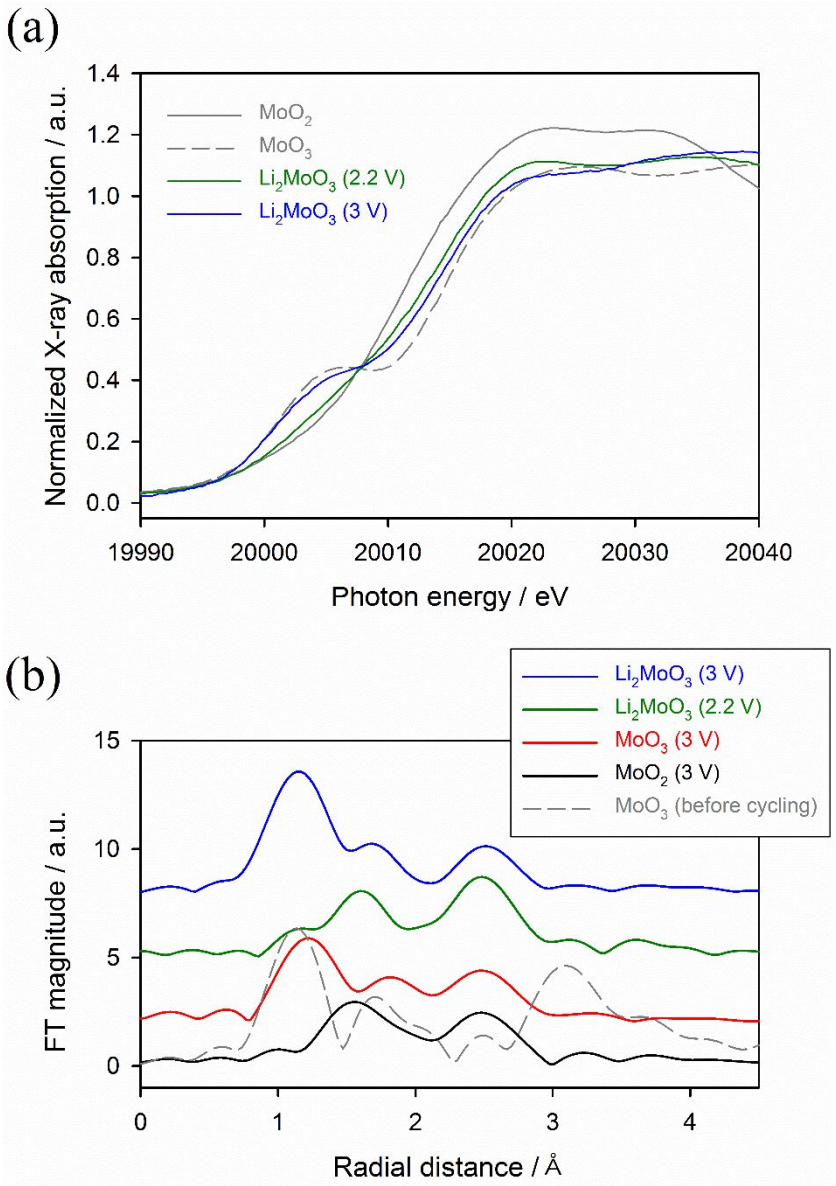


milling was conducted for 24 h with 500 rpm in Ar atmosphere due to



**Figure 45.** *Ex-situ* (a) XANES and (b) EXAFS spectra of the de-lithiated $Li_2MoO_3$ electrode until 2.2 V and 3 V (*vs.* $Li/Li^+$). For the comparison, spectra are also represented: $MoO_2$ and $MoO_3$ electrodes before cycling in (a), and after the first cycle in (b).

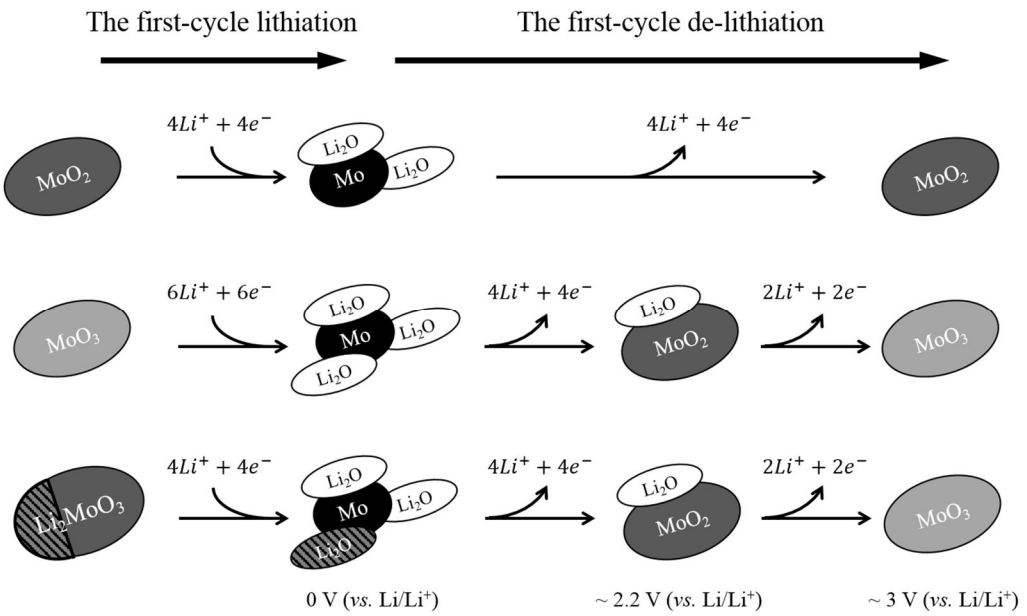


**Figure 46.** Schematic illustration of reaction mechanism of $MoO_2$, $MoO_3$ and $Li_2MoO_3$ electrodes during the first-cycle lithiation and de-lithiation processes.

maximize the degree of physical mixing and prevent the oxidation of $MoO_2$ (*Chapter 3.1.3.*). As shown in Fig. 47a, this electrode releases 5 $Li^+$/electrons per formula unit and shows 86.6 % ICE (1001 and 867 mAh $g^{-1}$ for the first-cycle lithiation and de-lithiation capacity, respectively), which is much higher than $MoO_2$ electrode, 75.0 %. In particular, in de-lithiation dQ/dV plot (Fig. 47b), 2.5 V (*vs.* $Li/Li^+$) peak which comes from the oxidation reaction of $Mo^{4+}$ to $Mo^{6+}$, mentioned in Fig. 40, is also observed in this composite electrode. From these result, it can be deduced once more that even physically added $Li_2O$ can participate in the bond-forming reaction if there are electrons suppliers on the periphery of $Li_2O$, molybdenum ions in this case. (Note that, in this ball-milled composite electrode, due to high ball-milling energy with long ball-milling time, the nature of metal oxide could be somewhat amorphous. As discussed in *Chapter 4.1.*, amorphous metal oxide has a lot of defects sites which can acts as storage sites of lithium ions, and its reversibility is fairly higher than that of conversion reaction. Therefore, in the high ICE of physical mixture of $MoO_2$ and $Li_2O$ formed by high-energy ball-milling, the effect of amorphization of metal oxide is also included.)

The second experiment is the usage of a different material, $Li_2RuO_3$, to demonstrate requirements (ii) and (iii). Although the valence of most ruthenium oxides are 4+, $Ru^{6+}$ can also be generated by electrochemically.[164] In the de-lithiation up to 4 V (*vs.* $Li/Li^+$), $RuO_2$ (99.9 %; Sigma-Aldrich) electrode showed 90 % of ICE (Fig. 48a) even though it remains its valence as 4+, due to the oxidation of SEI, as reported in

Maier group.[95] When $Li_2RuO_3$ electrode is de-lithiated, however, it shows about 120 % of ICE (Fig.

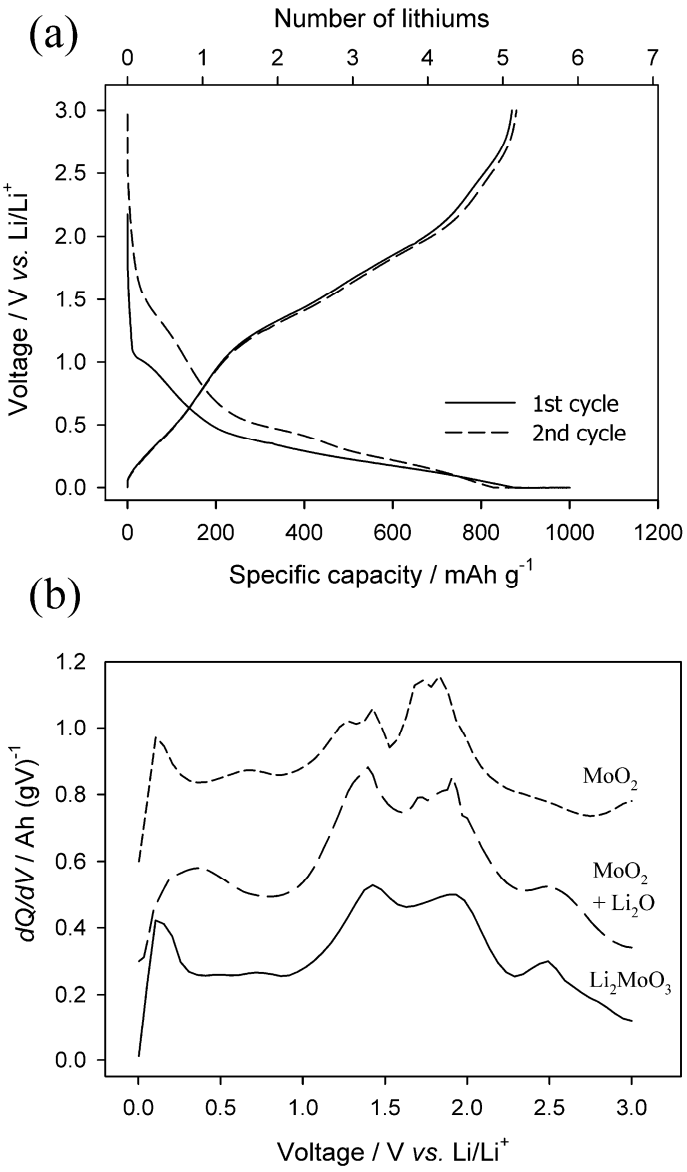


**Figure 47.** (a) The first- and second-cycle voltage – capacity profiles and (b) the first-cycle de-lithiation dQ/dV plots of a composite electrode consisting a physical mixture of $MoO_2$ and $Li_2O$ electrode. The first-cycle de-lithiation dQ/dV plots of $MoO_2$ and $Li_2MoO_3$ electrodes are also indicated in (b) for

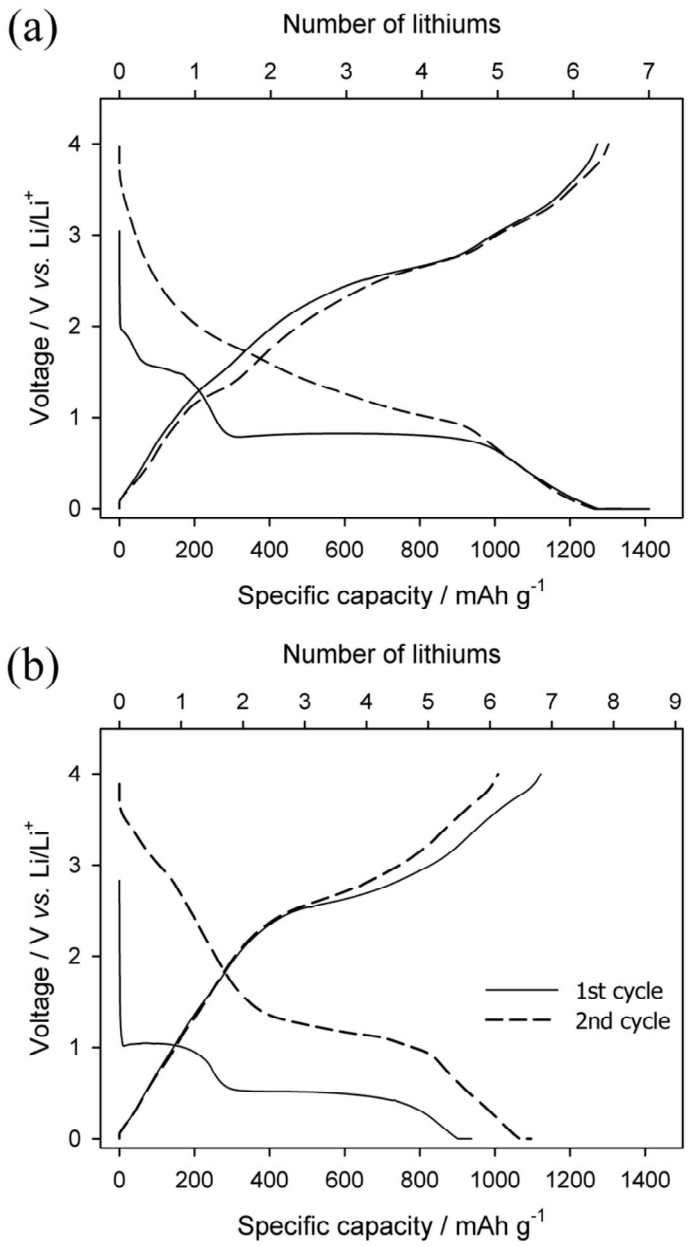


**Figure 48.** The first- and second- voltage – capacity profiles of (a) $RuO_2$ (99.9 %; Sigma-Aldrich) and (b) $Li_2RuO_3$ electrodes.

48b). In addition, the second-cycle lithiation capacity (1096 mAh $g^{-1}$) is much higher than that in the first-cycle lithiation (938 mAh $g^{-1}$), similarly with in the case of $Li_2MoO_3$ electrode. That means $Li_2RuO_3$ electrode also follows the suggested mechanism as in $Li_2MoO_3$ electrode, that is, 6 $Li^+$/electrons per formula unit are released by oxidizing up to 6+ in the first-cycle de-lithiation.

Fig. 49 indicates the cycle performance and rate capability of the $Li_2MoO_3$ electrode. It shows 900 mAh $g^{-1}$ in the 50$^{th}$ cycle with 97.8 % Coulombic efficiency and good rate capability (600 mAh $g^{-1}$ with 2 A $g^{-1}$), as well as good in the first cycle. These performances are outstanding among other reported conversion reaction-type metal oxides. Moreover, since its ICE is extremely high, it can be blended with poor Coulombic efficiency materials such as SiO. Although SiO electrode shows high specific capacity, the poor ICE has been a major drawback to use in the practical LIBs. When $Li_2MoO_3$ and SiO (Sigma-Aldrich) are mixed with a weight ratio of 1:1 by just hand-mixing, the ICE of this composite electrode is much enhanced from 54.7 % to 77.4 %, remaining similar the first-cycle de-lithiation capacity (Fig. 50 and Table 10). The calculated value in Table 10 is given by the average of measured lithiation and de-lithiation capacity from SiO and $Li_2MoO_3$ electrodes. The higher ICE in the measured value than the one calculated (69 %) is because of the enhancement of kinetic properties in virtue of the high electric conductivity of Mo metal. Since it remains at the potential where the de-alloying of Li-Si phase takes place, around 0.4 V (*vs.* Li/$Li^+$), Mo metal can facilitate the de-alloying reaction of Li-Si phase (indicated as arrow in

Fig. 51).

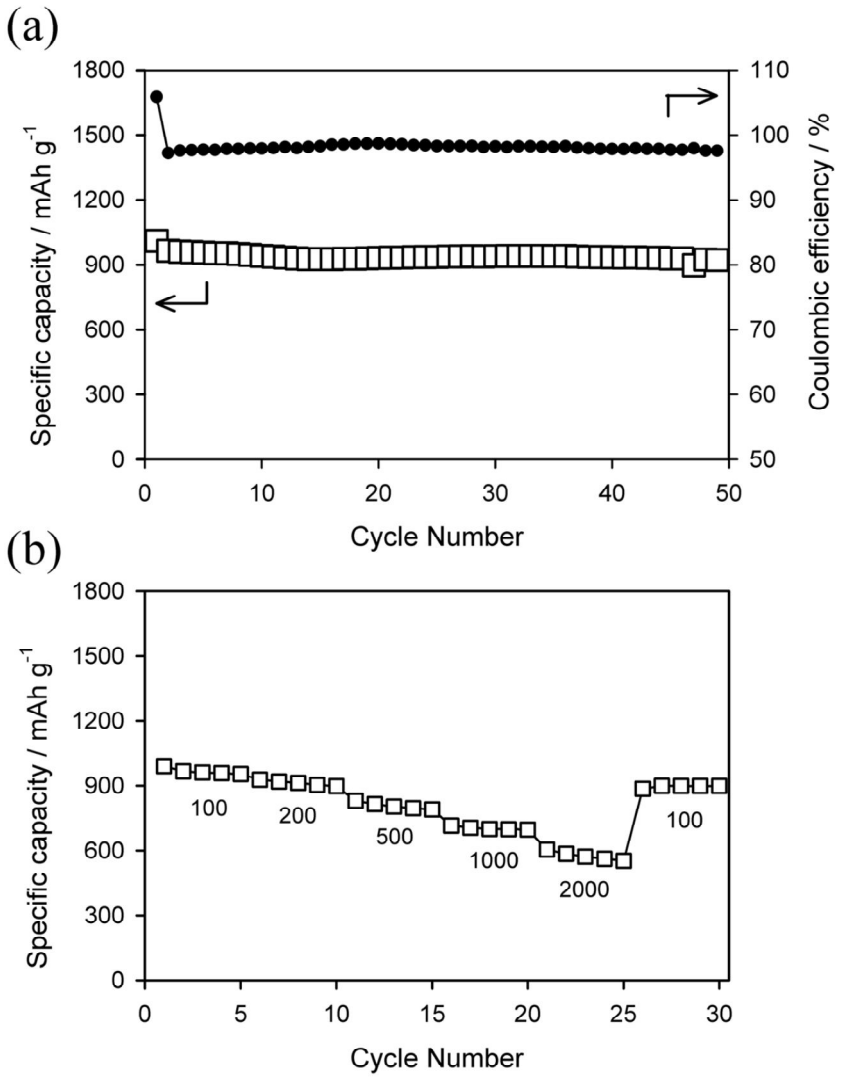


**Figure 49.** (a) Cycle performance with current density of 100 mA $g^{-1}$ and (b) rate performance of $Li_2MoO_3$ electrodes over voltage range of 0 ~ 3 V (*vs.* $Li/Li^+$). Only the de-lithiation capacity is shown, and current density (in mA $g^{-1}$) is indicated below the data points in (b).

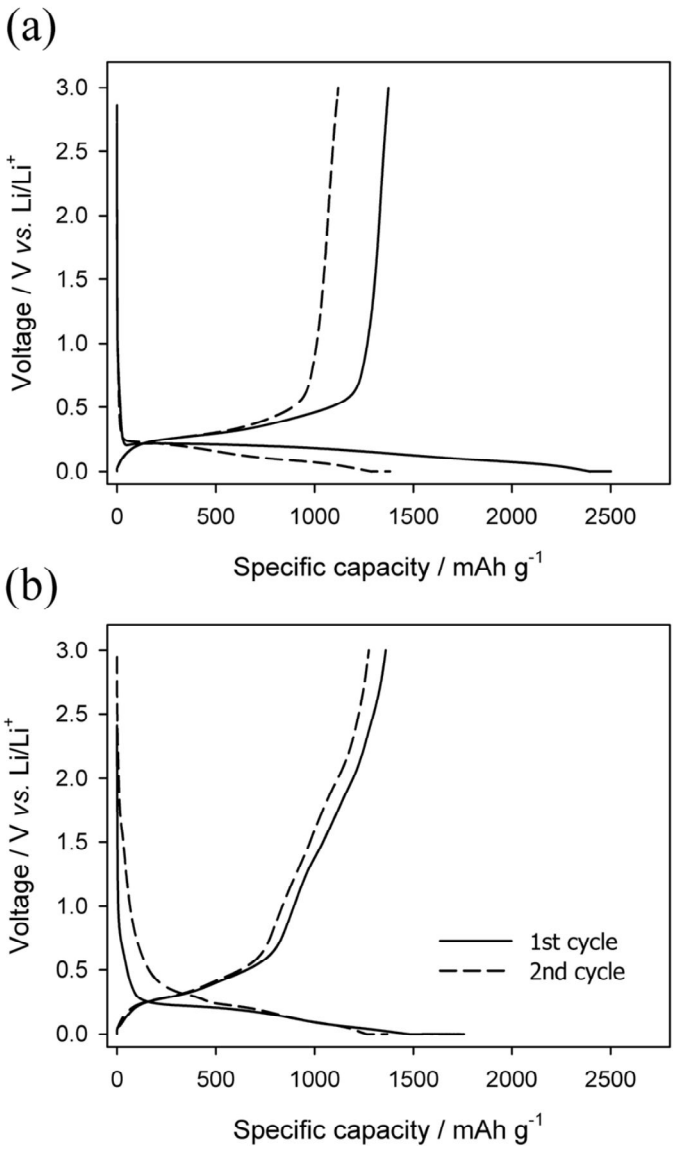


**Figure 50.** The first- and second- voltage – capacity profiles of (a) SiO (Sigma-Aldrich) and (b) a composite electrodes consisting of hand-mixed SiO and

**Table 10.** The first-cycle lithiation / de-lithiation capacity and the initial Coulombic efficiency of SiO, $Li_2MoO_3$, and a composite electrodes consisting of hand-mixed SiO and $Li_2MoO_3$.

| The first cycle | | Lithiation capacity ($mAh\ g^{-1}$) | De-lithiation capacity ($mAh\ g^{-1}$) | Coulombic efficiency (%) |
|---|---|---|---|---|
| SiO | | 2501 | 1374 | 54.9 |
| $Li_2MoO_3$ | | 955 | 1011 | 105.9 |
| $SiO + Li_2MoO_3$ (1:1 *wt.* ratio) | Calculated value | 1728 | 1193 | 69.0 |
| | Measured value | 1757 | 1360 | 77.4 |

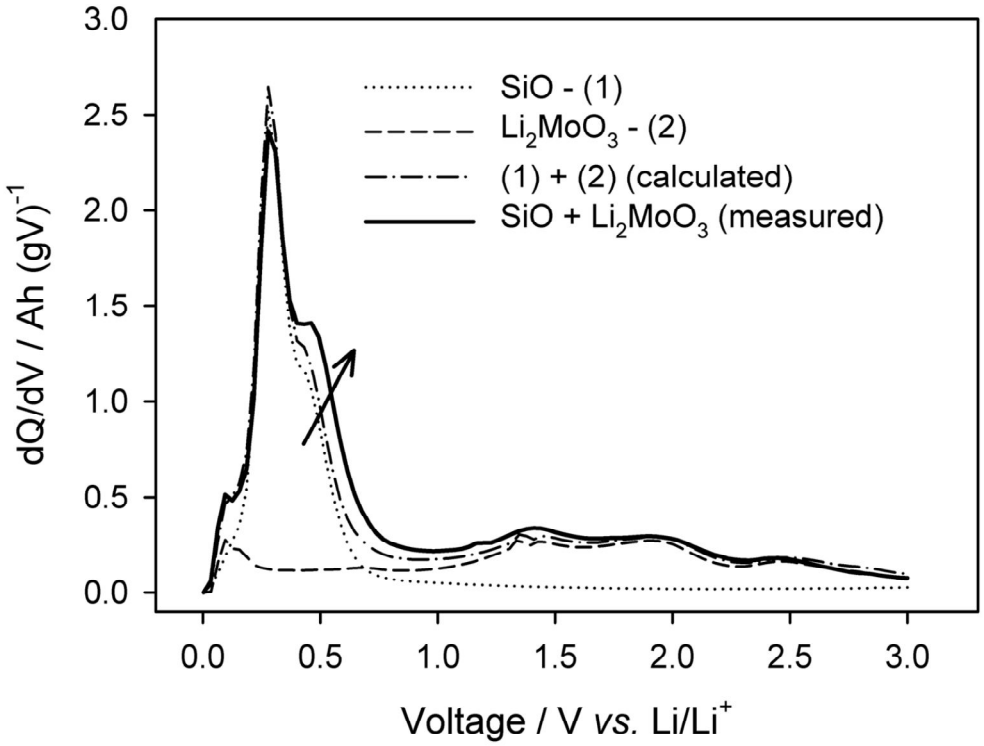


**Figure 51.** The first-cycle de-lithiation dQ/dV plots of SiO, $Li_2MoO_3$, and a composite electrodes consisting of hand-mixed SiO and $Li_2MoO_3$. Calculated plot is given by the average of SiO and $Li_2MoO_3$ plots.

# 5. CONCLUSIONS

In this work, the electrochemical performance of molybdenum oxides as negative electrode for lithium-ion batteries (LIBs) is improved by (i) *Chapter 4.1.*: pH control on the synthesis of amorphous molybdenum oxides, (ii) *Chapter 4.2.*: simple and short ball-milling of $MoO_3$, and (iii) *Chapter 4.3.*: a introduction of $Li_2MoO_3$ as new negative electrode for LIBs. Although conversion reaction-type metal oxides exhibit a high specific capacity than carbonaceous materials which is now used in practical LIBs, they have drawbacks including poor initial Coulombic efficiency (ICE). In this work, particularly in (ii) and (iii), the ICE of molybdenum oxides can be enhanced. The detail summaries are as follows.

(i) Amorphous molybdenum oxides can be synthesized by the reduction of aqueous $K_2MoO_4$ with aqueous $KBH_4$. According to the solution pH, physical properties of the oxides such as the Mo valence can be altered. Through TG and XANES analysis, each oxidation state of aM2-0.8 (amorphous $MoO_{2.2}$ prepared in low pH solution, pH=0.8) and aM2-4 (amorphous $MoO_{2.8}$ prepared in high pH solution,

pH=4) is revealed to be closed to $Mo^{+4}$ and $Mo^{+6}$, respectively. Both amorphous oxide electrodes show relatively high ICE than crystal $MoO_3$ electrode, because of the intrinsic higher reversibility of lithium ions insertion into / extraction from defect sites than conversion reaction of crystal metal oxide. However, among the amorphous oxides, there are the different reaction mechanism in the lithiation and de-lithiation and thus the electrochemical performance due to the different Mo valence. Specially, aM2-4 follows the conversion reaction, while aM2-0.8 do not, which results in poor cycle performance of aM2-4 and good cycle performance of aM2-0.8. Therefore, this study demonstrates that physical properties and ultimately the electrochemical performance of synthesized transition metal oxide can be altered by controlling such as the solution pH. Further research about transition metal oxides prepared by sol-gel method will elucidate the precise relationship between the synthetic conditions and physical properties of the oxides, which will directly aid the improvement of the performance of LIBs in the future.

(ii) By the analysis of conversion reaction of $MoO_3$ electrode, it is revealed that the de-lithiation reaction consists of two reaction: the additional de-lithiation capacity which is polymer/gel-like film dissolution in below 0.8 V (*vs.* $Li/Li^+$), and de-conversion reaction in voltage range of 0.8 ~ 3 V (*vs.* $Li/Li^+$). Among these reaction capacity, ball-milling of $MoO_3$ can increase the de-conversion reaction capacity by improving the reversibility of conversion reaction, or reactivity of de-conversion reaction, which results in the enhancement of electrochemical performance, especially

in ICE and cycleability. The reason is stemmed from the high reactivity of the grinded surfaces and tens of nanometric particles formed by ball-milling. Due to the extremely small size, molybdenum ions in them can oxidize up to almost +6 in the de-lithiation process, whereas not in molybdenum ions in micro-sized particles. However, such positive effects decrease in further ball-milling samples because of the practical problems in usage of water-soluble binder and aggregation of particles to reduce their surface energy. In summary, even ball-milling during short time with low rpm can enhance the ICE of $MoO_3$ electrode, and therefore, it is expected that such ball-milling can improve the electrochemical performance of other conversion-reaction based inorganic compounds.

(iii) To enhance the ICE of conversion reaction material, $Li_2O$ is added as a molecular-level mixture with $MoO_2$ by introducing $Li_2MoO_3$ material. When the $MoO_2$ component is lithiated by conversion reaction, the $Li_2O$ component is idling. In the de-lithiation, the idling $Li_2O$ now participates in the bond-forming reaction, releasing 6 $Li^+$/electrons per formula unit. Meanwhile, M valence is 4+ in $Li_2MoO_3$ but should be increased up to 6+ ($MoO_3$) to release 6 $Li^+$/electrons. Such further oxidation during the first-cycle de-lithiation is confirmed by electrochemically (comparison of the specific capacity, OCV before each cycle) and spectroscopically (comparison of valence change of metal ion and structural change by XANES and EXAFS). Consequently, the de-lithiation capacity is higher than the lithiation capacity to give the ICE of > 100 %. Moreover, it shows not only high specific capacity but also good cycle performance,

thus it can be good candidate for negative electrode material in LIBs.

# REFERENCES


[1] M. Winter, J. O. Besenhard, M. E. Spahr, P. Novák, *Advanced Materials*, **10** (1998) 725-763.

[2] J. M. Tarascon, M. Armand, *Nature*, **414** (2001) 359-367.

[3] T.-H. Kim, J.-S. Park, S. K. Chang, S. Choi, J. H. Ryu, H.-K. Song, *Advanced Energy Materials*, **2** (2012) 860-872.

[4] A. S. Arico, P. Bruce, B. Scrosati, J.-M. Tarascon, W. van Schalkwijk, *Nature Materials*, **4** (2005) 366-377.

[5] M. Armand, J.-M. Tarascon, *Nature*, **451** (2008) 652-657.

[6] J. Cabana, L. Monconduit, D. Larcher, M. R. Palacin, *Advanced Materials*, **22** (2010) E170-192.

[7] J. B. Goodenough, Y. Kim, *Chemistry of Materials*, **22** (2010) 587-603.

[8] M. V. Reddy, G. V. Subba Rao, B. V. R. Chowdari, *Chemical Reviews*, **113** (2013) 5364-5457.

[9] J. H. Ku, J. H. Ryu, S. H. Kim, O. H. Han, S. M. Oh, *Advanced Functional Materials*, **22** (2012) 3658-3664.

[10] 오승모, *전기화학*, 2 ed. 자유아카데미 (2014).

[11] M. S. Whittingham, *Science*, **192** (1976) 1126-1127.

[12] M. S. Whittingham, *Chemical Reviews*, **104** (2004) 4271-4302.

[13] P. Kurzweil, K. Brandt, in *Encyclopedia of Electrochemical Power Sources* (Ed.: J. Garche), Elsevier, Amsterdam (2009), pp. 1-26.

[14] M. Armand, P. Touzain, *Materials Science and Engineering*, **31** (1977) 319-329.

[15] K. Mizushima, P. C. Jones, P. J. Wiseman, J. B. Goodenough, *Materials Research Bulletin*, **15** (1980) 783-789.

[16] M. G. S. R. Thomas, P. G. Bruce, J. B. Goodenough, *Journal of The Electrochemical Society*, **132** (1985) 1521-1528.

[17] K. Xu, *Chemical Reviews*, **104** (2004) 4303-4418.
[18] J. N. Reimers, J. R. Dahn, *Journal of The Electrochemical Society*, **139** (1992) 2091-2097.
[19] J. Cho, Y. J. Kim, T.-J. Kim, B. Park, *Angewandte Chemie International Edition*, **40** (2001) 3367-3369.
[20] R. A. Leising, M. J. Palazzo, E. S. Takeuchi, K. J. Takeuchi, *Journal of The Electrochemical Society*, **148** (2001) A838-A844.
[21] K.-S. Lee, Y.-K. Sun, J. Noh, K. S. Song, D.-W. Kim, *Electrochemistry Communications*, **11** (2009) 1900-1903.
[22] T. Ohzuku, A. Ueda, M. Nagayama, *Journal of The Electrochemical Society*, **140** (1993) 1862-1870.
[23] T. Ohzuku, A. Ueda, M. Nagayama, Y. Iwakoshi, H. Komori, *Electrochimica Acta*, **38** (1993) 1159-1167.
[24] S. H. Kang, J. Kim, M. E. Stoll, D. Abraham, Y. K. Sun, K. Amine, *Journal of Power Sources*, **112** (2002) 41-48.
[25] C. H. Chen, J. Liu, M. E. Stoll, G. Henriksen, D. R. Vissers, K. Amine, *Journal of Power Sources*, **128** (2004) 278-285.
[26] Z. Liu, A. Yu, J. Y. Lee, *Journal of Power Sources*, **81–82** (1999) 416-419.
[27] M. Yoshio, H. Noguchi, J.-i. Itoh, M. Okada, T. Mouri, *Journal of Power Sources*, **90** (2000) 176-181.
[28] M. M. Thackeray, W. I. F. David, P. G. Bruce, J. B. Goodenough, *Materials Research Bulletin*, **18** (1983) 461-472.
[29] M. M. Thackeray, P. J. Johnson, L. A. de Picciotto, P. G. Bruce, J. B. Goodenough, *Materials Research Bulletin*, **19** (1984) 179-187.
[30] R. J. Gummow, A. de Kock, M. M. Thackeray, *Solid State Ionics*, **69** (1994) 59-67.
[31] D. H. Jang, S. M. Oh, *Journal of The Electrochemical Society*, **144** (1997) 3342-3348.
[32] K. Amine, H. Tukamoto, H. Yasuda, Y. Fujita, *Journal of The Electrochemical Society*, **143** (1996) 1607-1613.
[33] P. Arora, B. N. Popov, R. E. White, *Journal of The Electrochemical Society*, **145** (1998) 807-815.
[34] A. M. Kannan, A. Manthiram, *Electrochemical and Solid-State Letters*, **5** (2002) A167-A169.
[35] S.-W. Lee, K.-S. Kim, H.-S. Moon, H.-J. Kim, B.-W. Cho, W.-I. Cho, J.-B. Ju, J.-W. Park, *Journal of Power Sources*, **126** (2004) 150-155.
[36] Y. Talyosef, B. Markovsky, G. Salitra, D. Aurbach, H. J. Kim, S. Choi, *Journal of Power Sources*, **146** (2005) 664-669.
[37] T. Yoon, D. Kim, K. H. Park, H. Park, S. Jurng, J. Jang, J. H. Ryu, J. J. Kim, S. M. Oh, *Journal of The Electrochemical Society*, **161** (2014) A519-A523.
[38] A. K. Padhi, K. S. Nanjundaswamy, J. B. Goodenough, *Journal of The Electrochemical Society*, **144** (1997) 1188-1194.
[39] A. Yamada, S. C. Chung, K. Hinokuma *Journal of The Electrochemical*

*Society*, **148** (2001) A224-A229.
[40] D. Morgan, A. Van der Ven, G. Ceder, *Electrochemical and Solid-State Letters*, **7** (2004) A30-A32.
[41] P. S. Herle, B. Ellis, N. Coombs, L. F. Nazar, *Nature Materials*, **3** (2004) 147-152.
[42] B. Kang, G. Ceder, *Nature*, **458** (2009) 190-193.
[43] S.-Y. Chung, J. T. Bloking, Y.-M. Chiang, *Nature Materials*, **1** (2002) 123-128.
[44] M. Rosso, T. Gobron, C. Brissot, J.-N. Chazalviel, S. Lascaud, *Journal of Power Sources*, **97-98** (2001) 804-806.
[45] P. C. Howlett, D. R. MacFarlane, A. F. Hollenkamp, *Journal of Power Sources*, **114** (2003) 277-284.
[46] W.-S. Kim, W.-Y. Yoon, *Electrochimica Acta*, **50** (2004) 541-545.
[47] L. Gireaud, S. Grugeon, S. Laruelle, B. Yrieix, J.-M. Tarascon, *Electrochemistry Communications*, **8** (2006) 1639-1649.
[48] M. Ishikawa, H. Kawasaki, N. Yoshimoto, M. Morita, *Journal of Power Sources*, **146** (2005) 199-203.
[49] S.-K. Jeong, H.-Y. Seo, D.-H. Kim, H.-K. Han, J.-G. Kim, Y. B. Lee, Y. Iriyama, T. Abe, Z. Ogumi, *Electrochemistry Communications*, **10** (2008) 635-638.
[50] S. Liu, N. Imanishi, T. Zhang, A. Hirano, Y. Takeda, O. Yamamoto, J. Yang, *Journal of Power Sources*, **195** (2010) 6847-6853.
[51] N.-S. Choi, B. Koo, J.-T. Yeon, K. T. Lee, D.-W. Kim, *Electrochimica Acta*, **56** (2011) 7249-7255.
[52] M. Wu, Z. Wen, Y. Liu, X. Wang, L. Huang, *Journal of Power Sources*, **196** (2011) 8091-8097.
[53] D. Guerard, A. Herold, *Carbon*, **13** (1975) 337-345.
[54] J. O. Besenhard, H. P. Fritz, *Angewandte Chemie International Edition in English*, **22** (1983) 950-975.
[55] J. R. Dahn, A. K. Sleigh, H. Shi, J. N. Reimers, Q. Zhong, B. M. Way, *Electrochimica Acta*, **38** (1993) 1179-1191.
[56] J. R. Dahn, W. Xing, Y. Gao, *Carbon*, **35** (1997) 825-830.
[57] C. Wan Park, S.-H. Yoon, S. I. Lee, S. M. Oh, *Carbon*, **38** (2000) 995-1001.
[58] A. N. Dey, *Journal of The Electrochemical Society*, **118** (1971) 1547-1549.
[59] R. A. Huggins, *Journal of Power Sources*, **81–82** (1999) 13-19.
[60] J. Y. Kwon, J. H. Ryu, S. M. Oh, *Electrochimica Acta*, **55** (2010) 8051-8055.
[61] M. Winter, J. O. Besenhard, *Electrochimica Acta*, **45** (1999) 31-50.
[62] H. Mukaibo, T. Osaka, P. Reale, S. Panero, B. Scrosati, M. Wachtler, *Journal of Power Sources*, **132** (2004) 225-228.
[63] P. G. Bruce, B. Scrosati, J.-M. Tarascon, *Angewandte Chemie International Edition*, **47** (2008) 2930-2946.
[64] C. K. Chan, H. Peng, G. Liu, K. McIlwrath, X. F. Zhang, R. A. Huggins, Y. Cui, *Nat Nano*, **3** (2008) 31-35.
[65] W.-J. Zhang, *Journal of Power Sources*, **196** (2011) 13-24.

[66] K. D. Kepler, J. T. Vaughey, M. M. Thackeray, *Journal of Power Sources*, **81–82** (1999) 383-387.
[67] J. Y. Kwon, J. H. Ryu, Y. S. Jung, S. M. Oh, *Journal of Alloys and Compounds*, **509** (2011) 7595-7599.
[68] M. Wachtler, J. O. Besenhard, M. Winter, *Journal of Power Sources*, **94** (2001) 189-193.
[69] J. Li, R. B. Lewis, J. R. Dahn, *Electrochemical and Solid-State Letters*, **10** (2007) A17-A20.
[70] N. S. Hochgatterer, M. R. Schweiger, S. Koller, P. R. Raimann, T. Wöhrle, C. Wurm, M. Winter, *Electrochemical and Solid-State Letters*, **11** (2008) A76-A80.
[71] M.-Q. Li, M.-Z. Qu, X.-Y. He, Z.-L. Yu, *Electrochimica Acta*, **54** (2009) 4506-4513.
[72] G.-B. Han, M.-H. Ryou, K. Y. Cho, Y. M. Lee, J.-K. Park, *Journal of Power Sources*, **195** (2010) 3709-3714.
[73] K. M. Colbow, J. R. Dahn, R. R. Haering, *Journal of Power Sources*, **26** (1989) 397-402.
[74] T.-F. Yi, L.-J. Jiang, J. Shu, C.-B. Yue, R.-S. Zhu, H.-B. Qiao, *Journal of Physics and Chemistry of Solids*, **71** (2010) 1236-1242.
[75] K. Zaghib, M. Simoneau, M. Armand, M. Gauthier, *Journal of Power Sources*, **81–82** (1999) 300-305.
[76] C. H. Chen, J. T. Vaughey, A. N. Jansen, D. W. Dees, A. J. Kahaian, T. Goacher, M. M. Thackeray, *Journal of The Electrochemical Society*, **148** (2001) A102-A104.
[77] E. M. Sorensen, S. J. Barry, H.-K. Jung, J. M. Rondinelli, J. T. Vaughey, K. R. Poeppelmeier, *Chemistry of Materials*, **18** (2005) 482-489.
[78] L. Zhao, Y.-S. Hu, H. Li, Z. Wang, L. Chen, *Advanced Materials*, **23** (2011) 1385-1388.
[79] A. R. Armstrong, G. Armstrong, J. Canales, R. García, P. G. Bruce, *Advanced Materials*, **17** (2005) 862-865.
[80] L. Liu, Q. Fan, C. Sun, X. Gu, H. Li, F. Gao, Y. Chen, L. Dong, *Journal of Power Sources*, **221** (2013) 141-148.
[81] J. H. Ku, Y. S. Jung, K. T. Lee, C. H. Kim, S. M. Oh, *Journal of The Electrochemical Society*, **156** (2009) A688-A693.
[82] S. Yoon, K.-N. Jung, C. S. Jin, K.-H. Shin, *Journal of Alloys and Compounds*, **536** (2012) 179-183.
[83] H.-J. Zhang, T.-H. Wu, K.-X. Wang, X.-Y. Wu, X.-T. Chen, Y.-M. Jiang, X. Wei, J.-S. Chen, *Journal of Materials Chemistry A*, **1** (2013) 12038-12043.
[84] A.-M. Cao, J.-S. Hu, H.-P. Liang, L.-J. Wan, *Angewandte Chemie International Edition*, **44** (2005) 4391-4395.
[85] O. B. Chae, J. Kim, I. Park, H. Jeong, J. H. Ku, J. H. Ryu, K. Kang, S. M. Oh, *Chemistry of Materials*, **26** (2014) 5874-5881.

[86] P. Poizot, S. Laruelle, S. Grugeon, L. Dupont, J. M. Tarascon, *Nature*, **407** (2000) 496-499.
[87] D. Larcher, G. Sudant, J.-B. Leriche, Y. Chabre, J.-M. Tarascon, *Journal of The Electrochemical Society*, **149** (2002) A234-A241.
[88] S. Sun, H. Zeng, *Journal of the American Chemical Society*, **124** (2002) 8204-8205.
[89] Y.-M. Kang, K.-T. Kim, K.-Y. Lee, S.-J. Lee, J.-H. Jung, J.-Y. Lee, *Journal of The Electrochemical Society*, **150** (2003) A1538-A1543.
[90] D. Larcher, C. Masquelier, D. Bonnin, Y. Chabre, V. Masson, J.-B. Leriche, J.-M. Tarascon, *Journal of The Electrochemical Society*, **150** (2003) A133-A139.
[91] P. Poizot, S. Laruelle, S. Grugeon, J.-M. Tarascon, *Journal of The Electrochemical Society*, **149** (2002) A1212.
[92] H. Li, P. Balaya, J. Maier, *Journal of The Electrochemical Society*, **151** (2004) A1878-A1885.
[93] S. Laruelle, S. Grugeon, P. Poizot, M. Dollé, L. Dupont, J. M. Tarascon, *Journal of The Electrochemical Society*, **149** (2002) A627.
[94] Y.-Y. Hu, Z. Liu, K.-W. Nam, O. J. Borkiewicz, J. Cheng, X. Hua, M. T. Dunstan, X. Yu, K. M. Wiaderek, L.-S. Du, K. W. Chapman, P. J. Chupas, X.-Q. Yang, C. P. Grey, *Nature Materials*, **12** (2013) 1130-1136.
[95] P. Balaya, H. Li, L. Kienle, J. Maier, *Advanced Functional Materials*, **13** (2003) 621-625.
[96] J. Jamnik, J. Maier, *Physical Chemistry Chemical Physics*, **5** (2003) 5215.
[97] Y. F. Zhukovskii, P. Balaya, E. A. Kotomin, J. Maier, *Physical Review Letters*, **96** (2006) 058302.
[98] A. Ponrouch, P.-L. Taberna, P. Simon, M. R. Palacín, *Electrochimica Acta*, **61** (2012) 13-18.
[99] V. Aravindan, J. Gnanaraj, S. Madhavi, H.-K. Liu, *Chemistry – A European Journal*, **17** (2011) 14326-14346.
[100] W. Henderson, in *Electrolytes for Lithium and Lithium-Ion Batteries, Vol.* **58** (Eds.: T. R. Jow, K. Xu, O. Borodin, M. Ue), Springer New York (2014), pp. 1-92.
[101] S. S. Zhang, K. Xu, T. R. Jow, *Journal of The Electrochemical Society*, **149** (2002) A586-A590.
[102] K. Kanamura, *Journal of Power Sources*, **81–82** (1999) 123-129.
[103] Y. Sasaki, M. Handa, K. Kurashima, T. Tonuma, K. Usami, *Journal of The Electrochemical Society*, **148** (2001) A999-A1003.
[104] R. Fong, U. von Sacken, J. R. Dahn, *Journal of The Electrochemical Society*, **137** (1990) 2009-2013.
[105] D. Guyomard, J. M. Tarascon, *Journal of The Electrochemical Society*, **140** (1993) 3071-3081.
[106] J. M. Tarascon, D. Guyomard, *Solid State Ionics*, **69** (1994) 293-305.
[107] E. Peled, *Journal of The Electrochemical Society*, **126** (1979) 2047-2051.
[108] D. Aurbach, Y. Ein-Eli, O. Chusid , Y. Carmeli, M. Babai, H. Yamin, *Journal*

*of The Electrochemical Society*, **141** (1994) 603-611.
[109] G. Nagasubramanian, S. Di Stefano, *Journal of The Electrochemical Society*, **137** (1990) 3830-3835.
[110] M. C. Lonergan, M. A. Ratner, D. F. Shriver, *Journal of the American Chemical Society*, **117** (1995) 2344-2350.
[111] D. Aurbach, K. Gamolsky, B. Markovsky, Y. Gofer, M. Schmidt, U. Heider, *Electrochimica Acta*, **47** (2002) 1423-1439.
[112] M. Contestabile, M. Morselli, R. Paraventi, R. J. Neat, *Journal of Power Sources*, **119–121** (2003) 943-947.
[113] K. M. Abraham, D. M. Pasquariello, E. B. Willstaedt, *Journal of The Electrochemical Society*, **137** (1990) 1856-1857.
[114] K. Abe, in *Electrolytes for Lithium and Lithium-Ion Batteries, Vol.* **58** (Eds.: T. R. Jow, K. Xu, O. Borodin, M. Ue), Springer New York (2014), pp. 167-207.
[115] J. Kang, F. Yan, P. Zhang, C. Du, *Journal of Power Sources*, **206** (2012) 310-314.
[116] J. H. Ryu, J. W. Kim, Y.-E. Sung, S. M. Oh, *Electrochemical and Solid-State Letters*, **7** (2004) A306-A309.
[117] D. Kim, S. Park, O. B. Chae, J. H. Ryu, Y.-U. Kim, R.-Z. Yin, S. M. Oh, *Journal of The Electrochemical Society*, **159** (2012) A193-A197.
[118] A. Manthiram, C. Tsang, *Journal of The Electrochemical Society*, **143** (1996) L143-L145.
[119] K.-S. Park, D. Im, A. Benayad, A. Dylla, K. J. Stevenson, J. B. Goodenough, *Chemistry of Materials*, **24** (2012) 2673-2683.
[120] M. Sathiya, K. Ramesha, G. Rousse, D. Foix, D. Gonbeau, A. S. Prakash, M. L. Doublet, K. Hemalatha, J. M. Tarascon, *Chemistry of Materials*, **25** (2013) 1121-1131.
[121] J. R. Dahn, T. Zheng, Y. Liu, J. S. Xue, *Science*, **270** (1995) 590-593.
[122] J. R. Dahn, W. R. McKinnon, *Solid State Ionics*, **23** (1987) 1-7.
[123] L. C. Yang, Q. S. Gao, Y. H. Zhang, Y. Tang, Y. P. Wu, *Electrochemistry Communications*, **10** (2008) 118-122.
[124] N. A. Chernova, M. Roppolo, A. C. Dillon, M. S. Whittingham, *Journal of Materials Chemistry*, **19** (2009) 2526-2552.
[125] O. B. Chae, S. Park, J. H. Ryu, S. M. Oh, *Journal of The Electrochemical Society*, **160** (2012) A11-A14.
[126] S.-H. Lee, Y.-H. Kim, R. Deshpande, P. A. Parilla, E. Whitney, D. T. Gillaspie, K. M. Jones, A. H. Mahan, S. Zhang, A. C. Dillon, *Advanced Materials*, **20** (2008) 3627-3632.
[127] Y. S. Jung, S. Lee, D. Ahn, A. C. Dillon, S.-H. Lee, *Journal of Power Sources*, **188** (2009) 286-291.
[128] M. F. Hassan, Z. P. Guo, Z. Chen, H. K. Liu, *Journal of Power Sources*, **195** (2010) 2372-2376.
[129] L. A. Riley, S.-H. Lee, L. Gedvilias, A. C. Dillon, *Journal of Power Sources*,

**195** (2010) 588-592.
[130] B. d. Darwent, *National Standard Reference Data Series: National Bureau of Standard No. 31, Washington* (1970.
[131] W. J. H. Borghols, M. Wagemaker, U. Lafont, E. M. Kelder, F. M. Mulder, *Journal of the American Chemical Society*, **131** (2009) 17786-17792.
[132] J. Yang, T. B. Atwater, J. J. Xu, *Journal of Power Sources*, **139** (2005) 274-278.
[133] A. Martínez-de la Cruz, I. Juárez Ramírez, *Journal of Power Sources*, **133** (2004) 268-271.
[134] Y. Shi, B. Guo, S. A. Corr, Q. Shi, Y.-S. Hu, K. R. Heier, L. Chen, R. Seshadri, G. D. Stucky, *Nano Letters*, **9** (2009) 4215-4220.
[135] K. Ben-Kamel, N. Amdouni, H. Groult, A. Mauger, K. Zaghib, C. M. Julien, *Journal of Power Sources*, **202** (2012) 314-321.
[136] W. Cho, J. Song, J.-H. Kim, G. Jeong, E. Lee, Y.-J. Kim, *Journal of Applied Electrochemistry*, **42** (2012) 909-915.
[137] A. Bhaskar, M. Deepa, T. Narasinga Rao, *ACS Applied Materials & Interfaces* 2013.
[138] J. Park, I. Choi, M. J. Lee, M. H. Kim, T. Lim, K. H. Park, J. Jang, S. M. Oh, S. K. Cho, J. J. Kim, *Electrochimica Acta*, **132** (2014) 338-346.
[139] A. N. Mansour, P. H. Smith, W. M. Baker, M. Balasubramanian, J. McBreen, *Electrochimica Acta*, **47** (2002) 3151-3161.
[140] C. Tsang, A. Dananjay, J. Kim, A. Manthiram, *Inorganic Chemistry*, **35** (1996) 504-509.
[141] E. Bekaert, P. Balaya, S. Murugavel, J. Maier, M. Ménétrier, *Chemistry of Materials*, **21** (2009) 856-861.
[142] A. Débart, L. Dupont, P. Poizot, J.-B. Leriche, J. M. Tarascon *Journal of The Electrochemical Society*, **148** (2001) A1266-A1274.
[143] S. Grugeon, S. Laruelle, R. Herrera-Urbina, L. Dupont, P. Poizot, J.-M. Tarascon, *Journal of The Electrochemical Society*, **148** (2001) A285-A292.
[144] T. A. Kerr, H. Wu, L. F. Nazar, *Chemistry of Materials*, **8** (1996) 2005-2015.
[145] C. H. Kim, Y. S. Jung, K. T. Lee, J. H. Ku, S. M. Oh, *Electrochimica Acta*, **54** (2009) 4371-4377.
[146] N. S. Chiu, S. H. Bauer, M. F. L. Johnson, *Journal of Catalysis*, **89** (1984) 226-243.
[147] D. Lützenkirchen-Hecht, R. Frahm, *The Journal of Physical Chemistry B*, **105** (2001) 9988-9993.
[148] K. Isa, H. Ishimura, *Bulletin of the Chemical Society of Japan*, **54** (1981) 3628-3634.
[149] T. Ressler, *Journal of Catalysis*, **191** (2000) 75-85.
[150] O. Delmer, P. Balaya, L. Kienle, J. Maier, *Advanced Materials*, **20** (2008) 501-505.
[151] Y.-G. Guo, J.-S. Hu, L.-J. Wan, *Advanced Materials*, **20** (2008) 2878-2887.
[152] D. B. Rogers, R. D. Shannon, A. W. Sleight, J. L. Gillson, *Inorganic Chemistry*, **8** (1969) 841-849.

[153] Z. Hu, C. Zhou, M. Zheng, J. Lu, B. Varghese, H. Cheng, C.-H. Sow, *The Journal of Physical Chemistry C*, **116** (2012) 3962-3967.
[154] F. Disma, L. Aymard, L. Dupont, J. M. Tarascon, *Journal of The Electrochemical Society*, **143** (1996) 3959-3972.
[155] B. Koo, H. Kim, Y. Cho, K. T. Lee, N.-S. Choi, J. Cho, *Angewandte Chemie International Edition*, **51** (2012) 8762-8767.
[156] L. Su, Y. Zhong, Z. Zhou, *Journal of Materials Chemistry A*, **1** (2013) 15158-15166.
[157] J. Maier, *Angewandte Chemie International Edition*, **52** (2013) 4998-5026.
[158] Y. S. Jung, P. Lu, A. S. Cavanagh, C. Ban, G.-H. Kim, S.-H. Lee, S. M. George, S. J. Harris, A. C. Dillon, *Advanced Energy Materials*, **3** (2013) 213-219.
[159] Y. Qiao, X. Hu, Y. Liu, G. Liang, M. C. Croft, Y. Huang, *Journal of Materials Chemistry A*, **1** (2013) 15128-15134.
[160] O. B. Chae, S. Park, J. H. Ku, J. H. Ryu, S. M. Oh, *Electrochimica Acta*, **55** (2010) 2894-2900.
[161] J. Kim, M. K. Chung, B. H. Ka, J. H. Ku, S. Park, J. Ryu, S. M. Oh, *Journal of The Electrochemical Society*, **157** (2010) A412-A417.
[162] Y. Yu, C. H. Chen, J. L. Shui, S. Xie, *Angewandte Chemie International Edition*, **44** (2005) 7085-7089.
[163] S. J. Hibble, I. D. Fawcett, *Inorganic Chemistry*, **34** (1995) 500-508.
[164] B. J. Hornstein, D. M. Dattelbaum, J. R. Schoonover, T. J. Meyer, *Inorganic Chemistry*, **46** (2007) 8139-8145.

# 6. APPENDIX

## 6.1. Additional lithiation and de-lithiation capacity

Unlike ordinary negative electrode, metal oxide reacted through the conversion reaction shows unusual behavior near low voltage range, below 1 V (*vs.* $Li/Li^+$). In this chapter, such behavior in the first cycle are examined on the $MoO_3$ electrode. As mentioned in *Chapter 4.2.*, lithiation capacity of $MoO_3$ electrode is about 300 mAh $g^{-1}$ higher than the theoretical capacity, and we can call it as an *additional lithiation capacity*. In addition, during de-lithiation up to 0.8 V (*vs.* $Li/Li^+$), about 200 mAh $g^{-1}$ is exhibited without the oxidation of molybdenum metal, as demonstrated in *ex-situ* XANES spectra of $MoO_3$ electrode (Fig. 15). Thus, we called such capacity as an *additional de-lithiation capacity*. In *Chapter 4.2.*, we mentioned that the additional de-lithiation capacity is stemmed from the reversible polymer/gel-like film formation and dissolution, suggested by Tarascon group.[93] Similarly with previous studies, such additional lithiation / de-lithiation capacity is also examined in this study.

Cyclic voltammetry (CV) experimental was conducted to demonstrate the reaction

in low voltage region. After the first-cycle lithiation by constant current (CC) method, CV test was conducted on the voltage range of 0.8 ~ 0 V (*vs.* $Li/Li^+$). Fig. 52 shows CV data with various scan rate (mV $s^{-1}$). Note that almost of voltammograms show rectangular-like shape, and peak currents show linear relationship with scan rates rather than scan rates square of 1/2 (Fig. 53), which means capacitive behavior. There are two categories for capacitive behavior: (i) electric double-layer capacitive behavior, and (ii) pseudo-capacitive behavior.

Electric double-layer capacitor (EDLC) stores charges on the electric double-layer. EDLC is mostly used electrode having ideally polarizable characteristics, high electric conductivity, and large surface area such as activated carbon. EDLC-like behavior in the lithiated electrode by conversion reaction can be shown at the interface between nano-sized metallic particle and $Li_2O$ matrix. Electrons and lithium ions can be reserved in the metallic particles and lithium compounds ($Li_2O$), respectively. Such behavior has been called as a capacitive interfacial storage, and it is strongly suggested in Maier group.[96] In this study, capacity from the capacitive interfacial storage was calculated by using simple mathematics with some assumption. We assume that metallic particles are spheres, its average diameter and double-layer capacitance is 5 nm, and 30 μF $cm^{-2}$, respectively.[98] As shown in Table.11, the result capacity is much smaller than measured capacity during lithiation and de-lithiation. In fact, double-layer capacitance used in this calculation is that of bulk metal, and thus that of nano-sized metallic particle could be much higher than that of bulk metal. Nonetheless, since such

c a l c u l a t e d  c a p a c i t y  i s

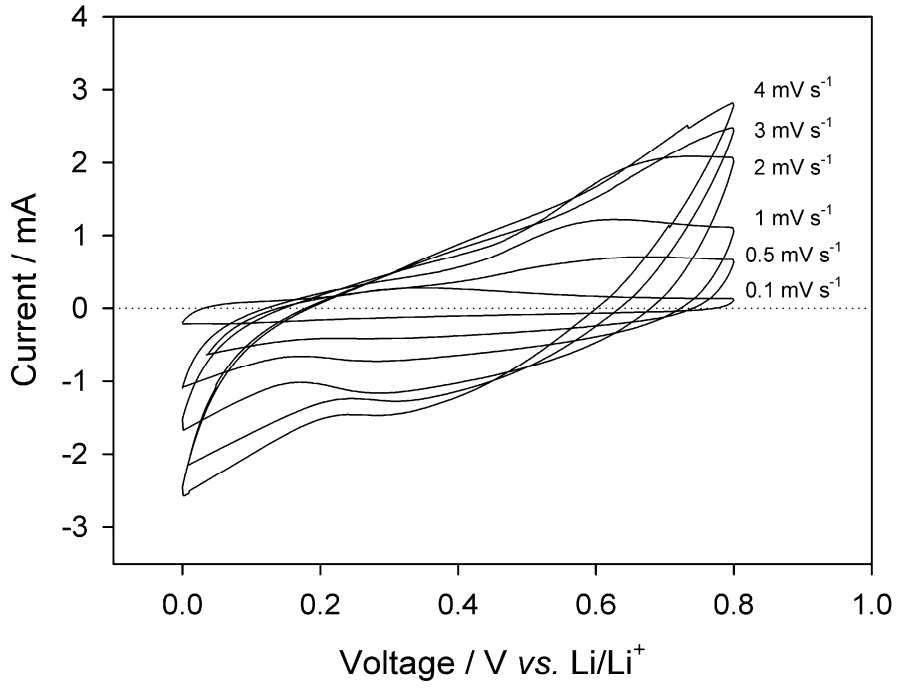


**Figure 52.** CV test for lithiated $MoO_3$ electrode over the voltage range of 0 ~ 0.8 V (*vs.* $Li/Li^+$) with various scan rate (0.1, 0.5, 1, 2, 3, and 4 mV $s^{-1}$).

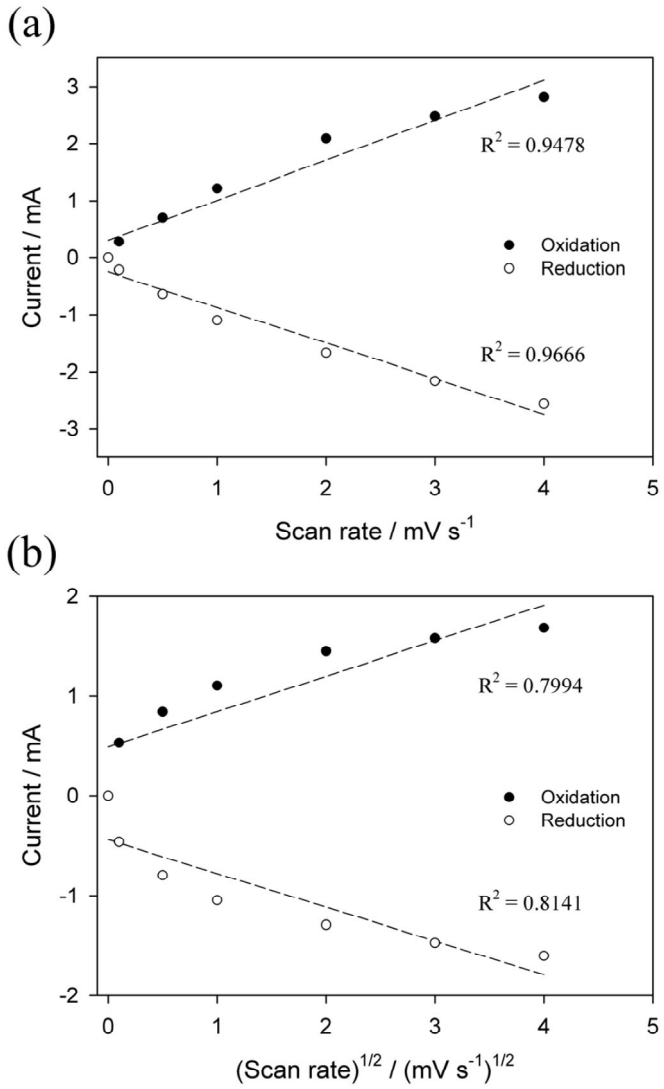


**Figure 53.** Peak, or maximum, current in CV test for oxidation (black dot) and reduction (white dot) *vs.* (a) (scan rate) $^{1}$ and (b) (scan rate) $^{1/2}$. Note that higher $R^2$ value in (a) than (b).

**Table 11.** Calculated additional capacity based on EDLC of nano-sized metallic particles, and measured additional capacity in the conversion reaction of $MoO_3$ electrode.

| | Voltage range (V, *vs.* $Li/Li^+$) | Calculated additional capacity ($mAh\ g^{-1}$) | Measured additional capacity ($mAh\ g^{-1}$) |
|---|---|---|---|
| Lithiation | 0.5 ~ 0 | 4.2 | ~ 300 |
| De-lithiation | 0 ~ 0.8 | 6.7 | ~ 200 |

extremely small, there should be another reaction showing capacitive behavior.

Pseudo-capacitor stores charges by faradaic reaction rather than using ideally polarizable characteristics of electrode, but it is called pseudo-capacitor because it shows similar behavior with EDLC. Mostly pseudo-capacitive reaction occurs in the immobilized redox species at the surface of electrode. There are some examples: redox reaction of functional groups such as OH group, reaction of $RuO_2$ with proton ($H^+$) in the aqueous solution, redox reaction of organic conducting polymer. In lithiated metal oxide electrode by conversion reaction, however, such reaction cannot occur because of organic electrolyte, extreme low voltage region, below 0.8 V (*vs.* $Li/Li^+$), in which OH group cannot survive. Therefore, another species who can exhibit pseudo-capacitive behavior must be presented in the lithiated metal oxide electrode. Electrolyte or some organic species in the SEI film can be a good candidate. Reversible polymer/gel-like film formation and dissolution, suggested by Tarascon group and mentioned in *Chapter 4.2.*, means the faradaic reaction of organic electrolyte exhibiting pseudo-capacitive behavior. As seen in *ex-situ* TEM images (Fig. 54), lithiated $MoO_3$ particles by conversion reaction has very thick film at the surface of $MoO_3$. It is much thicker than SEI film in ordinary negative electrode, because nano-sized metallic particles formed by conversion reaction maybe act as a catalyst to decompose organic electrolyte. Therefore, such thick film is called as polymer/gel-like film rather than dense SEI. To demonstrate film change during cycling on the surface of metallic particles, molybdenum metal powder having around 100 nm size embedded

in a Ni form is cycled and *ex-situ* XPS for

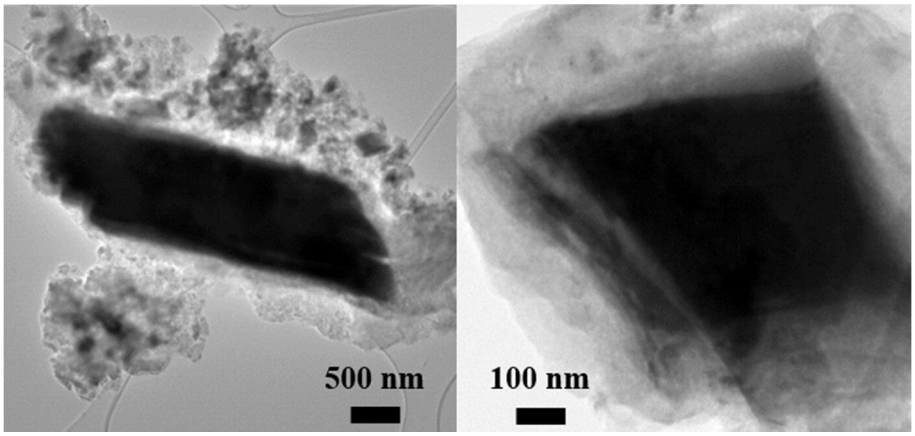


**Figure 54.** *Ex-situ* TEM images for lithiated $MoO_3$ particles. Dense and black particles are $MoO_3$ particles lithiated by conversion reaction ($Mo^0 + Li_2O$), and porous and gray films at the surface of particles are passivation films formed by electrolyte decomposition.

lithiated and de-lithiated was examined. After de-lithiation (3 V), XPS peak from molybdenum metal shows more clearly than after lithiation (0 V), which means the thickness of film is varied reversibly during cycling (Fig. 55a). In addition, through the XPS for carbon 1s, it is revealed that organic species are dominantly formed and removed during cycling (Fig. 55b). Even though it cannot be confirmed that such reversible polymer/gel-like film formation and dissolution reaction is the main source in additional lithiation / de-lithiation capacity, we can demonstrate that organic species are formed and removed reversibly during cycling.

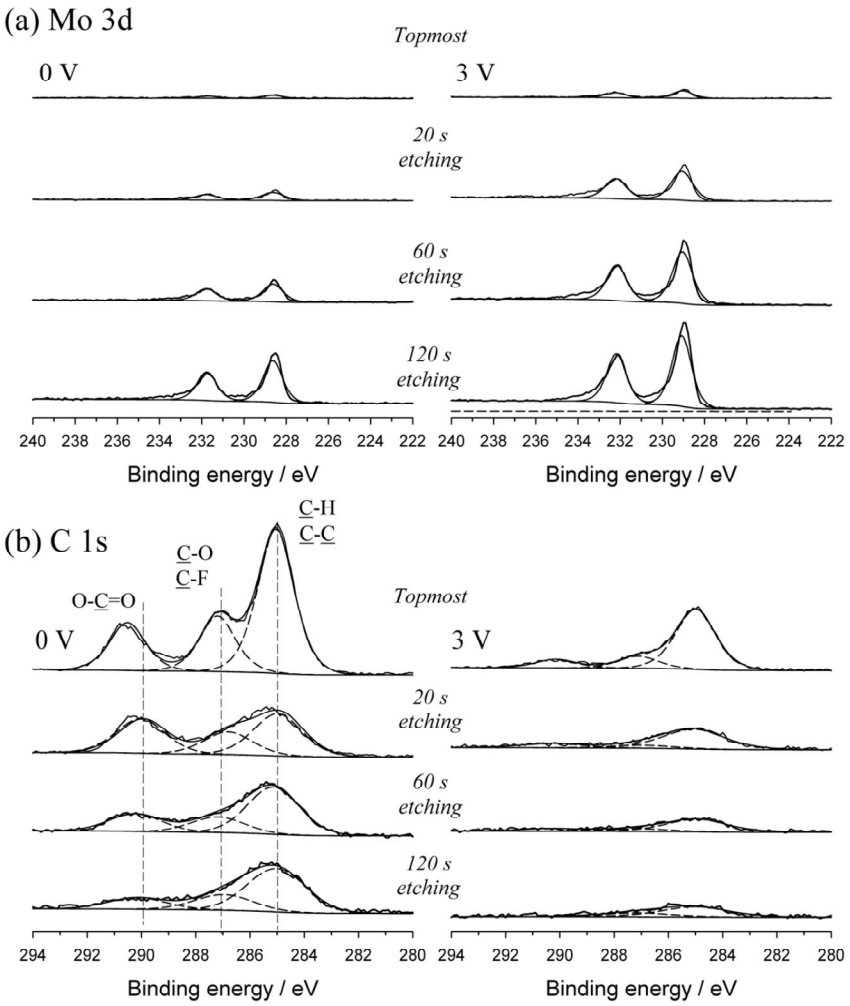


**Figure 55.** (a) Mo 3d, (b) C 1s XPS spectra of lithiated (0 V) and de-lithiated (3 V) molybdenum metal (~ 100 nm) embedded in Ni form.

# 국문초록

## 리튬 이온 전지용 몰리브데넘 산화물 전극의 초기 쿨롱 효율 향상

장 지 현
서울대학교 대학원
화학생물공학부

현재 상용화된 리튬 이온 전지의 음극 물질인 흑연은 많은 장점이 있지만, 작은 용량 때문에 전기자동차나 대용량 저장 장치 등 큰 용량을 필요로 하는 전지에 적용하기에는 한계점이 있다. 이를 극복하기 위해 개발되고 있는 음극소재 중, 전환 반응을 통해 용량을 발현하는 금속 산화물이 큰 용량을 발현한다는 장점으로 인해 차세대 음극물질로 각광받고

있다. 이러한 금속 산화물은 충전 시에 금속 이온이 전자를 받으면서 금속과 산소 사이의 결합이 깨져 금속 이온은 메탈 상태까지 환원이 되고 산소 이온은 리튬 이온과 결합해 $Li_2O$ 를 형성하게 된다. 방전 시에는 산화 반응을 통해 금속과 산소 사이의 결합이 다시 생기면서 리튬 이온이 빠져나와 용량을 발현한다.

여러 가지 금속 산화물 중 몰리브데넘 산화물은 전기화학적 특성이 우수하고, 특히 $MoO_3$ 는 한 분자당 6 개의 리튬 이온 및 전자를 받고 내줄 수 있기 때문에 큰 용량 (이론용량: 1117 mAh $g^{-1}$) 을 발현 한다는 장점이 있다. 하지만, 전환 반응의 특성상 결합이 깨졌다 생성되는 반응이 완벽히 가역적이지 못하고, 또한 새로 생긴 수 나노 크기의 금속 표면에서 전해질 부 반응이 심하게 일어나기 때문에 초기 쿨롱 효율이 낮다는 단점이 있다. 완전지에서 음극의 초기 쿨롱 효율이 낮으면, 셀 안에 있는 리튬의 양이 비가역적으로 많이 소모된다는 것이기 때문에 이후 사이클에서의 용량이 크게 감소하게 된다. 따라서 낮은 초기 쿨롱 효율은 전환 반응을 하는 금속산화물의 상용화를 막는 큰 문제점이라 할 수 있겠다.

본 연구에서는 이렇듯 전환 반응을 하는 몰리브데넘 산화물의 낮은 초기 쿨롱 효율 및 좋지 않은 전기화학 성능을 개선하기 위해 3 가지 전략을 사용하였다. 첫 번째로는, 성능이 좋다고 잘 알려진 비정질

몰리브데넘 산화물을 수계 환원법으로 합성함에 있어, pH 조절을 통해 그것의 산화수를 조절하여 물성 및 전기화학 성능을 향상시켰다. 두 번째로는, $MoO_3$ 에 약한 볼밀링을 짧은 시간 동안만 가해주어 초기 쿨롱 효율 및 전기화학 성능을 향상시켰다. 이는, 짧은 볼밀을 통해 생긴 갈아진 표면과 수십 나노 크기의 작은 분진들로 인해 생긴 효과라고 생각된다. 마지막으로는, 충전 시 받은 것 보다 더 많은 리튬 이온 및 전자를 방전 시에 발현하도록 설계된 $Li_2MoO_3$ 라는 새로운 음극 물질을 이용하는 것으로, 100 % 가 넘는 초기 쿨롱 효율을 얻을 수 있었다. 이렇듯 사용한 전략들이 잘 발현되었는지 확인하기 위해, 다양한 전기화학적 방법과 분광학적 방법을 적극 사용하였다. 이번 연구에서 제안한 방법들은 몰리브데넘 산화물뿐만 아니라 전환 반응을 하는 다양한 금속 산화물에 적용할 수 있을 것이며, 이는 금속 산화물 음극 물질의 상용화에 한걸음 더 다가갈 수 있는 계기가 될 것이라 생각된다.

---

**키워드:** 리튬 이온 전지, 음극, 몰리브데넘 산화물, 비정질 산화물, 전환 반응, 초기 쿨롱 효율

**학 번:** 2010 – 21012